

Towards increased realism of a computer simulation of human childbirth



Said-Magomed Sadulaev

Supervisor: Dr. Rudy Lapeer

School of Computing Sciences

University of East Anglia

Degree of Doctor of Philosophy

September 2019

Contents

Contents	i
List of Figures	v
List of Tables	xi
1 Introduction	1
1.1 Background and Motivation	1
1.2 Human childbirth labour	4
1.2.1 Stages of Labour	4
1.2.2 Presentation	6
1.2.3 Position	6
1.2.4 Mechanical View	7
1.2.5 Standard Cardinal movements	8
1.3 Newborn Spine	12
1.3.1 Newborn Cervical Vertebrae	12
1.4 Maternal pelvis	13
1.4.1 Pelvic types	13
1.4.2 Bony structure	13
1.4.3 Mobility of the sacrum	13
1.4.4 Mobility of the coccyx	14
1.5 Hypothesis	14
1.6 Thesis Overview	15
1.6.1 Contributions	15
1.6.2 List of publications	16
1.6.3 Other contributions	16
2 Literature review	22
2.1 Introduction to Literature Review	22
2.1.1 Virtual childbirth simulators	22
2.2 Four main schemes of the computational neck model	24

2.2.1	Continuum rod model	25
2.2.2	Two-pivot (three bodies) models	25
2.2.3	Multi-body models	26
2.2.4	Finite element models	27
2.3	Mechanical properties of the fetal/pediatric spine	28
2.3.1	Luck et al. (2008)	28
2.3.2	Ouyang et al. (2005)	29
2.3.3	Luck (2012)	30
2.3.4	Nuckley et al. (2013a)	30
2.4	Existing computational models of newborn infants	37
2.4.1	Q0 ATD finite-element model	37
2.4.2	Nita infant model	38
2.4.3	MD Adams infant model	38
2.5	Range of motion of an infant skull	40
2.6	Conclusion	42
3	Developing a computational fetal neck model	43
3.1	Overview	43
3.2	Methodology	44
3.2.1	Overview	44
3.2.2	Complete mechanical properties of the fetal neck	44
3.2.3	BirthViewH	51
3.2.4	Mechanical models of the fetal neck	64
3.2.5	Validation of the fetal neck range of motion	71
3.3	Computational Neck Models	78
3.3.1	Overview	78
3.3.2	Preliminary experiments in BirthEngine	79
3.3.3	Basic Neck model (NM01)	84
3.3.4	Validation of the basic neck model in BirthView	86
3.3.5	Improved Neck model (NM02)	92
3.3.6	A one-pivot neck model with 6DOF spring constraint (NM03)	94
3.3.7	Two pivot neck model (NM04)	96
3.3.8	Conclusion	97
4	Optimization of childbirth simulation	99
4.1	Mesh Generation	99
4.1.1	Overview	99
4.1.2	Gynecoid pelvis	99
4.1.3	Spine, shoulders and rib cage	100
4.2	Sacrum mobility	101
4.2.1	Introduction	101

4.2.2	Experimental setup	102
4.2.3	Analysis	104
4.3	Expulsion	105
4.3.1	Introduction	105
4.3.2	Analysis	106
4.3.3	Affects of disabling the bending spring after the fetal head is born	107
4.3.4	Expulsion of shoulders	108
4.4	Shoulder dystocia	109
4.4.1	Introduction	109
4.4.2	Experiment	110
4.5	Validation of the BirthView TLED procedure	112
4.5.1	Introduction	112
4.5.2	Sphere on cube experiment	117
4.6	Experimental study of OP position	121
4.6.1	Overview	121
4.6.2	Direct OP using the old neck model (NM01)	122
4.6.3	Direct OP using the new neck model (NM03)	122
4.6.4	Pelvis tilted by 10 degrees	124
4.7	Experimental study of cardinal movements with different dimen- sions of the fetal head	126
4.7.1	Introduction	126
4.7.2	Cephalic index	127
4.7.3	Biparietal diameter (BPD)	128
4.7.4	Experimental setup	129
4.7.5	Analysis	136
4.7.6	Additional experiments	137
4.7.7	Conclusion	139
5	Summary and Conclusions	143
5.1	Conclusion	143
5.2	Summary	144
5.3	Limitations and Future work	145
5.3.1	Limitations	145
5.3.2	Future work	146
	Bibliography	149
	Appendices	160

A	Experimental study of cardinal movements with different dimension of the fetal head	161
B	A clinical study of ROM in healthy newborn babies	179
	B.1 Introduction	179
	B.2 Motivation	180
	B.3 Methods	180
	B.4 Study	183
	B.5 Procedures	184
	B.6 Measuring ROMs	184
	B.7 Analysis	185
	B.8 Application	186
C	Instructions on BirthViewH for midwives	188
	C.1 Aim	188
	C.2 Procedure	188
	C.3 Instructions	189
	C.4 Setting up stiffness and damping value	189
	C.5 Flexion/extension/lateral bending testing	189
	C.6 Side rotations testing	189
D	Glossary	191
E	Childbirth simulators	194
	E.1 BirthEngine	194
	E.2 BirthView	195
	E.2.1 Cross-platform	195
	E.2.2 Scalability	195
	E.2.3 Entity Component System	195
F	Human Spine	198
	F.1 Vertebral Column	199
	F.2 Vertebra	200
	F.3 Joints	200
	F.3.1 Intervertebral Discs	201
	F.3.2 Synovial Joints	201
	F.3.3 Ligaments	201

List of Figures

1.1	UEA virtual childbirth simulator (Lapeer et al., 2019).	2
1.2	An example of an imposed trajectory applied to a fetal head. Image from Jing et al. (2012).	3
1.3	First stage of labour.	5
1.4	Second stage of labour.	5
1.5	Third stage of labour.	6
1.6	Fetal Head Diameters: OF - occipito-frontal, SOB - sub-occipito bregmatic, SOF - sub-occipito frontal, SMB - sub-mento bregmatic, MV - mento-vertical, SMV - sub-mento vertical.	7
1.7	Positions of the head in vertex presentation	8
1.8	Engagement	9
1.9	Descent and flexion	9
1.10	Internal rotation	10
1.11	Descent and flexion	10
1.12	External rotation	10
1.13	Descent and flexion	10
1.14	Diagram showing the positions of the fetal head and shoulders (bisacromial diameter) in the different stages of descent (Borell and Fernström, 1958). The upper diagram is showing the number of cases when the orientation of the fetal shoulders was either sagittal, oblique or transverse, at certain stations (positions), with respect to the pelvis. Similarly, the lower diagram is showing the orientations of the fetal head with respect to the pelvis.	18
1.15	Infant Spine. Image from Crelin (1969).	19
1.16	Atlas. Image from Crelin (1969).	20
1.17	Axis. Image from Crelin (1969).	20
1.18	4th Cervical Vertebra. Image from Crelin (1969).	20
1.19	The four standard or pelvic types (Caldwell and Moloy, 1938).	21
1.20	Human pelvis (Drake et al., 2015).	21

2.1	Tensile stiffness (N/mm) of the upper cervical spine (O-C2) segment from Luck et al. (2008) compared to three previous juvenile animal surrogate studies	29
2.2	Flexion and Extension Range of Motion (ROM) for Perinatal, Neonatal and Pediatric PMHS from the paper by Luck (2012)	41
3.1	Springs in series	45
3.2	Flexion and extension stiffness in O-C2 (Luck, 2012)	47
3.3	Flexion and extension stiffness in C4-C5 (Luck, 2012)	47
3.4	Flexion and extension stiffness in C6-C7 (Luck, 2012)	47
3.5	Logarithmic regression of C1-C2 for adults	52
3.6	Logarithmic regression of C4-C5 for adults	53
3.7	Logarithmic regression of C6-C7 for adults	53
3.8	BirthViewH	54
3.9	BirthViewH class diagram.	55
3.10	Basic Neck in BirthView.	59
3.11	Two haptic devices used in BirthViewH.	61
3.12	Bushing element comprising six degrees-of-freedom springs (Autodesk Maya, 2019)	64
3.13	The detailed representation of a single tensile/compressive spring attachment in the bushing element.	65
3.14	Head in normal position (front view)	67
3.15	Head is flexed laterally (front view)	67
3.16	Head in normal position (front view)	68
3.17	Head is rotated (top view).	68
3.18	Ball and Socket Joint	69
3.19	Displacement vector from point $A1$ to point $P1$	69
3.20	Object's distance from the attachment point	70
3.21	Displacement vector from rotated $A1$ to $P1$	71
3.22	Mass-Spring-Damper system	71
3.23	Goniometer	72
3.24	Starting position for measuring cervical flexion	74
3.25	Measuring flexion with a goniometer	74
3.26	Starting position for measuring cervical extension	75
3.27	Measuring extension with a goniometer	75
3.28	Starting position for measuring side rotation	76
3.29	Measuring side rotation with a goniometer	76
3.30	Lateral bending.	77
3.31	Measuring angles in Kinovea	78
3.32	Perspective measurements in Kinovea	79
3.33	Flexion	80

3.34	Lateral Bending	80
3.35	Childbirth simulation with the fetal body trunk	81
3.36	Basic Neck in BirthView.	87
3.37	Measuring extension from NIPE video in Kinovea.	88
3.38	Measuring extension in BirthView with a tensile spring	88
3.39	A newborn's head trajectory in flexion/extension.	89
3.40	Extension of the fetal head during labour in BirthView.	90
3.41	Extreme lateral bending of the fetal head with a longer neck.	91
3.42	Simulating childbirth with a head width of 9.03cm.	92
3.43	Simulating childbirth with a head width of 9.03cm.	93
4.1	Gynecoid pelvis	100
4.2	Gynecoid pelvis with separated sacrum and coccyx	100
4.3	A CT scan of a 6 months old baby girl	101
4.4	Pelvic moulding: the fetal head is in contact with the coccyx.	104
4.5	Pelvic moulding: the fetal head is in contact with the sacrum.	105
4.6	Graph of simulating labour with a static sacrum.	106
4.7	Graph of simulating labour with a mobile sacrum.	107
4.8	Flexion observed in MRI video (Bamberg et al., 2012).	108
4.9	Extension observed in MRI video (Bamberg et al., 2012).	109
4.10	The fetal trunk after the head descended into the pelvic cavity illustrating the expulsion force directions.	110
4.11	Simulation with a trunk cut in half.	111
4.12	Delivery of a fetus, front view.	112
4.13	Delivery of a fetus, side view.	113
4.14	Shoulder arrest below and left to the pubic symphysis.	114
4.15	Shoulder arrest behind the pubic symphysis.	115
4.16	Sphere on cube experiment in BirthView.	117
4.17	Comparison of BirthView TLED/pDN against Abaqus Explicit for a sphere of 10 kg released on a cube.	119
4.18	Comparison of BirthView TLED/pDN against Abaqus Explicit for a sphere of 15 kg released on a cube.	120
4.19	New mesh models for the fetus and maternal pelvis.	121
4.20	Graph of simulating a direct OP with NM04 neck model.	123
4.21	Expulsion force in direct OP with NM01.	124
4.22	The trunk in contact with sacrum and lower maternal spine.	125
4.23	OP delivery with high expulsion force.	126
4.24	Graph of a non-controlled simulation of a direct OP with NM03 neck model.	127
4.25	Expulsion force in direct OP with NM03 (non-controlled).	128

4.26	Graph of a controlled simulation of a direct OP with NM03 neck model.	129
4.27	Expulsion force in direct OP with NM03 (controlled).	130
4.28	Graph of a non-controlled simulation of a direct OP with NM03 neck model.	130
4.29	Expulsion force in direct OP with NM03 (non-controlled).	131
4.30	OP with tilted pelvis.	132
4.31	Measuring head length with calipers.	132
4.32	Measuring head width with calipers.	132
4.33	Measuring the fetal head's length in Blender with a ruler.	133
4.34	Head width, both sexes, at birth.	133
4.35	Simulating childbirth (LOT) with a head width of 9.07cm.	135
4.36	Simulating childbirth with a head width of 9.07cm.	136
4.37	Relationship between expulsion force and BPDs	137
4.38	Simulating childbirth (ROT) with a head width of 9.15cm.	138
4.39	Simulating childbirth with a head width of 9.07cm.	139
4.40	Comparison of expulsion force required for the neck length of 2.4cm and 3.6cm	140
4.41	Simulating childbirth (LOT) with a head width of 9.07cm and neck length of 2.4cm.	141
4.42	Simulating childbirth with a head width of 9.07cm and neck length of 2.4cm.	142
A.1	Simulating childbirth (LOT) with a head width of 9.15cm.	161
A.2	Simulating childbirth with a head width of 9.15cm.	162
A.3	Simulating childbirth (LOT) with a head width of 9.2cm.	162
A.4	Simulating childbirth with a head width of 9.2cm.	163
A.5	Simulating childbirth (LOT) with a head width of 9.25cm.	163
A.6	Simulating childbirth with a head width of 9.25cm.	164
A.7	Simulating childbirth (LOT) with a head width of 9.3cm.	164
A.8	Simulating childbirth with a head width of 9.3cm.	165
A.9	Simulating childbirth (LOT) with a head width of 9.35cm.	165
A.10	Simulating childbirth with a head width of 9.35cm.	166
A.11	Simulating childbirth (LOT) with a head width of 9.4cm.	166
A.12	Simulating childbirth with a head width of 9.4cm.	167
A.13	Simulating childbirth (LOT) with a head width of 9.45cm.	167
A.14	Simulating childbirth with a head width of 9.45cm.	168
A.15	Simulating childbirth (LOT) with a head width of 9.5cm.	168
A.16	Simulating childbirth with a head width of 9.5cm.	169
A.17	Simulating childbirth (LOT) with a head width of 9.56cm.	169
A.18	Simulating childbirth with a head width of 9.56cm.	170

A.19	Simulating childbirth (LOT) with a head width of 9.15cm and neck length of 2.4cm.	170
A.20	Expulsion force when simulating childbirth with a head width of 9.15cm and neck length of 2.4cm.	171
A.21	Simulating childbirth (LOT) with a head width of 9.2cm and neck length of 2.4cm.	171
A.22	Expulsion force when simulating childbirth with a head width of 9.2cm and neck length of 2.4cm.	172
A.23	Simulating childbirth (LOT) with a head width of 9.25cm and neck length of 2.4cm.	172
A.24	Expulsion force when simulating childbirth with a head width of 9.25cm and neck length of 2.4cm.	173
A.25	Simulating childbirth (LOT) with a head width of 9.3cm and neck length of 2.4cm.	173
A.26	Expulsion force when simulating childbirth with a head width of 9.3cm and neck length of 2.4cm.	174
A.27	Simulating childbirth (LOT) with a head width of 9.35cm and neck length of 2.4cm.	174
A.28	Expulsion force when simulating childbirth with a head width of 9.35cm and neck length of 2.4cm.	175
A.29	Simulating childbirth (LOT) with a head width of 9.4cm and neck length of 2.4cm.	175
A.30	Expulsion force when simulating childbirth with a head width of 9.4cm and neck length of 2.4cm.	176
A.31	Simulating childbirth (LOT) with a head width of 9.45cm and neck length of 2.4cm.	176
A.32	Expulsion force when simulating childbirth with a head width of 9.45cm and neck length of 2.4cm.	177
A.33	Simulating childbirth (LOT) with a head width of 9.5cm and neck length of 2.4cm.	177
A.34	Expulsion force when simulating childbirth with a head width of 9.5cm and neck length of 2.4cm.	178
B.1	Three planes of ROM	181
B.2	Measuring device of ROMs of the neck of a newborn.	181
B.3	Accelerometer BWT901CL.	182
B.4	Range of motion.	182
B.5	Safety helmet for infants.	187
B.6	Scale	187
B.7	Dynamometer	187

E.1	BirthView solution's list of plugin projects.	196
E.2	Entity component system use in BirthEngine.	196
E.3	Cervix Scene in BirthView	197
E.4	Cervix Scene in BirthView	197
F.1	Spine regions	198
F.2	Cervical Vertebra	199
F.3	Thoracic Vertebra	199
F.4	Lumbar Vertebra	200
F.5	Typical Vertebra	200
F.6	Intervertebral Disc	201
F.7	Zygapophysial Joints	202
F.8	Zygapophysial Joints	202
F.9	Anterior and Posterior Longitudinal Ligaments	202
F.10	Ligamenta Flava	203
F.11	Ligamentum Nuchae and Supraspinous Ligament	203
F.12	Interspinous Ligaments	204

List of Tables

2.1	Biomechanics of pediatric cervical spine’s section O-C2 (Luck et al., 2008; Luck, 2012; Luck et al., 2013). Flexion and extension are given in Nm/degrees. Compression and tension are given in N/mm.	31
2.2	Biomechanics of pediatric cervical spine’s section C4-C5 (Luck et al., 2008; Luck, 2012; Luck et al., 2013). Flexion and extension are given in Nm/degrees. Compression and tension are given in N/mm.	32
2.3	Biomechanics of pediatric cervical spine’s section C6-C7 (Luck et al., 2008; Luck, 2012; Luck et al., 2013). Flexion and extension are given in Nm/degrees. Compression and tension are given in N/mm.	33
2.4	Biomechanics of pediatric cervical spine’s section C1-C2 (Nuckley et al., 2013b).	34
2.5	Biomechanics of pediatric cervical spine’s section C3-C5 (Nuckley et al., 2013b).	35
2.6	Biomechanics of pediatric cervical spine’s section C6-C7 (Nuckley et al., 2013b).	36
2.7	Mean Measurements of Rotation and Lateral Flexion at the Ages of 2, 4, 6, and 10 Months	40
2.8	Flexion and Extension Range of Motion (ROM) for Perinatal, Neonatal and Pediatric PMHS from the paper by Luck (2012). In order to get the age in days multiply by factor 30.4167.	41
3.1	Complete predicted stiffness values for the segment C1-C2 in newborns. Compression and tension are given in N/m. Flexion, extension, lateral bending and axial rotation in Nm/deg.	49
3.2	Complete predicted stiffness values for the segment C4-C5 in newborns. Compression and tension are given in N/m. Flexion, extension, lateral bending and axial rotation in Nm/deg.	49

3.3	Complete predicted stiffness values for the segment C6-C7 in newborns. Compression and tension are given in N/m. Flexion, extension, lateral bending and axial rotation in Nm/deg.	50
3.4	The Geomagic Touch specification	54
3.5	Mechanical properties of NM01	72
3.6	Experimental results	82
3.7	Mechanical properties of NM01 and NM02 (see 3.3.5)	84
3.8	Experimental results with NM01 and NM02 (see 3.3.5)	86
3.9	ROM of the head in extension with and without the tensile spring (BirthView)	88
3.10	Newborn PMHS Anthropometric Data (Luck et al., 2008)	94
3.11	Mean stiffness values for each cervical spine's segment and the combined equivalent stiffness of all segments. Compression and tension are given in N/m. Flexion, extension, lateral bending and axial rotation are given in Nm/deg.	95
3.12	Combined stiffness for upper cervical spine	97
3.13	Combined stiffness for lower cervical spine	97
4.1	The experimental setup of BirthView for the experimental study on pelvic moulding	103
4.2	Comparison of BirthView implementation of TLED with projection based contact against Abaqus Explicit Contact.	116
4.3	Increasing the number of tetrahedral elements of a Neo-hookean hyperelastic cube subjected to distributed force shows that project based contact method implemented in BirthView is not sensitive to mesh complexity.	116
4.4	Comparison of BirthView implementation of project based contact method against Abaqus explicit.	118
4.5	The experimental setup of BirthView for the experimental study of cardinal movements with different dimension of the fetal head.	134
B.1	Measurements required for finding range of motion of a newborn baby's head (template).	183
B.2	Measurements that are normally recorded after birth. Bold items may have to be measured during the study (template).	183

Acknowledgements

I would like to express my sincere gratitude to Dr Rudy Lapeer, who has been supervising my PhD, for helping me throughout my entire degree, for the opportunity to be involved in this fascinating research, for valuable suggestions and his patience in addressing all the issues I faced in four years.

Also I would like to thank my best friend and colleague Dr Zelimkhan Gerikhanov, for his constant support and help, for introducing me to research in general and motivating me to apply for this degree.

I would like to thank Dr Abdurrahman Saeed for keeping me a company, giving advices, constantly motivating me and sharing his experience in doing a PhD.

I would like to thank my friend Binoop Pulikkottil John for whenever I needed help with solving issues with my PC, he has always been there for me. Thank you for helping me to build the device for measuring range of motion of a newborn's neck.

Last but not least, I would like to thank my family, my wife and, most importantly, my parents who have been patiently supporting me during my entire studies for 11 years.

Abstract

A virtual childbirth simulator is normally associated with a computer analogue of mechanical mannequins used for training purposes in obstetrics. Such a simulator would allow acquiring a deeper understanding of the labour and the necessary expertise for students in obstetrics. A patient-specific childbirth simulator, in turn, would be capable of predicting difficult birth scenarios in advance based on the ultrasound or magnetic resonance imaging scans of the maternal pelvis and fetus. This would give the midwives time to prepare for the predicted worst-case scenarios and potentially reduce morbidity and mortality of both babies and their mothers. The existing virtual childbirth simulator successfully simulates physiologic labour. This thesis is concerned with taking the software one step closer towards being a patient-specific virtual childbirth simulator and to simulate difficult birth scenarios.

The core content of this thesis is concerned with the development of computational fetal neck models. A number of neck models were developed and tested in the simulator. The methods used to simulate the fetal neck are the following: ball and socket joint for intervertebral discs, spring-and-damper systems for ligaments and six-degrees-of-freedom bushing element to simulate a coupled behaviour of the discs, ligaments and neck muscles. The latest one-pivot neck model is using a six-degrees-of-freedom bushing element to simulate the behaviour of the fetal head. The developed neck model, together with the approximated complete mechanical properties of the fetal spine, facilitated running the experiments with a higher variety of biomechanical parameters such as the neck's length, strength and a full range of fetal biparietal diameters. The experiments are reported in this thesis.

An additional simulation software, using haptic devices, was developed specifically for validation of the developed computational neck models. The software allows manipulating of a virtual fetal head on the screen, using two haptic devices. It is used to validate the resistance of the fetal head, during flexion, extension and rotation. It was clinically tested by midwives and obstetricians at the hospital. The results showed that the software is capable of replicating biomechanical properties of a newborn's head motion, with the help from the clinicians.

Experiments were conducted to validate the accuracy of the Total Lagrangian Explicit Dynamics (TLED) contact method, used in the software, against Abaqus software. The validation setup consisted of a finite element cube and a rigid body plate, pushing vertically down on the cube with a gravitational force of 9.81N. Similarly, the experiment was repeated for a rigid body sphere pushing on the top of the cube. The results showed that TLED is less sensitive to the number of tetrahedral elements as compared to Abaqus Explicit contact method.

Another set of experiments were conducted for resolving a direct occipito-posterior position (OP) of the fetal head, which is considered to be a difficult birth scenario. In OP midwives advise their patients to tilt their pelvises anteriorly to help with labour. This method was experimentally tested in the childbirth simulator and the results showed that tilting a pelvis anteriorly could potentially ease the dilation during the first stage of labour. However, no significant difference was observed as compared to the non-tilted pelvis during the second stage of labour.

Experiments were run to observe shoulder dystocia in the childbirth simulator. Initially it was not possible to observe shoulder dystocia due to the rigid fetal trunk coming into contact with the maternal sacrum. A number of adjustments were made in order to allow the rigid fetal trunk to follow the fetal head, such as increasing the fetal shoulders to the average width, cutting the trunk in half and disabling the spring keeping the trunk vertical. Shoulder dystocia was observed in the simulator even in the absence of the complete birth canal, articulated fetal shoulders and flexible fetal chest.

Finally, a new maternal pelvis was introduced in the software with a mobile sacrum. The sacrum was attached to the rest of the pelvis using the six degrees-of-freedom bushing element. The effects of the sacrum mobility on a childbirth were studied. The results show that a mobile sacrum contributes toward the full internal rotation of the fetal head during a childbirth, whereas the absence of the mobility leads to the arrest of the head in the anteroposterior diameter of the pelvis.

Chapter 1

Introduction

1.1 Background and Motivation

Virtual reality (VR) based forward-engineered¹ childbirth simulators can be used as a training ground for future obstetricians and, more importantly, to predict difficult labour in advance. One of the advantages of such a virtual simulator over a mechanical mannequin² is that a teacher is not required to be present in order for a student to observe and learn different birth scenarios. More than that, the simulator would allow to experiment with a virtual fetus to gain sufficient experience and, at the same time, to avoid harming real patients and their babies during labour due to lack of necessary expertise.

The existing simulation software BirthView (see Figure 1.1) includes the following models: rigid body fetal skull, rigid body maternal pelvis, basic neck (implemented with Hooke's Law), finite element (FE) deformable cervix, pelvic floor muscles and sacrospinous ligaments. It has been developed by Lapeer's research group at the University of East Anglia (Lapeer et al., 2014).

Currently the simulator is capable of successfully simulating the following cardinal movements in the way they are described in the mainstream obstetrics literature: engagement, descent, flexion, internal rotation, extension, restitution

¹Reverse engineered simulations use superimposed trajectories of the motion of a simulation object and are animations rather than simulations. With regard to the reverse engineered childbirth simulation the trajectory of descent of the fetal head is predefined or replicated from the observed real life scenarios (see Figure 1.2).

²Such as ESP Advanced Childbirth Simulator (<https://esp-models.co.uk>)

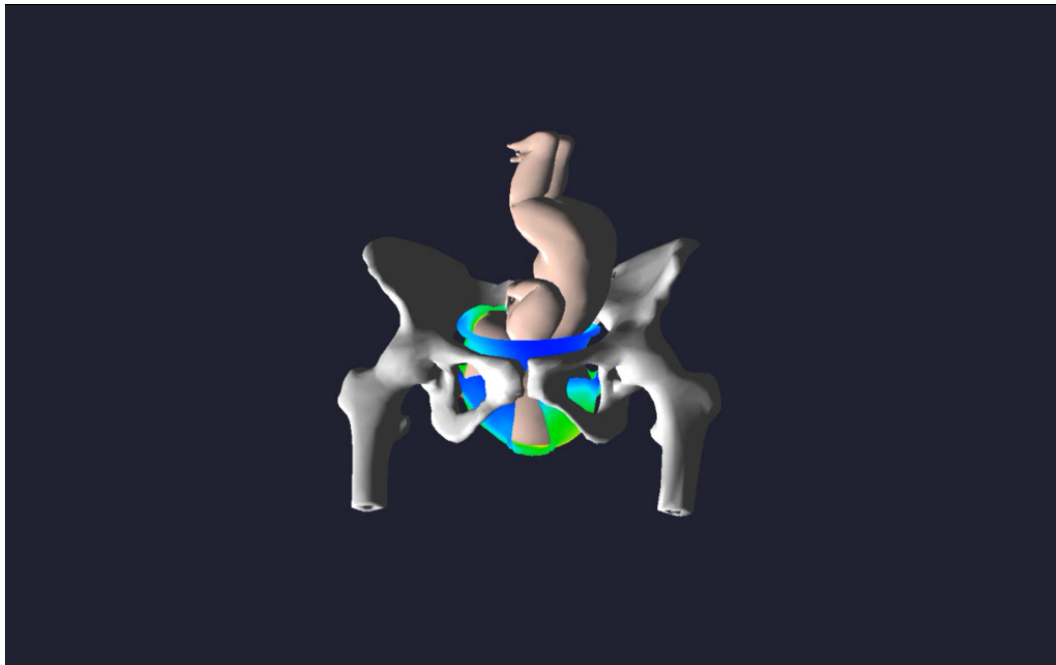


Figure 1.1: UEA virtual childbirth simulator (Lapeer et al., 2019).

and external rotation. However, the obstetrics literature (Chamberlain, 1995) is not always in line with the underlying research in that area (Dietze, 2001) as discussed in Section 1.2.5. Thus, visual observance of the cardinal movements as they are described in the literature is not sufficient to claim that the simulation occurs in a realistic way. In addition, the simulation has only been validated with a single gynecoid pelvis, although admittedly it has also been validated with a few varying parameters of ligaments' tone and head dimensions. The ultimate purpose of the software is to simulate abnormal scenarios for predicting difficult labours and to make the simulator patient-specific. Therefore, more validation and experimental studies are required for both normal and abnormal scenarios.

In this thesis the simulation software will be improved with a better neck model, a mouldable pelvis and validated for both normal and abnormal scenarios, namely, persistent occipito-posterior position. By doing so we addressed some of limitations and future plans mentioned by Gerikhanov (2017) in his thesis. Contributions of this thesis are discussed in more detail in Section 1.6.1.

To this point the validation of the simulation has been primarily done visu-

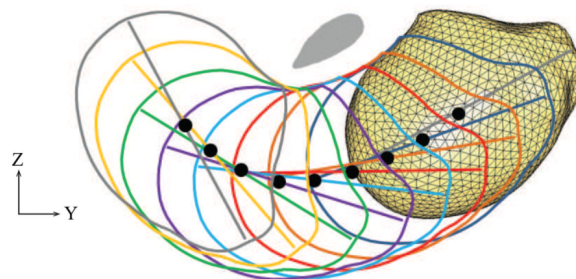


Figure 1.2: An example of an imposed trajectory applied to a fetal head. Image from Jing et al. (2012).

ally by referencing the description of the cardinal movements in the mainstream obstetrics books, which in turn can differ in the way they describe the occurrence of the cardinal movements. Furthermore some of these books do not provide references to the conducted research and experiments, which contributed to the understanding of the labour process and cardinal movements in particular. Consequently, it was deemed necessary to find the papers describing these experiments in pursuit to establish validation criteria.

Borell and Fernström (1957a,b, 1958, 1959) carried out numerous radiographic studies of human labour using a specially constructed delivery table, which allowed simultaneous x-rays to be taken laterally and antero-posteriorly. As indicated by Dietze (2001) there are certain limitations of the studies such as small sample size up to 40 women, unusual delivery position, complete restriction of movement, lack of privacy etc. Nevertheless, according to Dietze (2001) the radiographic studies by Borell and Fernström (1957a,b, 1958, 1959) are widely referenced and most of them have not been replicated by other researchers and it may not be possible to do so due to ethical reasons. Therefore these radiographic plates would be very useful for validation of the childbirth simulation.

Both Ulf Borell and Ingmar Fernström worked at the Department of Diagnostic Roentgenology and the Department of Women's Diseases at Karolinska Sjukhuset (Hospital), Stockholm, Sweden. As indicated in the paper by Dietze (2001), the radiographic plates taken by Borell and Fernström were re-examined by Hans Ohlsen (Ohlsén, 1973), who also worked at the Department of Diagnostic Roentgenology at the same hospital. We contacted Karolinska Hospital and,

unfortunately, it seems like the plates no longer exist. Nevertheless the reported results are still used for validation.

Another study by Bamberg et al. (2012) describes the relationship between the fetus and the pelvis as the fetus travels through the birth canal, using an open magnetic resonance imaging (MRI) scanner. To the best of our knowledge these are the only images available for validation purposes. Unfortunately, some critical parts of the fetus, such as the cervical spine, are not visible on the presented images in the sagittal plane. Moreover, the study has been conducted for one labour only, therefore, validation results cannot be generalised. Based on the results published by Borell and Fernström (1958) (see Figure 1.14) it is fair to assume that labour can progress in multiple ways and one cannot completely rely on a single study.

It is worth mentioning that the simulation presented in Lapeer et al. (2019) is in line with findings of Borell and Fernström (1957a).

The following subsections provide information on the process of human childbirth labour, anatomy of the newborn spine and the maternal pelvis.

1.2 Human childbirth labour

It is important to briefly cover the fundamentals of human childbirth labour such as what labour is, stages of labour, presentations, position and cardinal movements in order to understand the context of this project and the validation criteria.

1.2.1 Stages of Labour

Human childbirth labour is divided into three stages (Symonds, 1992; Chamberlain, 1995):

- During the **first stage** of labour the uterine contractions gradually widen the cervix until it is fully dilated (see Figure 1.3). In case of a cephalic presentation, the dilation is followed by the fetal head entering the birth canal. It is worth mentioning that during the first stage of labour the fetal head may change its shape due to the pressure in the birth canal.

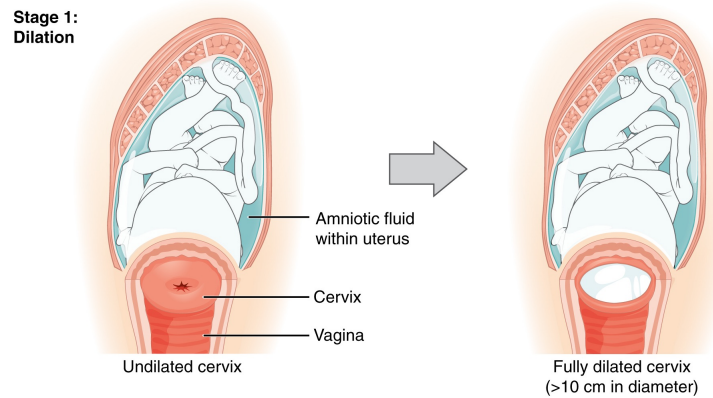


Figure 1.3: First stage of labour.

This phenomenon is known as the fetal head moulding (Lapeer and Prager, 2001).

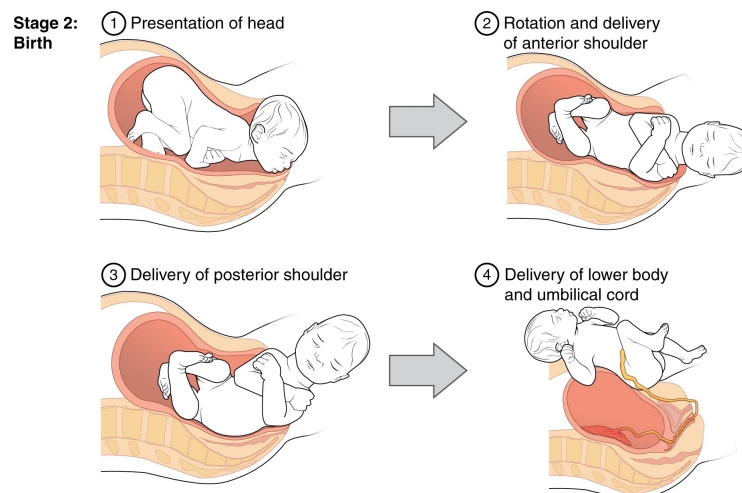


Figure 1.4: Second stage of labour.

- The **second stage**, or stage of expulsion starts when the previous stage terminates and ends with the birth of the fetus (see Figure 1.4).
- After the fetus is born, the **third stage**, or placental stage commences and ends with the delivery of the placenta (see Figure 1.5).

This project is concerned with the second stage of labour only.

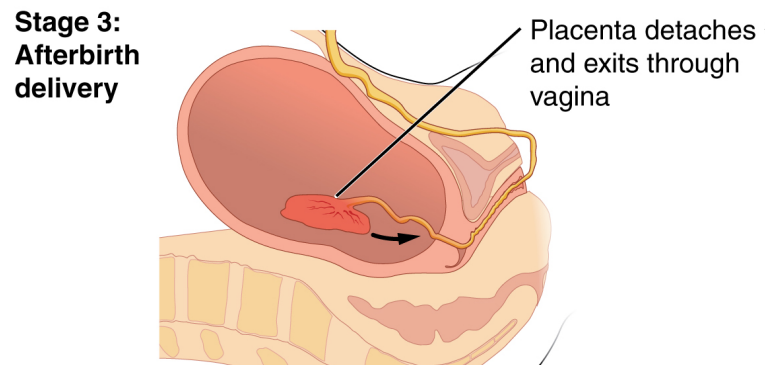


Figure 1.5: Third stage of labour.

1.2.2 Presentation

Presentation of a fetus refers to which anatomical part of the fetus is leading during human childbirth labour. When the head is the leading part, the presentation is termed *cephalic*. If the head is well flexed, the presenting part is the *vertex* (sub-occipito-bregmatic diameter¹/see Figure 1.6). If the head is fully extended, there is a *face* presentation (sub-mento-bregmatic diameter), and if it is partly extended, there is a *brow* presentation (vertico-mental diameter). The brow is defined as the area between the base of the nose and the anterior fontanelle (Chamberlain, 1995; Symonds, 1992).

1.2.3 Position

Position describes the relationship of a denominator of the presenting part to the right or left side of the maternal pelvis (Chamberlain, 1995). In case of a *vertex* presentation, position describes the relationship of the occiput to the maternal pelvis. Symonds (1992)/see Figure 1.7 describes the following 6 positions for vertex presentation:

- left occipito-anterior (LOA)
- left occipito-transverse (LOT)

¹The diameters of the skull are used to indicate the presenting part

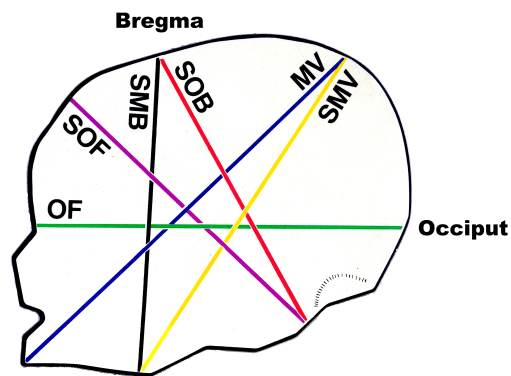


Figure 1.6: Fetal Head Diameters: OF - occipito-frontal, SOB - sub-occipito bregmatic, SOF - sub-occipito frontal, SMB - sub-mento bregmatic, MV - mento-vertical, SMV - sub-mento vertical.

- left occipito-posterior (LOP)
- right occipito-anterior (ROA)
- right occipito-transverse (ROT)
- right occipito-posterior (ROP)

1.2.4 Mechanical View

The developed simulation software approaches labour as a mechanical problem or to be more precise as a biomechanical one. This means that the laws of physics are applied to labour to simulate the process as close to reality as possible. This includes calculation of forces and respective displacements of rigid bodies and deformation of soft tissues. In addition it is worth mentioning that the fetus is considered to be passive, i.e. the fetus is compliant with the surrounding bony structures and soft tissues as it moves down the birth canal. However, the author must admit that the fetus might be performing certain movements reflexively as a reaction to external impact (Dietze, 2001).

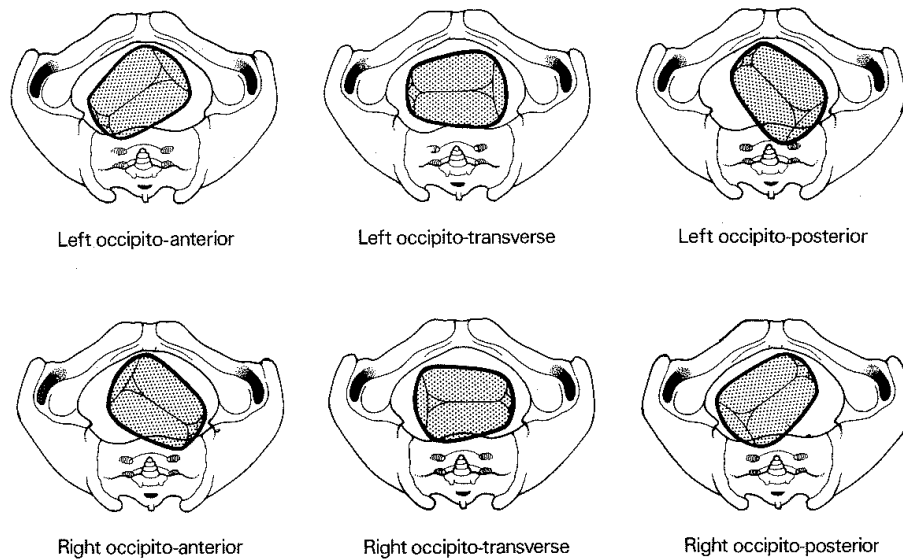


Figure 1.7: Positions of the head in vertex presentation

1.2.5 Standard Cardinal movements

Cardinal movements or the mechanisms of labour are the passive movements of the fetal head, which include change in position and orientation, during its passage through the birth canal. A number of obstetrics books describe five (Chamberlain, 1995), seven (Gabbe et al., 2012), eight (Symonds, 1992) discrete cardinal movements:

1. Engagement (Gabbe et al., 2012);
2. Descent (Gabbe et al., 2012; Symonds, 1992);
3. Flexion;
4. Internal rotation;
5. Extension;
6. Restitution (Symonds, 1992; Chamberlain, 1995);
7. External rotation;
8. Expulsion/Deliver of the shoulders (Symonds, 1992; Gabbe et al., 2012)

The mechanisms of labour are extremely important for the validation of the childbirth simulator.

Before we describe the mechanisms of labour, it is important to keep in mind that there is no unique way of undergoing cardinal movements as we will see later. Sometimes one can observe all of them, and sometimes the fetus tends to "skip" certain movements (Dietze, 2001).

Engagement refers to the entrance of the widest diameter of the fetal head into the smallest diameter of the maternal pelvis (see Figure 1.8). Engagement does not always happen before labour, i.e. sometimes it occurs during labour. For that reason it seems, Symonds (1992) combined engagement with descent.



Figure 1.8: Engagement



Figure 1.9: Descent and flexion

Descent is a measure of progress in labour and it must always happen for the fetus to be born. It refers to the downwards motion of the fetal head through the pelvis.

Flexion of the fetal chin onto the chest occurs when the head descends and meets the soft tissues of the pelvic floor. It produces a smaller diameter of presentation, changing from the occipito-frontal diameter to the sub-occipito bregmatic diameter (see Figure 1.6).

Internal rotation refers to rotation of the head when it hits the pelvic floor and, in most cases, the occiput rotates from its original position to the pubic symphysis (Symonds, 1992). Occasionally it moves in the opposite direction towards the sacrum. It is worth mentioning that Borell and Fernström (1958) observed that following this rotation of the head the fetal shoulders also rotated in the same direction.

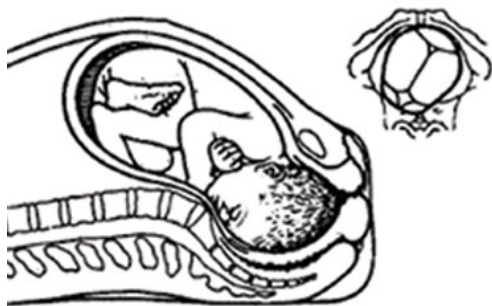


Figure 1.10: Internal rotation



Figure 1.11: Extension

Extension. There is a difference in opinion about when and where the extension takes place. According to Symonds (1992) “the sharply flexed head descends to the vulva and the base of the occiput comes into contact with the inferior rami of the pubi”. He adds that the head then starts extending until it is delivered. In contrast to Symond’s observation, Borell and Fernström (1958) revealed in their radiographic study that the fetal thoracic spine (back) extends during the extension stage, following internal rotation, and the fetal head remains flexed until after delivery.

Restitution refers to the return of the fetal head to the correct anatomic position in relation to the fetal shoulders. Gabbe et al. (2012) state that this can happen to either side depending on the orientation of the fetus (see Section 1.2.3). They also refer to the restitution as the external rotation.



Figure 1.12: External rotation



Figure 1.13: Expulsion

External rotation refers to the rotation of the fetal shoulders into the anteroposterior diameter. This is followed by the further rotation of the fetal head.

Symonds (1992) claims that the rotation occurs when the shoulders reach the pelvic floor same as the internal rotation of the fetal head.

Gabbe et al. (2012) describe the rotation of the shoulders as a part of expulsion/delivery of the shoulders and Borell and Fernström (1958) refers to the rotation as the second rotation of the shoulders. According to Gabbe et al. (2012) after the delivery of the head and restitution, which they refer to as external rotation, the anterior shoulder reaches the level of the symphysis pubis. Then the anterior shoulder is delivered similar to the internal rotation of the head, with its rotation under the symphysis pubis (Figure 1.20).

Finally Chamberlain (1995) describes the process as follows:

“As the shoulders descend the right and anterior shoulder is lower and meets the resistance of the pelvic floor before the left shoulder. The right shoulder rotates to the space in front, as did the the occiput...”.

These descriptions complement each other.

Nevertheless, there is another opinion, given by Borell and Fernström (1958) and supported by their radiographic studies on 40 women. In this study, in most of the cases, the internal rotation of the fetal head occurred between the ischial spines and the ischial tuberosities, whilst the second rotation of the fetal shoulders occur well below that level. In addition according to Sellheim et al. (1906) the fetal chest is more flexible in the lateral rather than in the dorsal direction. Therefore, at the time of the passage of the middle part of the chest through the curved part of the birth canal the second rotation of the shoulders occurs. This claim has been supported by the radiographic studies by Borell and Fernström (1958).

Hence, they suggest that the second rotation of the shoulders are not caused by the same mechanism as the internal rotation of the head, but rather by the fetal chest, which rotates in order to pass through the curved part of the birth canal.

Expulsion completes the second stage of labour by delivering the fetal shoulders, trunk and legs. Gabbe et al. (2012) described the second rotation of the fetal shoulders as part of expulsion.

1.3 Newborn Spine

For a detailed anatomy of the human spine see Appendix F.

The average length of the newborn vertebral column is 19 or 20 cm (approximately 40 percent of the total body length), excluding the sacral and coccygeal vertebrae. The thoracic part constitutes a half of the entire vertebral column in both newborn and adult and the lumbar part increases from a fourth in the newborn to nearly a third in the adult (Crelin, 1973).

The vertebral column does not have any curves at birth and is extremely flexible. According to Crelin (1973) it can be easily bent into a perfect half circle.

1.3.1 Newborn Cervical Vertebrae

1.3.1.1 Size

The cervical vertebrae of the newborn infant constitutes about a fourth of the entire vertebral column, whereas in the adult the cervical part is reduced to a fifth or a sixth of the entire column/see Figure 1.15.

1.3.1.2 Ossification Centres

All cervical vertebrae, except the first (atlas) and second (axis) one, have similar structure and are composed of three ossification centres joined by hyaline cartilage. The atlas consists of “only two bony centres” and the axis is comprised of four ossification centres (see Figures 1.17, 1.16 and 1.18).

1.3.1.3 Intervertebral Discs

In contrast to the intervertebral disc of an adult, the nucleus pulposus of a newborn constitutes the greater part of the intervertebral disc.

1.4 Maternal pelvis

This section provides background information on different pelvic types, anatomy of pelvis and range of motion of sacrum and coccyx.

1.4.1 Pelvic types

Normally female pelvises are classified into one of the following four pelvic types: gynecoid, android, platypelloid and anthropoid.

Caldwell and Moloy (1938) describe them as follow:

- The anthropoid type resembles the long, narrow, oval pelvis of the anthropoid ape.
- The gynecoid type shows all the well-known architectural characteristics of the normal female pelvis.
- The platypelloid type. This pelvis has a wide or transverse oval appearance.
- The android type bears a morphological resemblance to the human male pelvis. The inlet is wedge-shaped or blunt heart-shaped.

However, according to Caldwell and Moloy (1938) many pelvises are a combination of the abovementioned pelvic types, when anterior and posterior segments of a pelvis do not belong to the same type as shown in Figure 1.19.

1.4.2 Bony structure

The pelvis consists of four bones: the right and left hip bones, the sacrum or sacroiliac (SI) body, and the coccyx (see Figure 1.20).

1.4.3 Mobility of the sacrum

The sacrum is connected to the rest of the pelvis through sacroiliac joints or SI joints. The sacroiliac body has six-degrees-of-freedom and its origin lies midway between the left and right posterior superior iliac spines (Goode et al., 2008).

Smidt et al. (1995) systematically reviewed literature on mobility of the sacroiliac joint and reported range of motion along three axes of motion. In this review, the X-axis (transverse axis) accounts for sacral rotation in the sagittal plane, Y-axis (longitudinal axis) for sacral rotation in the horizontal or transverse plane and Z-axis (sagittal axis) accounts for sacral rotation in the coronal plane. Rotation along the X-axis ranged from -1.1 to 2.2 degrees, along the Y-axis -0.8 to 4.0 degrees and along the Z-axis -0.5 to 8.0 degrees. Translations ranged from -0.3 to 8.0 mm along the X-axis, -0.2 to 7.0 mm along the Y-axis and -0.3 to 6.0 mm along the Z-axis.

1.4.4 Mobility of the coccyx

The physiological movements of the coccyx are restricted to flexion and extension (Maigne, 2002). Flexion refers to movement in a forward direction and extension refers to movement in a backward direction. The mobility of the normal coccyx of 47 volunteers has been reported to range from 0 to 22 degrees both for flexion and extension (Maigne et al., 1994). Thirteen coccyges had an extension between 5 and 15 degrees and eight a flexion between 5 and 22 degrees. Twenty-four coccyges had a very limited mobility between 0 and 5 degrees.

1.5 Hypothesis

The null hypothesis (H0) of this research is defined as follows:

H0: Variations of the mechanical properties of the fetal neck model and its implementation should not have a significant effect on the computer childbirth simulation due to weak neck muscles and little resistance of the fetal neck in general.

H1: Variations of the mechanical properties of a computer model of a fetal neck and the implementation of the model itself can significantly affect the outcome of the virtual childbirth simulation.

1.6 Thesis Overview

1.6.1 Contributions

1.6.1.1 Development of a virtual reality program to assess strength and flexibility of a newborn baby's neck

A virtual reality program was developed to assess strength and flexibility of a computer based model of a term fetus or newborn baby's neck. The software has a haptic/force feedback user interface which allows clinical experts to adjust the mechanical properties, including range of motion and mechanical stiffness of a newborn neck model, at runtime. The developed software was assessed by ten clinical experts in obstetrics. The empirically obtained stiffness and range of motion values corresponded well with values reported in the literature.

1.6.1.2 Experimental study of resolving persistent occipito-posterior position of a fetal head

The effects of tilting a maternal pelvis on resolving persistent occipito-posterior position (OP) of a fetal head have been studied and reported.

1.6.1.3 Experimental study of cardinal movements with different dimensions of a fetal head, tone of pelvic floor muscles and new gynecoid pelvis

The effects of varying simulation parameters and models on childbirth have been studied and reported.

1.6.1.4 Experimental study of pelvic moulding

The effects of sacrum and coccyx moulding on childbirth have been studied and reported.

1.6.1.5 Improvement of the existing neck model in BirthView

The original previous one-spring neck model could only restrict motion in rotation and compression/stretch. The improved neck model utilizes a six degrees-of-freedom spring-damper constraint in order to allow restriction in all three planes: sagittal, axial, coronal.

1.6.2 List of publications

In (Sadulaev et al., 2017) we developed a virtual reality program to assess strength and flexibility of a computer based model of a term fetus or newborn baby's neck. The software has a haptic/force feedback user interface which allows clinical experts to adjust the mechanical properties, including range of motion and mechanical stiffness of a newborn neck model, at runtime. The developed software was assessed by ten clinical experts in obstetrics. The empirically obtained stiffness and range of motion values corresponded well with values reported in the literature.

In (Lapeer et al., 2019) we presented a virtual reality-based simulation software of physiological childbirth. The results confirm the potential of the simulator as a predictive tool for problematic childbirths subject to patient-specific adaptations. The author of this thesis was involved in validation of total Lagrangian explicit dynamics method used to calculate soft tissue deformation in the simulation (see Section 4.5). In addition, the author was involved in running experiments for different positions of the fetal head in vertex presentation (see Figure 1.7). For the full list of contributions please refer to Section 4.5.2.

1.6.3 Other contributions

1.6.3.1 A device for measuring neck ROM

We developed a device in order to facilitate measuring of the range of motion of a fetal neck in three planes. The detailed description of the device is provided in Appendix B.

1.6.3.2 A clinical study of range of neck movements and muscle resistance in healthy newborn babies

We produced a protocol to measure range of neck movements in healthy newborn babies. The study was halted due to unforeseeable circumstances, however, the protocol can be used as a reference for future similar studies.

1.6.3.3 CT scans of a 6 month old baby's skull and neck

We acquired CT scans of a 6 month old baby's neck in order to calculate the dimensions of cervical vertebrae and intervertebral discs. The data has been used in the initial neck model. Since data of a younger baby was acquired later, the dimensions have not been used in the latest simulation. Nevertheless although by the age of 6 months a baby's neck is much stronger, considering lack of data on newborn's CT scans, these obtained scans can be useful for future development when a more detailed neck model is required for studying the effects of the simulation on soft tissues around the cervical vertebrae, i.e. to identify neck traumas.

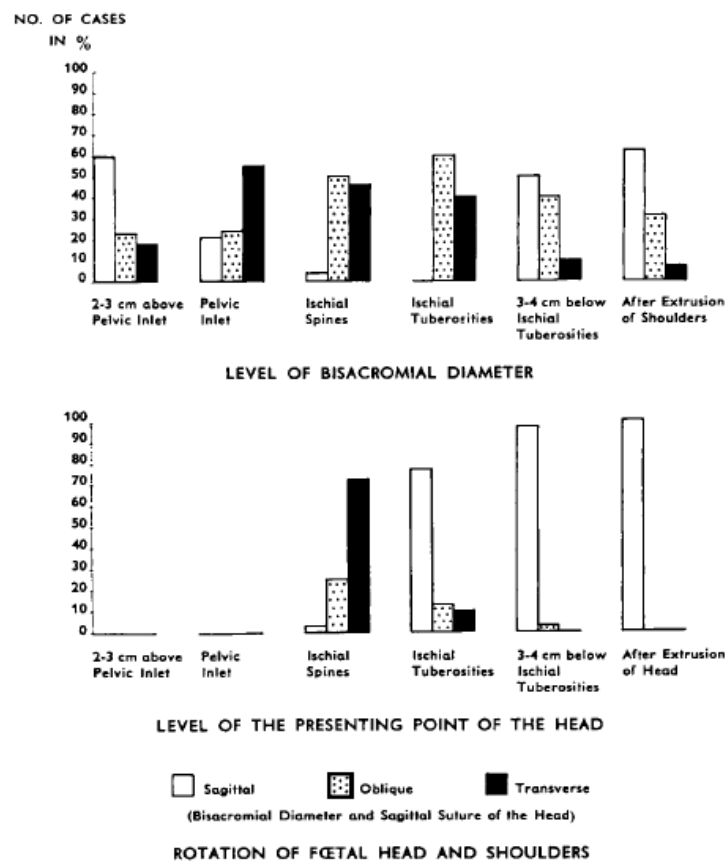


Figure 1.14: Diagram showing the positions of the fetal head and shoulders (bisacromial diameter) in the different stages of descent (Borell and Fernström, 1958). The upper diagram is showing the number of cases when the orientation of the fetal shoulders was either sagittal, oblique or transverse, at certain stations (positions), with respect to the pelvis. Similarly, the lower diagram is showing the orientations of the fetal head with respect to the pelvis.

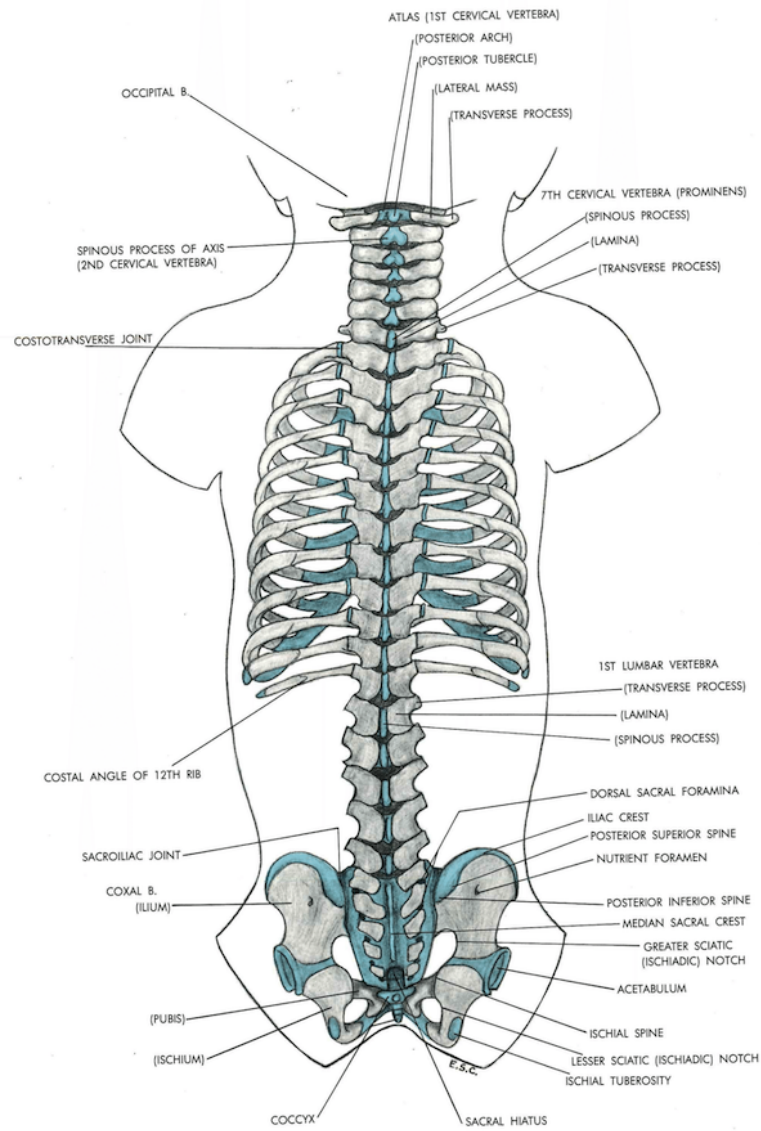


Figure 1.15: Infant Spine. Image from Crelin (1969).

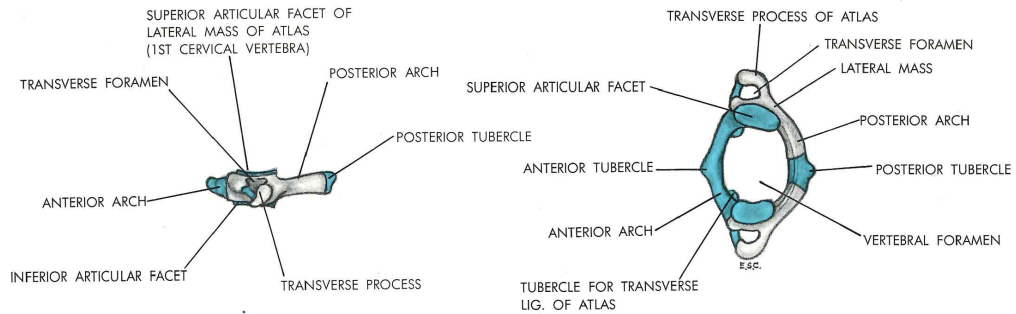


Figure 1.16: Atlas. Image from Crelin (1969).

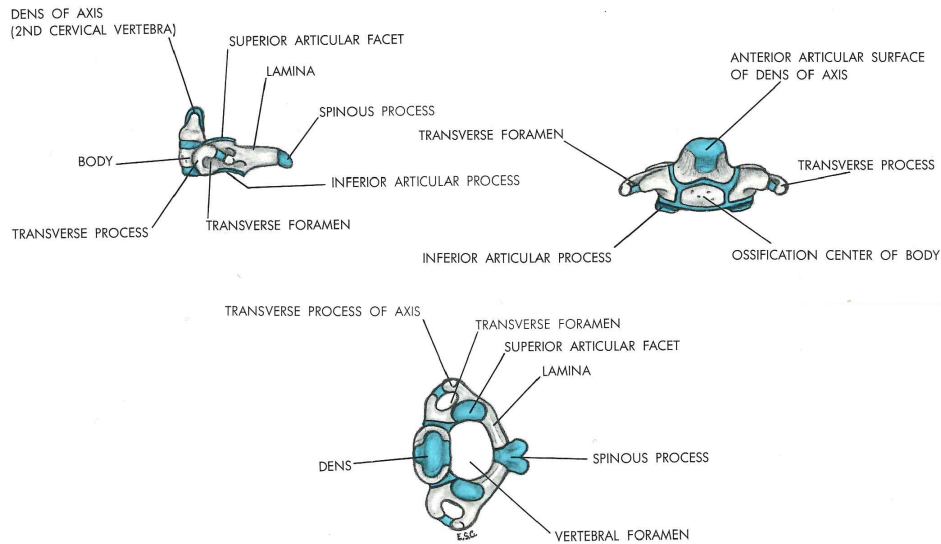


Figure 1.17: Axis. Image from Crelin (1969).

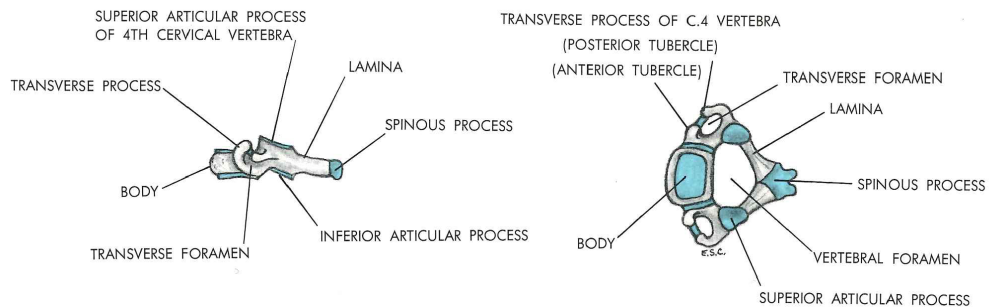


Figure 1.18: 4th Cervical Vertebra. Image from Crelin (1969).

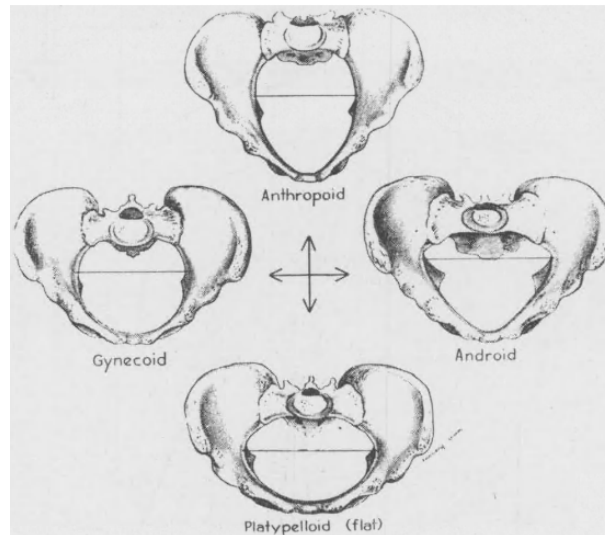


Figure 1.19: The four standard or pelvic types (Caldwell and Moloy, 1938).

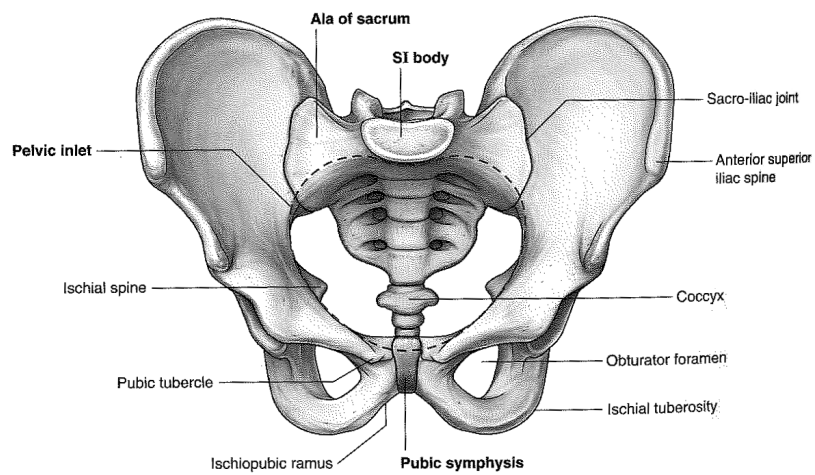


Figure 1.20: Human pelvis (Drake et al., 2015).

Chapter 2

Literature review

2.1 Introduction to Literature Review

This section reviews the latest research in biomechanical modelling of both an adult and pediatric cervical spine. It starts with describing the four main methods of the computational neck modelling and then it looks at the existing biomechanical neck simulation systems of adults. The conducted studies on the mechanical properties of the fetal spine are then presented followed by the review of existing computational models of newborn infants. Finally the studies on the range of motion of a newborn spine are briefly described.

Literature was primarily found through searches of related keywords in Google Scholar along with forwards and backwards citation analysis.

The following subsection sets the context of this literature review and gives an overview of what research has been carried out in the area of simulating the birthing process.

2.1.1 Virtual childbirth simulators

Virtual childbirth simulators can be potentially used as a planning tool for birth or an educational tool for students in obstetrics. A trivial example of the simulator being used in planning the birth, would be taking MRI or ultrasound scans of the maternal pelvis and the fetus, reconstructing their 3D models and running the simulator. Alternatively, instead of manually reconstructing the models, there

can be a library of the 3D models in the software, which allows selecting the pelvic models with dimensions and shapes corresponding to the ones in the MRI or ultrasound scans.

A more advanced simulator would run a dynamic process using an underlying model based on the Finite Element Method (FEM) and by varying the uterine contractions' force and frequency, the initial positions of the fetus and its shoulders as well as modelling its neck's strength, it would be possible to assess the level of risk for a physiologic birth, which would indicate that an assisted delivery or a Caesarean section is required. Another example of using a simulator would be to identify the maximum stretch ratio of the pelvic floor muscles to indicate the risk associated with stretch related pelvic floor injuries during childbirth.

There have been very few studies on simulating the first (and the longest) stage of labour, when the contractions become regular, the cervix dilates and the baby moves into the birth canal. During the first stage of labour, the fetal head subjected to pressures in the birth canal, may undergo deformation or moulding into an oblong shape. In one of the studies by Lapeer and Prager (2001) they presented a non-linear model of the deformation of a complete fetal skull, under the pressure of cervix. The results were in good agreement with clinical experiments.

On the contrary there are quite a few studies on simulating the second stage of labour (Li et al., 2010), when the fetus is undergoing the cardinal movements described in Section 1.2.5.

Li et al. (2008) developed finite element (FE) models of the female pelvic floor muscles and the fetal head to simulate vaginal delivery to test if athletes involved in high-intensity sports have a higher probability of being engaged in a prolonged labour as compared to non-athletes. The results had shown that the athletes required more force to push the fetal head as compared to non-athletes (45% increase in peak force was observed for athletes). According to the authors the purpose of the developed framework is to help clinicians assess the risk of natural versus caesarean birth.

Hoyte et al. (2008) developed a model of female pelvic floor muscles to study the levator ani muscle (LAM) stretch during childbirth. The results had shown that a maximum stretch was seen in the posterior-medial puborectalis. Also maximum stretch was increased with increasing stiffness of lateral levator attach-

ments. A few more studies were done to predict LAM stretch during birth, which mainly differ in the representation of the geometry of the LAM and the fetal head (Lien et al., 2004; Martin, 2007; Parente et al., 2009).

The above studies focused mainly on LAM stretch and by extension on the difficult birth scenarios related to the pelvic floor muscles' overstretch. The motivation behind the following studies is to develop a generic childbirth simulator, which is potentially capable of simulating LAM stretch as well as other difficult birth scenarios, such as shoulder dystocia, occipito-posterior position of the fetal head etc. Such a simulator would require to run in real-time, include the pelvic ligaments and floor muscles and have articulated shoulders, arms, neck, spine and chest for the fetus.

Gerikhanov et al. (2013) developed a childbirth simulator using only a rigid pelvic model and a rigid fetal head model. The mechanical contact interaction was implemented between the models. A number of experiments were run in the hope to observe the cardinal movements, which are observed in real life during normal labour. However only three out of seven cardinal movements were observed and it was concluded that a more complex geometry of the models is required as well as presence of the soft tissues, i.e. ligaments and pelvic floor muscles.

Lapeer et al. (2019) improved the model by Gerikhanov et al. (2013) and included the following models into their childbirth simulator: rigid body fetal head, rigid body maternal pelvis, basic neck implemented as a spring, FE deformable cervix, pelvic floor muscles and sacrospinous ligaments. Similarly, a series of experiments were run to test whether the simulator is capable of simulating all seven cardinal movements. As a result the simulator did successfully display the seven cardinal movements of the fetal head and trunk, which occur during physiological labour.

2.2 Four main schemes of the computational neck model

Finite element and multi-body modelling are the most popular modelling techniques used for development of a computational model of a cervical spine (Jalalian

et al., 2013). In addition, according to Lopik (2004) there are two more types of head-neck models, namely, continuum rod and two-pivot models, which are capable of simulating the general head behaviour, although less accurate than FE and multi-body models.

2.2.1 Continuum rod model

A one-dimensional continuum model of the spine was created by Cramer et al. (1976) as a curved homogeneous beam-column, which has infinite degrees of freedom. The model is focusing on the pilot ejection problem, however, it is suitable for any simulation with an acceleration applied in the midsagittal plane. A 10g acceleration was applied to the torso to study its dynamic response. The model predicted the configuration history, the axial force, shear force, bending moment and effective stress distributions along the spine for the impact situation. The model predictions are said to agree with pilot ejection injury data.

2.2.2 Two-pivot (three bodies) models

Two-pivot models consist of three rigid bodies, the head, neck and torso. The neck link represents the lumped properties of the seven cervical vertebrae.

Tien and Huston (1987) developed a three-body model of the head/neck system, which simulated the gross motion of the head as accurately as the analogous nine-body model by Huston et al. (1976). Springs and dampers were used in order to simulate combined properties of the discs, ligaments and muscles. The developed model was validated against sled¹ experimental data (Ewing et al., 1977). According to the authors, although the developed neck model is not able to describe the mechanics of the neck in detail, it is capable of efficiently predicting global head positions and orientations. Similar two-pivot neck models have been developed and validated by Bosio and Bowman (1986) and Wismans et al. (1986, 1987).

¹Sled test systems are used in automotive industries to reproduce the dynamic conditions of a crash event in a controlled environment (Exponent, 2019)

2.2.3 Multi-body models

In multi-body or discrete parameter models, head and vertebrae are represented by rigid bodies, that are connected by massless spring and damper systems, representing intervertebral soft tissues and muscles. Ligaments, discs, facet joints and sometimes muscles are usually lumped together, resulting in computationally efficient modelling (Van Lopik and Acar, 2007).

Panjabi (1973) developed a general method for producing a discrete parameter model and constructing governing equations of motion of the spine structure. The anatomic structure is represented by any combination of rigid bodies with 6 degrees of freedom and connecting tissues represented by springs and dampers.

Belytschko et al. (1973) developed a mathematical model for a three-dimensional force analysis of the human vertebral column. The vertebrae are represented as rigid bodies, while the discs, ligaments, and connective tissues are represented by spring elements. An incremental stiffness method which accounts for nonlinearities due to large displacements is used.

Deng and Goldsmith (1987) developed a lumped-parameter model of the human head, cervical vertebrae and upper torso (T1 and T2) with 15 pairs of muscles. These rigid bodies were connected by lumped intervertebral joints, described by a stiffness matrix relating the force (moment) and translation (rotation).

De Jager et al. (1994) adapted Deng and Goldsmith (1987)'s head-neck model and implemented the model in the multibody software package Madymo¹. The new model consisted of a rigid body head, neck (C1-C7) and first thoracic vertebra. These were connected by linear viscoelastic intervertebral joints and nonlinear elastic Hill type muscle elements.

Lopik (2004) presents development and validation of a detailed multi-body computational model of the head and cervical spine of an adult in the upright posture. The model comprises nine rigid bodies: the head, seven cervical vertebrae of the neck and the first thoracic vertebra. These are interconnected by non-linear viscoelastic intervertebral discs elements, non-linear viscoelastic ligaments and supported through frictionless facet joints. The model includes eighteen muscle

¹Madymo is a worldwide standard software for the analysis of occupant safety in the automotive and transport industries (Tass International, 2019).

groups and 69 individual muscles.

Discs elements are represented by ‘bushing elements’, which allows stiffness and damping properties to be assigned to a joint for every degree of motion. Ligaments are modelled with spring-damper elements.

Lee and Terzopoulos (2006) introduced a biomechanical model of the human head-neck system for computer animation. The model consists of 7 cervical vertebrae coupled by three rotational degrees of freedom (DOF) joints and 72 neck muscles. A rotational damped spring has been attached to each joint in order to simulate the stiffness of the ligaments and disks using the following equation:

$$\tau_s = -k_s(q - q_0) - k_d\dot{q} \quad (2.1)$$

where q is the joint angle, q_0 is the joint angle in the natural, rest configuration, k_s is the spring stiffness, and k_d is the damping coefficient.

Numerical integration method: explicit Euler integrator.

To simulate the muscles, Lee and Terzopoulos (2006) employed a popular muscle model in biomechanics research, which is known as Hill’s muscle model (Hill (1938), Zajac (1988)). In addition, a hierarchical neuromuscular control model has been developed to simulate the biological motor control mechanisms of the head (head stabilizing).

Luo et al. (2013) presented a similar physical human neck model, partially based on the work of Lee and Terzopoulos (2006). The cervical vertebrae have also been modelled as an articulated multibody system (using springs) and the muscles have been implemented as a Hill-type muscle model as well.

2.2.4 Finite element models

Finite element models of the neck are able to model a highly detailed representation of a cervical spine geometry. Each anatomical component of the spine is broken down into a number of deformable elements (finite elements) with respective biological properties. However, these models are complex and have many parameters and, hence, computationally less efficient and difficult to validate as compared to the multi-body models (De Jager et al., 1994).

2.3 Mechanical properties of the fetal/pediatric spine

This section provides the most recent investigations of the mechanical properties of the pediatric cervical spine.

Most of the studies available on the mechanical properties of the neck has been completed using either full grown adults or juvenile animals. Nevertheless, there are a few studies that have analysed the newborn spine under tensile, rotational and bending loading conditions (Ouyang et al., 2005; Luck et al., 2008; Luck, 2012; Nuckley et al., 2013a). In addition there is unpublished data provided by Prange and Myers to Coats and Margulies (2008) through personal communication in 2004 describing the bending moment of the C4-5 segment from a 24-day-old infant.

2.3.1 Luck et al. (2008)

A number of non-destructive and destructive tests under tensile loading conditions, have been conducted by Luck et.al on post-mortem human subjects (PMHS).

The non-destructive study has been conducted first on the osteoligamentous head-neck complexes of eighteen PHMS infants aged from 20 weeks gestation to 14 years. Any musculature was removed from the cervical spine. Tensile testing was initially conducted on the whole cervical spine and then it was separated into three segments (O-C2, C4-C5 and C6-C7). After non-destructive tests were completed, each segment was loaded until failure. The tensile stiffness of the whole spine ranged between 5.3 and 70.1 N/mm for all PHMS subjects and from 5.3 to 7.9 N/mm for infants. The entire cohort of specimen had an ultimate strength for the upper cervical spine between 173.6 and 2960 N and for the lower cervical spine from 142 to 1757 N (see Tables 2.1, 2.2, 2.3).

The acquired data supported the usage of juvenile animal surrogates (Pintar et al., 2000; Ching et al., 2001; Nuckley and Ching, 2006) to fairly accurately estimate the stiffness of a paediatric cervical spine (Figure 2.1). However, the surrogates may not as accurately estimate the spine strength.

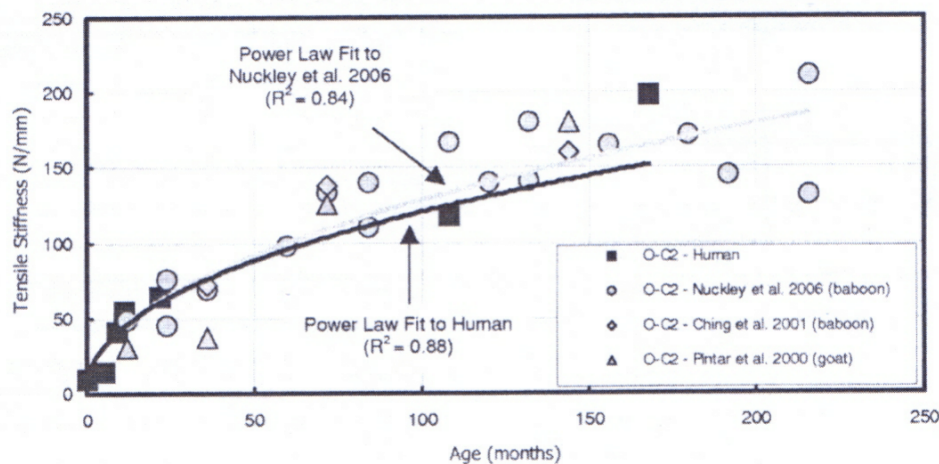


Figure 2.1: Tensile stiffness (N/mm) of the upper cervical spine (O-C2) segment from Luck et al. (2008) compared to three previous juvenile animal surrogate studies

2.3.2 Ouyang et al. (2005)

Ouyang et al. (2005) also studied biomechanics of the paediatric osteoligamentous cervical spine both on tension and bending. However, the test subjects ranged from 2-14 years of age. Each specimen was subjected to quasi-static nondestructive flexion-extension bending tests with subsequent nondestructive tensile tests. The nondestructive tests followed by tensile distraction loading to failure.

The failure loads from both studies (Luck et al., 2008; Ouyang et al., 2005) compared well considering the same age group in test subjects. However, both studies significantly differed when compared to the results obtained in the study by Duncan (1874), where five whole PHMS infants were subjected to tensile load until decapitating. The failure loads of Duncan's study were twice as large as those seen by Luck et al. This indicates that soft tissue structures in the neck significantly affect load bearing capacity of the newborn cervical spine. Similar findings were found by Chancey et al. (2003) and Van Ee et al. (2000) that musculature significantly impacts the dynamics and failure properties of the adult cervical spine in tension.

2.3.3 Luck (2012)

A number of non-destructive tests under bending (flexion/extension) loading conditions, have been performed by Luck et.al on twenty-two unembalmed cervical spine cadaver specimens. The ages of the specimens ranged from 29 weeks gestation to 18 years old. The spines were sectioned into three segments (O-C2, C4-C5 and C6-C7). Each segment was tested under load both in flexion and extension.

The flexion stiffness for the first segment (O-C2) ranged from 0.0033 to 0.0189 Nm/degree, whereas extension was between 0.0218 and 0.0164 Nm/degree for perinatal, neonatal and pediatric PMHS (see Tables 2.1, 2.2, 2.3).

2.3.4 Nuckley et al. (2013a)

A number of non-destructive tests in tension, compression, flexion, extension, lateral bending and axial rotation were performed on eleven human cadaver cervical spines aged from 2 to 28 years old (see Tables 2.4, 2.5 and 2.6). The cervical spines were dissected into segments: C1-C2, C3-C5 and C6-C7. After measuring their intact biomechanical responses each segment was loaded to failure in order to measure their tolerance in tension, compression and extension.

Table 2.1: Biomechanics of pediatric cervical spine's section O-C2 (Luck et al., 2008; Luck, 2012; Luck et al., 2013). Flexion and extension are given in Nm/degrees. Compression and tension are given in N/mm.

Specimen	Age (month)	Flexion (Nm/deg)	Extension (Nm/deg)	Compression (N/mm)	Tension (N/mm)
02P	0				
07P	0	0.0033	0.0218	4	11.9
08P	0			1.5	10.5
09P	0				
10P	0				
13P	0	0.0030	0.0050	1.5	12.2
05P	0.03	0.0012	0.0069	2.2	7.4
03P	0.1			1.8	11.2
06P	0.37	0.0180	0.0062	4.1	7.1
11P	0.53				
04P	0.8	0.0058	0.0034	0.9	9.3
12P	5	0.0084	0.0180	9.9	14.5
14P	9	0.0084	0.0105	20.7	41.5
15P	11	0.0080	0.0103	36.5	54.4
16P	18				
17P	22	0.0091	0.0316	41	64
24P	72	0.0122	0.0174	110.6	
19P	84	0.0111	0.0223		
18P	108	0.0076	0.0226	71.7	118.1
20P	144	0.0131	0.0234		
01P	168	0.0145	0.0221		199
21P	192	0.0138	0.0266		
22P	204	0.0150	0.0174		
23P	216	0.0189	0.0164		

Table 2.2: Biomechanics of pediatric cervical spine's section C4-C5 (Luck et al., 2008; Luck, 2012; Luck et al., 2013). Flexion and extension are given in Nm/degrees. Compression and tension are given in N/mm.

Specimen	Age (month)	Flexion (Nm/deg)	Extension (Nm/deg)	Compression (N/mm)	Tension (N/mm)
02P	0				
07P	0	0.0053	0.0754	27.4	46.1
08P	0				
09P	0	0.0154	0.0220	18.6	50.6
10P	0	0.0071	0.0233	27.5	35.8
13P	0	0.0115	0.0164	33.1	61.4
05P	0.03	0.0142	0.0236	25.7	50.4
03P	0.1			40.3	54.2
06P	0.37	0.0101	0.0237	20.4	50.5
11P	0.53	0.0141	0.0233	19.2	35.5
04P	0.8	0.0135	0.0274	25.3	42.8
12P	5	0.0302	0.0236	32.8	58.2
14P	9	0.0212	0.0465	100.9	114.4
15P	11	0.0243	0.0599	109.8	141.8
16P	18			138.6	
17P	22	0.0263	0.0512	93	153.1
24P	72	0.0294	0.0421	227.7	
19P	84	0.0621	0.1388	179.2	
18P	108	0.0306	0.1204		
20P	144	0.0397	0.1963	180.5	
01P	168				
21P	192	0.0570	0.2029	202.9	
22P	204	0.0463	0.1836	318	
23P	216	0.0351	0.0896	235.9	

Table 2.3: Biomechanics of pediatric cervical spine's section C6-C7 (Luck et al., 2008; Luck, 2012; Luck et al., 2013). Flexion and extension are given in Nm/degrees. Compression and tension are given in N/mm.

Specimen	Age (month)	Flexion (Nm/deg)	Extension (Nm/deg)	Compression (N/mm)	Tension (N/mm)
02P	0				
07P	0	0.0159	0.0299	21.7	44.4
08P	0				
09P	0	0.0216	0.0273	24	36.7
10P	0	0.0083	0.0356	13.6	37.1
13P	0	0.0176	0.0155	22.7	39.4
05P	0.03	0.0451	0.0212	36.4	45.2
03P	0.1			10	42.2
06P	0.37	0.0249	0.0195	30.1	50.8
11P	0.53	0.0149	0.0215	39	61.5
04P	0.8	0.0072	0.0301	38.3	34.2
12P	5	0.0314	0.0224	22	43.5
14P	9	0.0176	0.0403	61.9	103
15P	11	0.0219	0.0291	91.7	107.6
16P	18			125.2	
17P	22	0.0290	0.1642	86	93.1
24P	72	0.0279	0.0610	213	
19P	84	0.0531	0.1518		
18P	108	0.0339	0.0778	192.6	255.9
20P	144	0.0477	0.0790		
01P	168				
21P	192	0.0727	0.2824	189.6	
22P	204	0.0545	0.1128	301.1	
23P	216	0.0351	0.0758	282.5	

Table 2.4: Biomechanics of pediatric cervical spine's section C1-C2 (Nuckley et al., 2013b).

Specimen #	Age (years)	Flexion (Nm/rad)	Extension (Nm/rad)	Lateral bend (Nm/rad)	Axial rot (Nm/rad)	Compression (N/mm)	Tension (N/mm)
C1-C2							
01-109	2	–	–	28.8	8.8	694.2	155.8
01-103	3	30.5	37.6	50.4	17.7	1031.3	141.8
01-108	5	–	–	45.8	17.8	962.7	227.0
01-106	8	37.2	45.6	–	–	1254.7	195.8
01-101	9	35.2	33.1	–	–	1264.2	205.2
01-102	11	33.1	37.6	43.0	27.2	1778.9	252.9
01-110	13	42.2	48.4	60.7	27.2	1450.5	228.0
01-104	16	38.3	51.2	68.1	29.7	1317.2	211.1
01-111	18	44.2	52.0	71.7	28.7	1805.2	254.6
01-105	22	43.8	38.1	74.5	23.9	1409.1	268.4
01-107	28	–	50.4	65.6	16.1	2103.7	268.0

Table 2.5: Biomechanics of pediatric cervical spine's section C3-C5 (Nuckley et al., 2013b).

Specimen #	Age (years)	Flexion (Nm/rad)	Extension (Nm/rad)	Lateral bend (Nm/rad)	Axial rot (Nm/rad)	Compression (N/mm)	Tension (N/mm)
C3-C5							
01-109	2	18.3	12.3	23.7	7.9	393.0	95.0
01-103	3	21.3	22.8	30.8	15.5	585.5	108.1
01-108	5	27.4	16.7	32.0	18.3	682.5	131.5
01-106	8	21.0	21.2	37.3	20.0	916.2	185.5
01-101	9	–	29.6	29.9	18.4	733.5	139.3
01-102	11	31.5	25.7	34.9	16.1	986.2	129.3
01-110	13	31.7	24.1	33.6	18.8	863.7	–
01-104	16	29.6	21.6	39.2	18.1	–	251.2
01-111	18	33.2	29.8	34.7	20.3	1172.6	241.7
01-105	22	30.0	25.5	42.5	15.5	1167.7	229.5
01-107	28	–	24.0	42.1	25.5	1293.6	260.0

Table 2.6: Biomechanics of pediatric cervical spine's section C6-C7 (Nuckley et al., 2013b).

Specimen #	Age (years)	Flexion (Nm/rad)	Extension (Nm/rad)	Lateral bend (Nm/rad)	Axial rot (Nm/rad)	Compression (N/mm)	Tension (N/mm)
C6-C7							
01-109	2	10.6	10.0	21.6	15.9	537.3	167.7
01-103	3	45.3	47.5	41.3	30.3	–	178.8
01-108	5	26.4	18.9	42.5	28.2	760.1	264.1
01-106	8	19.4	42.5	55.2	33.2	1410.0	223.9
01-101	9	43.5	25.7	–	38.8	1025.0	240.9
01-102	11	28.7	56.7	51.3	41.6	1013.8	220.8
01-110	13	44.4	47.4	54.4	41.5	1203.0	271.2
01-104	16	41.6	58.2	44.5	30.0	1030.5	322.0
01-111	18	57.1	57.7	62.9	44.9	1418.3	349.0
01-105	22	54.4	–	63.0	39.7	1393.7	255.5
01-107	28	84.2	66.1	79.4	47.9	1498.6	406.9

2.4 Existing computational models of newborn infants

There are a limited number of computational newborn neck models due to paucity of paediatric biomechanical data. Up until 2012 the existing computational models, mainly of anthropomorphic testing devices (ATDs) or crash test dummies, have been utilizing either scaled adult or animal characteristics.

2.4.1 Q0 ATD finite-element model

There are three popular newborn Anthropomorphic Test Dummies (ATD), namely Civil Aeronautical Medical Institution (CAMI) newborn, the P0 and Q0. The CAMI newborn weighs 3.4 kg and has a standing height of 50.8 cm. It was designed for testing aircraft restraints. The P0 consists of a head, torso, arms and legs as a single unit. The torso, arms and legs are a single moulded piece of polyurethane covered with polyvinyl chloride (PVC) skin. The spine in this ATD is represented with a steel spring. However, both the P0 and the CAMI newborn are very simple ATDs and are of little practical value in terms of biofidelity and subsequent accuracy (Bondy et al., 2014).

The Q0 represents a six weeks old baby weighing 3.4 ± 0.05 kg with a sitting height of 35.5 ± 0.7 cm (First Technology Safety Systems, 2008). The ATD was designed to accept impacts from any direction and allows measurement of the upper neck forces and moments as well as accelerations of head, chest and pelvis. The neck is a series of rubber and metal discs connected at one end to the head, which is made of a polyurethane covered with a vinyl skin.

Humanetics has developed a finite element model of the Q0 (Humanetics ATD, 2017), which according to Bondy et al. (2014) was the only computer model of a small infant that was known to exist in 2014. The mechanical properties on the flexion-extension of a neck were scaled from adult data published by Mertz and Patrick (1971). The scaling factor was based on the study by Yamada et al. (1970), who determined the calcaneal tendon stiffness and failure stress for adults and children.

2.4.2 Nita infant model

A finite element/multi-body biomechanical model of a newborn has been developed by **Bondy et al. (2014)**, which was designed for an analysis of airway patency for infants in modern automotive child restraints¹. The geometry of the model was derived from a Nita newborn hospital training mannequin, which weights 1.81 kg and has a height of 40.64 cm. The model consists of 17 parts: eight upper and lower limb segments, the torso, head, and a seven-segment neck.

The neck is comprised of seven shell rigid bodies using the properties of steel and is a series of alternating spherical and translational joints. The joint stiffness properties of the neck are based on the publications by Luck et al. (2008), Coats and Margulies (2008) and Ouyang et al. (2005). An initial Nita model incorporated data from Ouyang et al. to model the stiffness of the neck under bending. However, since the youngest subject in the study was 2 years old, the latest model adapted data from Coats and Margulies (2008) to model the stiffness of the neck under bending, i.e. flexion and extension. Also the model directly incorporates the Luck's force-displacement properties for the translational joints (Luck et al., 2008). Finally the model has been validated against the studies of the biomechanics of shaken baby syndrome (SBS), infant falls and Q0 anthropomorphic testing device (ATD).

2.4.3 MD Adams infant model

The computational model of a nine-month-old infant was designed for the investigation of infant head injury by shaking. The geometry of the model was derived from serial sagittal magnetic resonance images (MRIs) from two infant subjects, aged 2 weeks and four months. Both images were used to extract detailed dimensions for the anatomical features of the head and scaled accordingly.

The infant spine (C0-L5) of the model is comprised of 24 cylindrical bodies and 24 joints. Vertebral body heights and intervertebral spaces were selected based on scaled data acquired from the MRIs. The size of the head is 2.3 kg with centre of mass at 14.5 mm anterior and 33.5 mm superior to the C0 joint,

¹The computer model may be made available to researchers upon request through the corresponding author (Bondy et al., 2014).

in the sagittal plane. The locations of the head, torso and spinal rigid body models corresponding to the data are derived from the MRI of the four month old subject.

The cervical spine is attached to the head and torso by fixed joints at C0 and C7 respectively. Cervical spine joints are restricted to a single rotational degree of freedom (flexion-extension). “Linear relationships are developed for the quasi-static and rate-dependent vertebral stiffness properties, in flexion-extension, across all cervical joints”:

$$\tau = -k\theta - c\omega \quad (2.2)$$

where k is *quasi-static stiffness*, θ is *angular displacement*, c is *rate-dependent stiffness or damping* and ω is *angular velocity*.

In other words, a torsional form of a spring-damper model has been employed in order to simulate the cervical spine.

The quasi-static flexion-extension stiffness properties for a nine-month-old infant were obtained from the paper describing child neck strength characteristics using an animal model (Pintar et al., 2000) and is equal to 0.242 Nm/deg. The rate-dependent stiffness was identified to be in range of 5-15 Nmm/s/deg, which resulted in a simulation that conformed to a physiological range of motion described in the paper by Jones et al. (2008).

The accuracy of the model was validated against paediatric motion analysis data, collected from one female infant between 3 and 18 months, which also included very gentle oscillations (shakes) at 9 months of age. The developed neck model was assessed against the recorded motion of the head relative to torso.

Discussion Bondy et al. (2014) stated that the finite element model of the Q0 ATD is the only computer model of a small infant that is known to exist. Q0 is designed for frontal, side, rear crash configurations, which implies the existence of calculated stiffness coefficients for the side rotation, flexion/extension and lateral bending.

Nevertheless, the biomechanical properties of the newborn neck, was scaled from the adult data. Also ATDs are designed to be robust and durable devices that will not be easily damaged, which might affect the biofidelity of the model.

The advantage of an infant model developed by Bondy et al. (2014) is that it utilized data from the studies on mechanical properties of the pediatric cervical spine, which obviously makes it more accurate. However, the model is significantly smaller than the average newborn (Janssen et al., 2007). Furthermore, the model is limited to bend in the sagittal plane only (flexion/extension).

2.5 Range of motion of an infant skull

It is essential to have information on range of motion (ROM) of infant skulls to recognize extraordinary rotations during simulation. Reference values for range of motion (side rotation and lateral bending) of the neck in infants have been reported by Öhman and Beckung (2008). ROM was measured in 38 healthy infants at the ages of 2, 4, 6 and 10 months. For side rotation the mean ROM was 110° and for lateral bending it was 70° . Mean measurements of rotation and lateral bending for the abovementioned infant group is presented in Table 2.7. Surprisingly, the mean ROM in the table tends to increase with age on rotation. However, a bigger number of tested subjects at an extended range of ages may lead to observing the opposite.

Table 2.7: Mean Measurements of Rotation and Lateral Flexion at the Ages of 2, 4, 6, and 10 Months

Mean	2 months ($^\circ$)	4 months ($^\circ$)	6 months ($^\circ$)	10 months ($^\circ$)
Rotation	105.2	111.8	112.4	111.7
Lateral bending	68.1	69.5	69.2	70

From Öhman and Beckung (2008)

Luck (2012) presented ROM under flexion/extension bending of the cervical segments (O-C2, C4-C5 and C6-C7) in nine perinatal and neonatal specimens (29 weeks gestation to 24 days old) and thirteen infant to young adult specimens (5 month to 18 years old). Total ROM in flexion and extension was observed to decrease with age as can be seen in Table 2.8 and Figure 2.2.

Note that segments C2-C3 and C5-C6 are not included in the table. Therefore, the total ROM under flexion/extension bending would be bigger for the presented

Table 2.8: Flexion and Extension Range of Motion (ROM) for Perinatal, Neonatal and Pediatric PMHS from the paper by Luck (2012). In order to get the age in days multiply by factor 30.4167.

PMHS ID	Age (months)	O-C2	C4-C5	C6-C7
		ROM (degrees)	ROM (degrees)	ROM (degrees)
07P	0	92.5	28.3	31.6
13P	0	95.9	25.9	28.9
05P	0.03	114.5	31.4	29.5
06P	0.37	92.0	28.4	21.5
04P	0.8	78.2	21.1	30.5
12P	5	52.7	16.1	15.2
15P	11	53.0	10.4	12.6
17P	22	47.1	12.0	7.6
24P	72	41.0	10.0	7.0
20P	144	28.4	3.5	3.9
21P	192	41.6	2.4	1.8

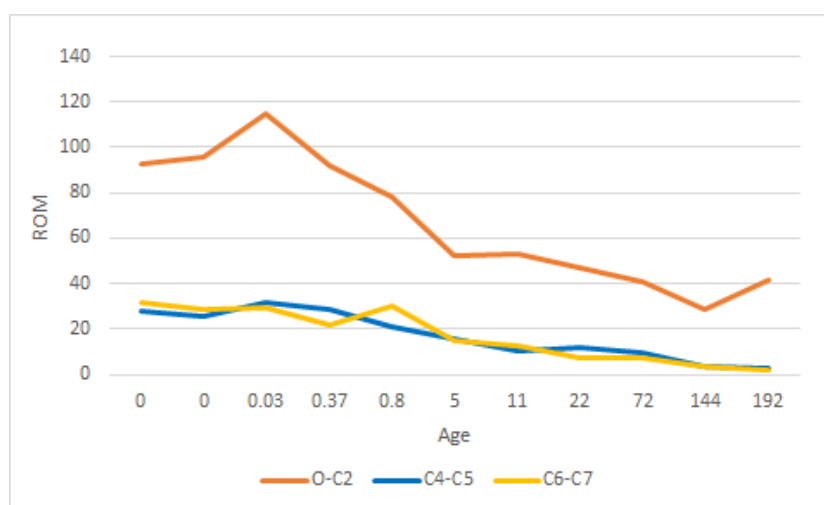


Figure 2.2: Flexion and Extension Range of Motion (ROM) for Perinatal, Neonatal and Pediatric PMHS for the cervical spine's segments O-C2, C4-C5, C6-C7 (Luck, 2012).

osteoligamentous segments. However, the real ROM may be significantly smaller as all neck musculature, subcutaneous fatty tissue, and skin were removed before the testing.

2.6 Conclusion

Several computational neck models and mechanical properties of the pediatric cervical spine have been reviewed in this section. Firstly, although a few studies are conducted and validated on the mechanical properties of infants, all of them were limited to sagittal plane motion only, which corresponds to flexion/extension bending. Secondly, the only computational neck model which attempts to simulate mechanical response of the fetal neck in axial and coronal planes is the Q0 ATD model (First Technology Safety Systems, 2008). However, the mechanical properties of the neck in the model were scaled from adult data and require further validation. To the author's best knowledge a validated computational fetal cervical spine model suited for all possible rotations does not exist. Therefore, there is a need for the development of a biofidelic fetal neck model capable of accurately simulating a fetal neck response in any direction.

Chapter 3

Developing a computational fetal neck model

3.1 Overview

This chapter covers the methods that have been employed in the validation of the existing childbirth simulator and the development of a new computational fetal neck model.

The following section describes the meshes used in the simulator, the sources of raw data and the software/techniques used to process the models.

Then the methods used to predict the missing stiffness values for a newborn's neck are described. The next section describes the validation of a neck's range of motion and the basic neck model.

The remainder of the chapter describes the developed computational neck models and the software used to assess strength and flexibility of the newborn's neck BirthViewH. The software is using two haptics devices (Phantom Omni) to validate the resistance of the skull, during bending and rotation.

Finally the developed neck models are discussed together with the validation from experimental studies.

3.2 Methodology

3.2.1 Overview

This section covers the techniques and methods used in the development of the fetal neck model. First and foremost, the methods used to acquire complete mechanical properties of the fetal neck are discussed. Then the developed simulation software BirthViewH is described used for the validation of computer neck models. The methods used to simulate the behaviour of intervertebral discs and ligaments are then described such as ball and socket joints, spring-damper systems and 6dof bushing elements. Finally the techniques and software used for measuring range of motion (ROM) and validating motion of the computer neck models are presented.

3.2.2 Complete mechanical properties of the fetal neck

3.2.2.1 Overview

This section is concerned with predicting the missing stiffness values for newborns' cervical spine segments. To the best of the author's knowledge, the only available stiffness data of newborns' cervical spine segments is published by Luck (2012). The data for 0-18 years old samples are presented in Tables 2.1, 2.2 and 2.3 for the following segments: O-C2, C4-C5, C6-C7. These tables contain stiffness values of the segments in flexion, extension, compression and tension. The only missing values are for axial rotation and lateral bending. It is worth mentioning that, although all these values were initially published in Luck's thesis, the flexion and extension values have never been published anywhere else.

Nuckley et al. (2013a) measured bending stiffness of the cervical spine segments (C1-C2, C3-C5 and C6-C7) of 2-28 years old samples in all planes, including lateral bending and axial rotation (see Tables 2.4, 2.5 and 2.6).

In this section we combined the two datasets Luck (2012); Nuckley et al. (2013b) in order to find the missing axial rotation and lateral bending stiffness values.

The initial method for finding the missing values was multiple imputation

(Heitjan and Little, 1991) using predictive mean matching, however, this did not produce the expected results and yielded implausible values.

3.2.2.2 Inconsistency in units

The reported flexion, compression, axial rotation and lateral bending stiffness data by Nuckley et al. (2013a) were presented in Nm/rad and, therefore, needed to be converted to Nm/degrees to correspond to the stiffness data by Luck (2012).

The following equation is used in order to convert a radian into a degree:

$$\alpha_{degrees} = \frac{\alpha_{radians}}{\pi} \times 180^\circ = \frac{1}{3.14159} \times 180^\circ \simeq 57.29578^\circ \quad (3.1)$$

In order to convert the stiffness values from Nm/rad to Nm/degrees the former needs to be divided by the calculated 57.29578. The values then were rounded down to two decimal places as in Tables 2.1, 2.2 and 2.3.

3.2.2.3 Inconsistency in segments

Nuckley et al. (2013a) measured stiffness of the following cervical spine segments: C1-C2, C3-C5 and C6-C7. Luck (2012) measured stiffness for O-C2, C4-C5 and C6-C7. C1-C2 and O-C2 are directly comparable due to occiput being attached to the first vertebra C1. However, C3-C5 and C4-C5 are not directly comparable due to the fact that the former includes the additional segment C3-C4.

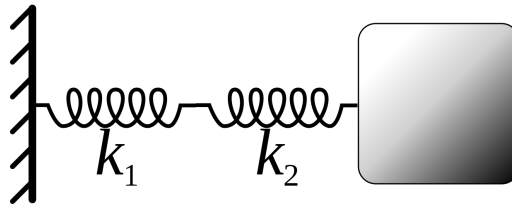


Figure 3.1: Springs in series

In order to find the stiffness of C3-C4, we assume that all the segments, starting with C3 and going all the way down to C7 are typical and similar to one another (Bogduk and Mercer, 2000). The cervical spine segments C3-C4 and

C4-C5 can be represented as two springs connected in series (see Figure 3.1) with their corresponding stiffnesses equal to each other (k_1 is equal to k_2).

The following formula is used in mechanics to calculate the spring stiffness that is equivalent to a system of two springs in series:

$$\frac{1}{k_{eq}} = \frac{1}{k_1} + \frac{1}{k_2} \quad (3.2)$$

Assuming that k_1 is equal to k_2 (k_{12}) we arrive at:

$$\frac{1}{k_{eq}} = \frac{2}{k_{12}} \quad (3.3)$$

Further simplifying we arrive at the final equation for finding k_1 and k_2 :

$$k_{12} = 2k_{eq} \quad (3.4)$$

3.2.2.4 Combining datasets

Once the datasets were combined into a single table, there was a discrepancy in flexion and extension values. Nuckley et al. (2013a) reported much higher results for the specimen of the same age as compared to the values reported by Luck (2012). This is probably due to having applied smaller loads during the measurements by Luck (2012). Nevertheless Ouyang et al. (2005) also reported bending stiffness (flexion) values for 2-18 years old specimen, which are in line with the data by Nuckley et al. (2013a). Therefore, an assumption was made that there is a scaling error in the data by Luck (2012).

For the O-C2 segment the stiffness is around 57 times smaller than the corresponding values reported by both Ouyang et al. (2005) and Nuckley et al. (2013a). It seemed to be a conversion error from degrees to radians, i.e. the results were converted to radians, but reported in degrees.

For the C4-C5 and C6-C7 the stiffness is around 100 times smaller and, hence, the previous assumption did not hold.

For that reason it appears to be unreasonable to use these flexion and extension values to predict the missing lateral bending and axial rotation values. An alternative approach was taken and is described in Section 3.2.2.5.

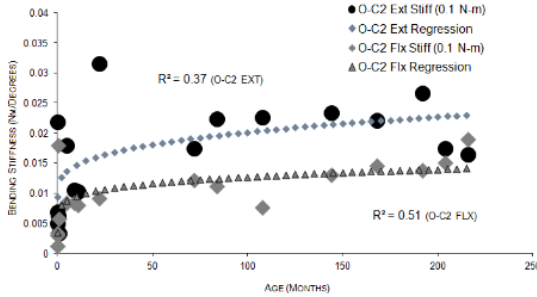


Figure 3.2: Flexion and extension stiffness in O-C2 (Luck, 2012)

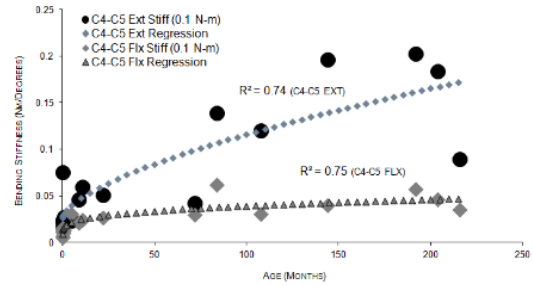


Figure 3.3: Flexion and extension stiffness in C4-C5 (Luck, 2012)

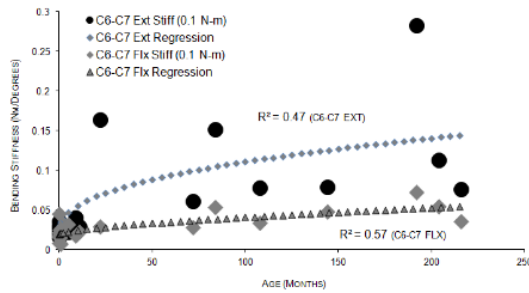


Figure 3.4: Flexion and extension stiffness in C6-C7 (Luck, 2012)

3.2.2.5 Logarithmic regression

The data by Luck (2012) produces a logarithmic curve (see Figures 3.5, 3.6, 3.7) and ideally should not be affected by the scaling factor, provided that all the data was scaled (see Figures 3.2, 3.3 and 3.4).

Therefore, a logarithmic regression was implemented on Nuckley’s dataset to fit the logarithmic curve and find the missing values for newborns, including the excluded flexion and extension.

The produced logarithmic models were used in order to predict the missing values for newborns. In case of axial rotation in the segment C1-C2, the equation $y = 0.0471\ln(x) + 0.1776$ was produced by logarithmic regression. Since the natural logarithm of 0 does not exist, we converted the age of the specimen to number of days instead of months and made an offset of the whole data by one. Hence, for a one day old specimen, by substituting x with 1 in the equation, the

stiffness value is calculated to be 0.1776.

The predicted stiffness values for newborns are summarized in Tables 3.1, 3.2 and 3.3. Stiffness values for the following segments are still missing: C2-C3, C3-C4 and C5-C6 due to lack of available data. These values will be approximated from the known adjacent segments in the neck models. Hence, C2-C3 is set to be the same as C1-C2, C3-C4 is the same as C4-C5 and C5-C6 is the same as C6-C7.

Table 3.1: Complete predicted stiffness values for the segment C1-C2 in newborns. Compression and tension are given in N/m. Flexion, extension, lateral bending and axial rotation in Nm/deg.

C1-C2						
Age (month)	Flexion	Extension	Compression	Tension	Lateral bending	Axial rotation
0	0.1650	0.2836	4000	11900	0.0201	0.1776
0	0.1500	0.2836	1500	12200	0.0201	0.1776
0.03	0.0600	0.2865	2200	7400	0.026	0.179
0.37	0.9000	0.3140	4100	7100	0.085	0.192
0.53		0.3246			0.108	0.198
0.8	0.29	0.3403	900	9300	0.142	0.205

Table 3.2: Complete predicted stiffness values for the segment C4-C5 in newborns. Compression and tension are given in N/m. Flexion, extension, lateral bending and axial rotation in Nm/deg.

C4-C5						
Age (month)	Flexion	Extension	Compression	Tension	Lateral bending	Axial rotation
0	0.0007	0.1204	27400	46100	0.2527	0.0029
0	0.0007	0.1204	18600	50600	0.2527	0.0029
0	0.0007	0.1204	27500	35800	0.2527	0.0029
0	0.0007	0.1204	33100	61400	0.2527	0.0029
0.03	0.0061	0.1247	25700	50400	0.2587	0.0067
0.37	0.0586	0.1659	20400	50500	0.3163	0.0437
0.53	0.0789	0.1818	19200	35500	0.3386	0.0581
0.8	0.1089	0.2053	25300	42800	0.3714	0.0791

Table 3.3: Complete predicted stiffness values for the segment C6-C7 in newborns. Compression and tension are given in N/m. Flexion, extension, lateral bending and axial rotation in Nm/deg.

C6-C7						
Age (month)	Flexion	Extension	Compression	Tension	Lateral bending	Axial rotation
0	0.2544	0.4784	21700	44400	0.1087	0.1105
0	0.3456	0.4368	24000	36700	0.1087	0.1105
0	0.1328	0.5696	13600	37100	0.1087	0.1105
0	0.2816	0.2480	22700	39400	0.1087	0.1105
0.03	0.7216	0.3392	36400	45200	0.1136	0.1137
0.37	0.3984	0.3120	30100	50800	0.1610	0.1447
0.53	0.2384	0.3440	39000	61500	0.1793	0.1567
0.8	0.1152	0.4816	38300	34200	0.2063	0.1743

3.2.3 BirthViewH

3.2.3.1 Overview

BirthViewH is a simulation software, which is using a haptic device to provide information on the effort needed to manipulate the fetal skull as well as its hardness and softness (see Figure 3.8). BirthViewH allows adjustments of the mechanical properties at runtime, including the stiffness and damping coefficients of the neck. In addition the software facilitates using multiple haptic devices at the same time making it easier to guide the movements of objects on a scene.

3.2.3.2 Software Engineering

Currently the application has been developed using a code and fix model, but the plan is to restructure the application to allow having multiple neck models and different scenes (see Figure 3.9). Also a switch is required to a more advanced GUI library to provide creation of additional GUI elements such as menus, lists etc.

3.2.3.3 Phantom Omni

Phantom Omni (currently The Geomagic Touch) is a mid-range professional haptic device (see Table 3.4). Used in research, 3D modeling and more, Phantom Omni allows users to freely sculpt 3D clay, enhance scientific or medical simulations, increase productivity with interactive training, and easily maneuver mechanical components to produce higher quality designs (The Touch Haptic Device, 2019).

Phantom Omni is a motorized device that applies force feedback on the user's hand, allowing them to feel virtual objects and producing true-to-life touch sensations as user manipulates on-screen 3D objects (The Touch Haptic Device, 2019).

3.2.3.4 Libraries

BirthViewH is using CHAI3D framework, GLFW and AntTweakBar GUI libraries.

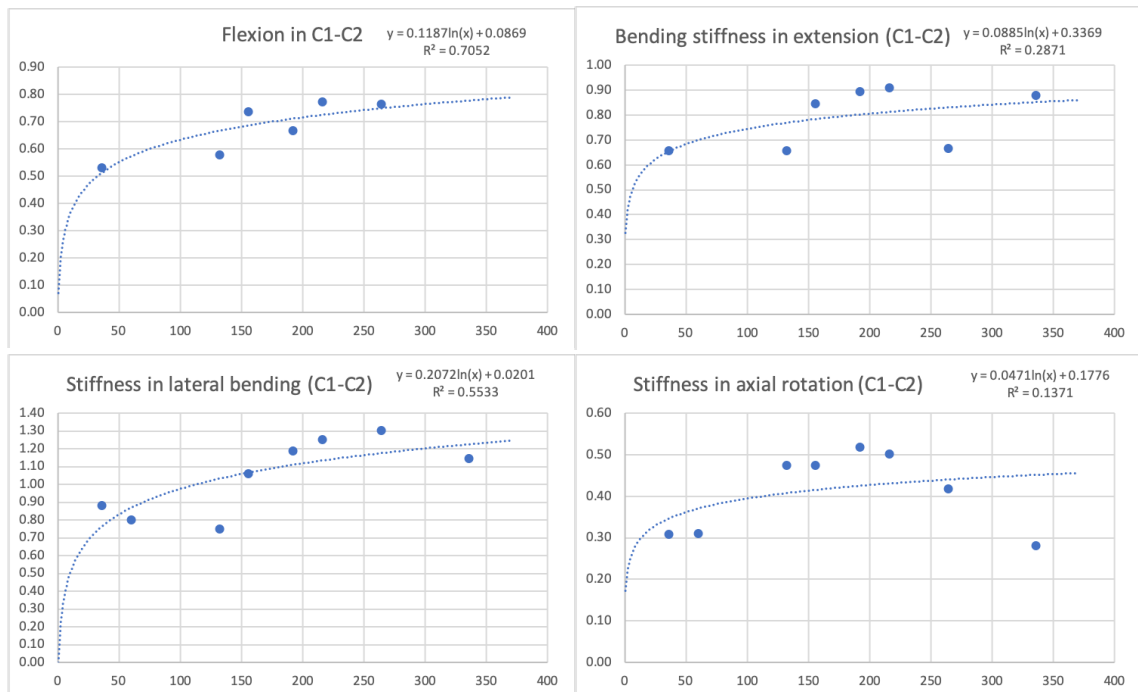


Figure 3.5: Logarithmic regression of C1-C2 for adults in flexion, extension, lateral bending and axial rotation

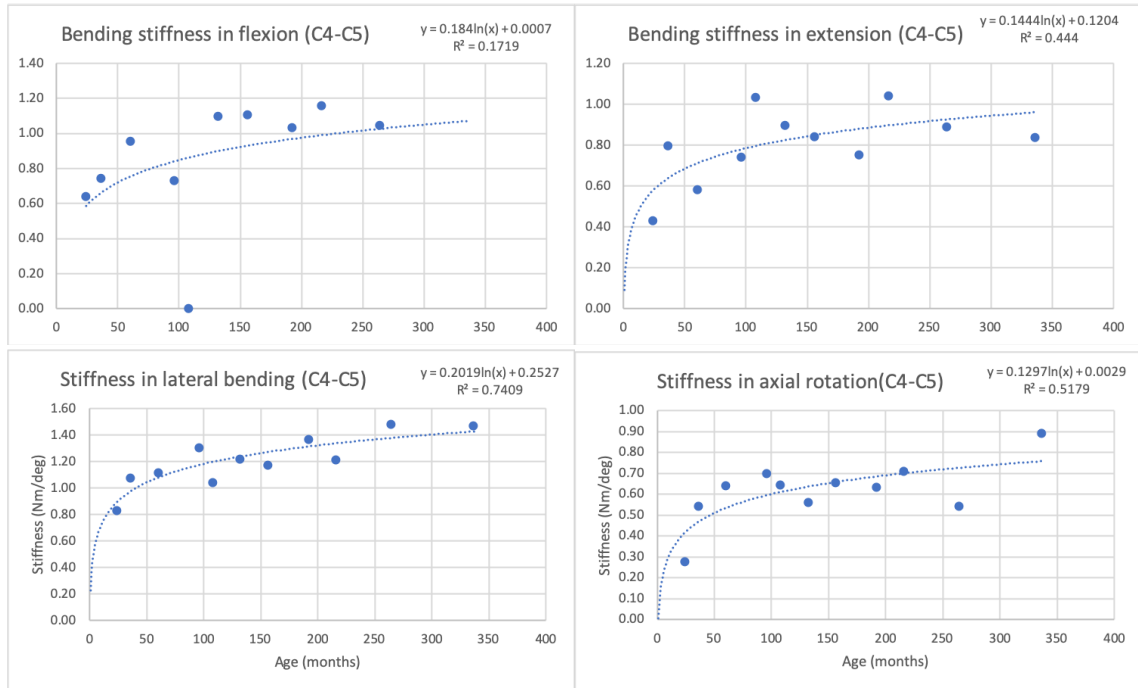


Figure 3.6: Logarithmic regression of C4-C5 for adults in flexion, extension, lateral bending and axial rotation

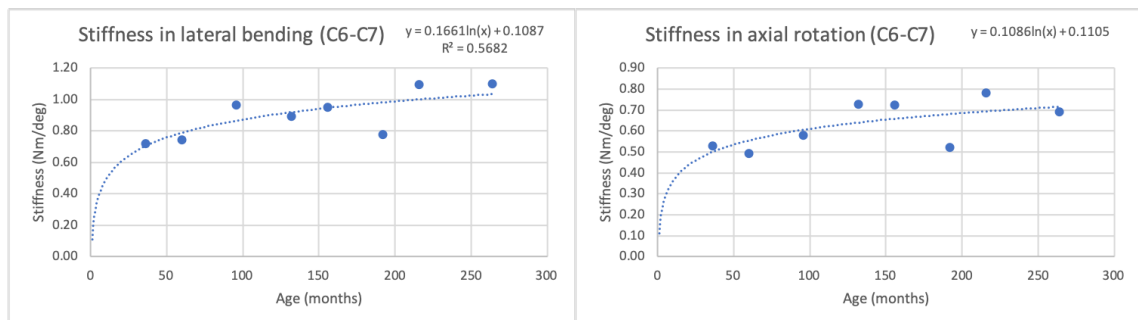


Figure 3.7: Logarithmic regression of C6-C7 for adults in lateral bending and axial rotation

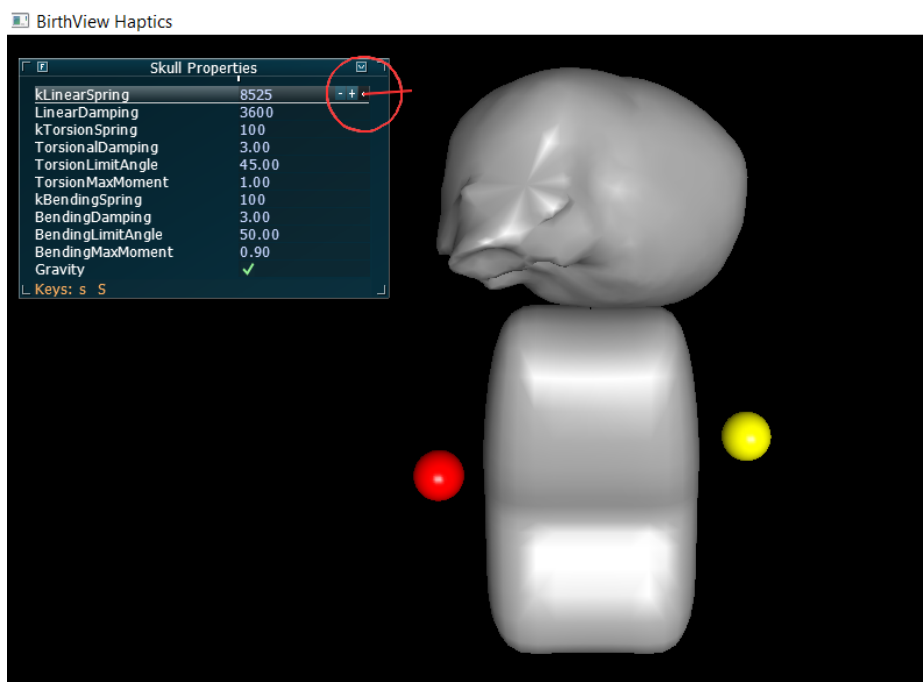


Figure 3.8: BirthViewH

Table 3.4: The Geomagic Touch specification

SPECIFICATIONS	TOUCH
Workspace	~6.4 W x 4.8 H x 2.8 D in > 160 W x 120 H x 70 D mm
Range of motion	Hand movement pivoting at wrist
Nominal position resolution	> 450 dpi ~0.055 mm
Maximum exertable force and torque at nominal position (orthogonal arms)	0.75 lbf/3.3 N
Stiffness	x-axis > 7.3 lb/in (1.26 N/mm) y-axis > 13.4 lb/in (2.31 N/mm) z-axis > 5.9 lb/in (1.02 N/mm)
Force feedback (3 Degrees of Freedom)	x, y, z
Position sensing/input (6 Degrees of Freedom)	x, y, z (digital encoders) [Roll, pitch, yaw ($\pm 5\%$ linearity potentiometers)]
Interface	USB 2.0

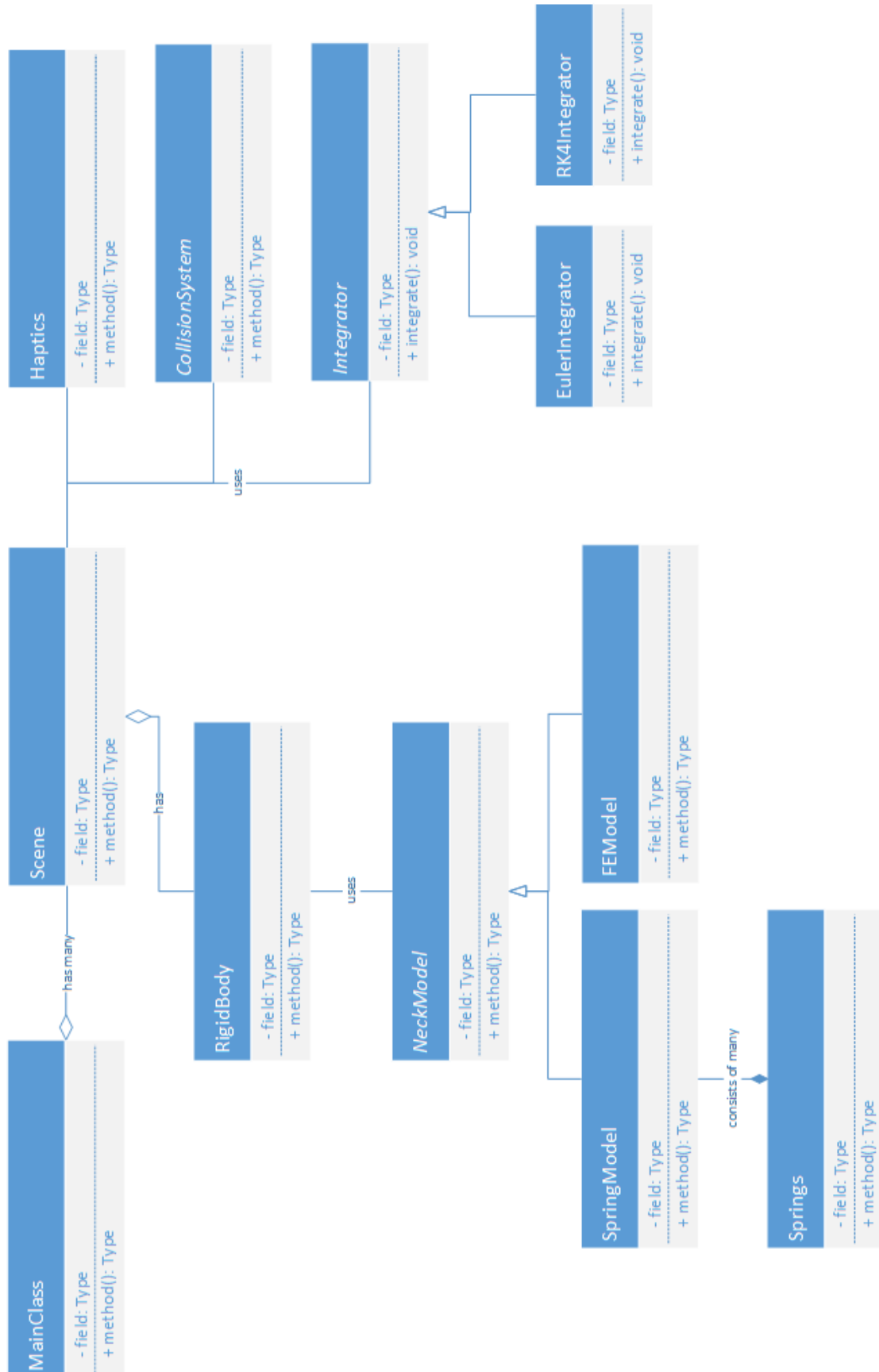


Figure 3.9: BirthViewH class diagram.

CHAI3D is an open source cross-platform C++ simulation framework for computer haptics, visualization and interactive real-time simulation. CHAI3D supports a variety of commercially available haptic devices and makes it simple to support new custom force feedback devices.

GLFW is an open source, cross-platform library for OpenGL, which provides a simple API for creating windows, contexts and surfaces, receiving input and events.

AntTweakBar is a C/C++ library that allows programmers to add a graphical user interface into graphics applications based on OpenGL.

3.2.3.5 Physics

3.2.3.5.1 Physics simulation

Here we are going to describe the motion of objects in BirthViewH. Every rigid body in the software can translate across the scene and perform rotations.

The process of finding out the object's translation can be described as follows:

- Calculate the forces acting on the object
- Sum up the forces in order to find a single net force
- Use Newton's second law to calculate the object's acceleration due to the applied forces:

$$F = ma \tag{3.5}$$

where m is the object's *mass* and a is its *acceleration*.

- Integrate the object's acceleration to find its velocity
- Integrate the object's velocity to calculate its position

Similarly for simulating the object's rotation:

- Calculate the torque acting on the object
- Add up the torques to find a single resultant torque

- Use Newton's second law for rotation to calculate the object's angular acceleration:

$$\tau = I\alpha \quad (3.6)$$

where I is the object's *moment of inertia* and α is its *angular acceleration*.

- Integrate the object's acceleration to find its angular velocity
- Integrate the object's velocity to calculate its rotation

3.2.3.5.2 Haptic interaction

CHAI3D provides a class called **cGenericHapticDevice** that implements a set of methods to communicate with most common 3D haptic devices. For the model of the haptic device that has been tested with BirthViewH, namely Phantom Omni, it implements a class called **cPhantomDevice**.

The force from a haptic device can be acquired by calling a method `getForce()`. It is then added to the resultant force and is used to calculate the torque caused by the device. Equation 3.7 shows the relationship between force, torque and moment arm, which is the distance from the pivot point to the point where the force is applied. Torque is defined as a cross product between the moment arm and the force vector.

$$\tau = r \times F \quad (3.7)$$

where r is *moment arm* and F is *force*.

3.2.3.6 Integration

3.2.3.6.1 Numerical integration

Numerical integration is an approximate computation of an integral using numerical techniques. BirthViewH is using a semi-implicit Euler integrator¹ in order

¹Since the discovered stiffness values for a fetal cervical spine are represented by small numbers (Luck et al., 2008; Luck, 2012; Coats and Margulies, 2008; Ouyang et al., 2005; Nuckley et al., 2013a), semi-implicit Euler integration is considered to be sufficient.

to integrate the object's accelerations and velocities. The following pseudocode describes the process:

```
while (true)  
{  
    acceleration = acceleration + force/mass  
    velocity = velocity + acceleration * timestep  
    position = position + velocity * timestep  
}
```

3.2.3.7 Clinical study

The following content is based on a published article “A haptic user interface to assess the mobility of the newborn’s neck” (Sadulaev et al., 2017).

The improved neck model, used in the childbirth simulator (BirthView), is approximated as a number of Hookean springs, which have stiffness coefficients indicating resistance of a head to translation and rotation.

The neck model in the childbirth simulator uses biomechanical properties described in the handful of studies on postmortem human subjects (PMHS) of children, adults and animals (Nuckley et al., 2013a; Luck, 2012; Luck et al., 2008; Ouyang et al., 2005). Nonetheless, these studies for newborns are limited mostly to the sagittal plane of motion. Therefore, the remaining values can only be derived by proportionally decreasing the studied values of adult PMHS. Even so not a single study among the listed provide sufficient information on all three planes of motion: flexion/extension, lateral bending and side rotation.

The developed BirthViewH software is intended to fill that void in the above-mentioned studies and to improve accuracy of simulating a computer-based neck model.

3.2.3.8 Geometric models

A newborn’s head model is an amended model from the childbirth simulator, which in turn has been obtained from a study on fetal head moulding (see Figure 3.10).

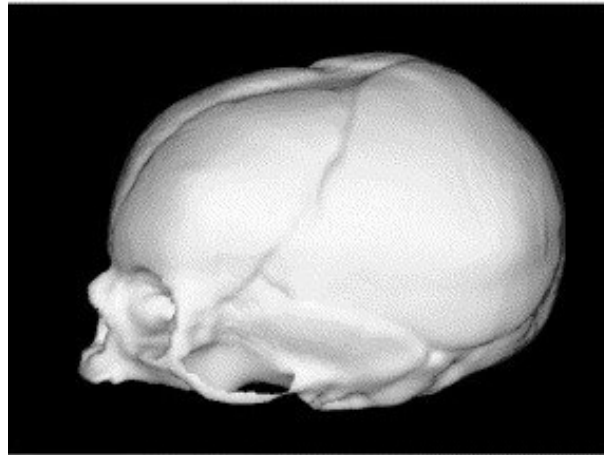


Figure 3.10: An initial version of the fetal head/skull model from a study on fetal head moulding (Lapeer and Prager, 2001). The model comprises approx. 64K triangular polygons.

A center of rotation, i.e. pivotal point of the head is at foramen magnum.

3.2.3.9 Neck model

The employed neck model is graphically depicted as a red line segment and is developed as a collection of spring-damper systems. The model is utilizing the available stiffness parameters presented in the research papers by (Luck et al., 2008; Luck, 2012). There are two types of Hookean springs utilized in order to simulate resistance of a newborn's head on stretch/compression, bending and rotation: linear spring, bending and torsional spring.

3.2.3.10 Neck mechanical properties

Masses of the fetal skull, trunk and neck are also in accordance with the data provided in these papers. Hence, the length of the neck is 3.61 cm and the masses of a trunk and head are 2.085 kg and 0.665 kg respectively. The linear damping is equal to 9650 Ns/m and 3650 Ns/m for the head and trunk respectively and the rotational damping is 3 Ns/degree for both the head and trunk. The stiffness values for the tensile and bending springs are directly incorporated from Luck's data, specifically subject 07P, aged 0 months. The tensile stiffness coefficient is

equal to 7900 N/m under load displacement of 0.69mm (musculature was not considered at the moment). The flexion bending stiffness is the sum of stiffness values of three cervical segments (O-C2, C4-C5 and C6-C7) and is equal to 0.0245 Nm/degree. The extension bending stiffness is calculated to be 0.1271 Nm/degree. In addition, to avoid extreme bending, the stiffness values will increase 1000 times

3.2.3.11 Experiments and Results

The developed software has been used in the experiment aimed to assess the strength and flexibility of the newborn's neck. The experiment has been conducted in the University Hospital in Norwich (NNUH), United Kingdom. 10 midwives and a pediatrician have agreed to participate in the assessment and been given short training prior to the experiment to get them used to using the haptic devices. The description of the procedure and instructions are given in Appendix C.

The professionals were required to apply certain force to the newborn's head on the screen using two haptic devices and to validate the resistance of the skull, during bending and rotation, against their real-life experience. The initial properties were then adjusted according to their feedback (see Figure 3.11).

As a result the ultimate torsional resistance (stiffness) varies between 4 and 12 Nm/degree and the range of motion ranged between 57.45 and 75.06 degrees from the initial upright position. Ultimate bending stiffness ranges between 12 and 18 Nm/degree and ROM for flexion was 50 degrees whereas for extension it ranged from 36.5 to 50 degrees. It is important to mention that flexion and extension were grouped together, even though in real life resistance of flexion would be noticeably lesser than of extension. Also lateral bending resistance and ROM has not been studied in the experiment.



Figure 3.11: Two haptic devices (Phantom Omni) are being used in order to validate the resistance of the fetal skull during bending and rotation. The yellow sphere on the screen corresponds to the right hand, whereas the red sphere corresponds to the left hand. The description of the procedure and instructions for midwives are given in Appendix C.

Position	RD	kT	cT	Side Rotation	kB	cB	Flexion	Extension	Comments
consultant	2	12	3	70	12	3	50	50	
obstetrician	2	12		70	12		50	50	
midwife	2	7		74.03	13		50	-	extension would be stiffer
doctor	3			-	-		-	-	looser flexion, stiffer extension
obstetrician	3	4		57.45	19		50	36.5	extension is between 36.5 and 40 degrees
unknown	2/1.5	15		66.22	-		50	40	
pediatrician	-	27		66.45	-		-	-	
doctor	3	4		70.43	-		-	-	
unknown	2			-	-		-	-	
doctor	3	8		75.06	18		50	-	
RD – rotational damping of a newborn’s head (Ns/degree), kT – torsion coefficient (Nm/degree), T – torsional damping coefficient (Nms/degree), kB – bending coefficient (Nm/degree), B – bending damping coefficient (Nms/degree), Lateral rotation, flexion and extension correspond to ROM (degrees)									

3.2.3.12 Discussion

The stiffness values for flexion and extension are much higher than the reported stiffness values in the study by Luck (2012). It was expected for them to be considerably higher since soft tissue structures can increase stiffness up to two times. However, the calculated stiffness values are 100 and 1000 bigger for flexion and extension respectively. This is possibly due to the fact that during the experiment only the maximum stiffness was identified at the maximum angle whereas the reported values are linear approximations of an average non-linear stiffness for non-destructive bending tests.

The acquired results for ROM compare well with Öhman and Beckung (2008) and studies by Luck (2012). Although at first glance the minimum obtained rotation ROM ranges from 57.45 degrees seems to be larger than the reported 52.6 degrees it is important to note that the heads of the infants in the mentioned study were not rotated even near to their failure angle so as not to harm them. However, in the virtual environment one can freely manipulate the newborn's head to the maximum possible degree without being afraid to cause damage and consequently adjust it according to what they believe to be its peak angle.

3.2.3.13 Conclusion and Future Work

From the presented results it appears that virtual simulation software is capable of replicating biomechanical properties of a newborn's head motion within an acceptable margin of error, with the help from obstetrics, midwives and paediatricians.

A number of assumptions have been made in this experiment: a baby was considered to be held upright by a second person. In addition the force of gravity has been omitted for the sake of simplicity of manipulating the head.

3.2.4 Mechanical models of the fetal neck

3.2.4.1 Bushing element using six degrees-of-freedom spring-damper system

3.2.4.1.1 Overview

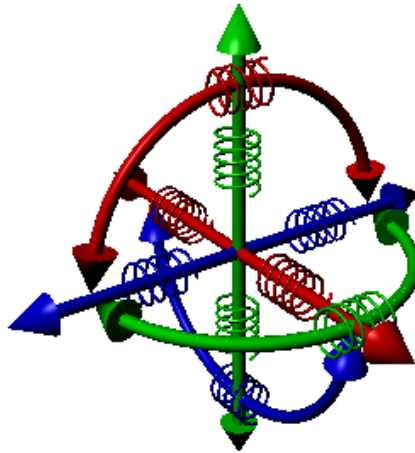


Figure 3.12: Bushing element comprising six degrees-of-freedom springs (Autodesk Maya, 2019). The straight green, red and blue arrows correspond to translations along y-axis, x-axis and z-axis respectively. The curved arrows correspond to rotations around the axes. The linear and torsional springs are used to resist motion along and around each axis

Bushing elements are widely used in order to simulate intervertebral disc's behaviour (Bondy et al., 2014; Huynh et al., 2012; Esat and Acar, 2007; Van Lopik and Acar, 2007; Senteler et al., 2015). Bushing elements restrict both translation and rotation of two rigid bodies along x, y and z axis by applying restricting forces and torques respectively.

The implemented bushing element uses four spring-damper systems, i.e. one translational and three rotational ones (see Figure 3.12).

For the translational forces to be calculated it is necessary to specify translational stiffness and initial (resting) length between the rigid bodies. Hence, when

the first rigid body translates relative to the second rigid body in any direction, the force restricting that motion, i.e. keeping them connected to one another, is calculated according to the translational form of Hooke's law (see Equation 3.19).

Similarly, three rotational stiffnesses and maximum angles for each axis are used to calculate torques, exerted by rotational springs around each axis (x, y and z). These rotational springs only start resisting motion when the angle between rigid bodies is greater than the specified maximum angle below which the spring remains inactive. The torque is calculated according to the angular form of Hooke's law (see Equation 3.8).

3.2.4.1.2 Tensile/compressive spring

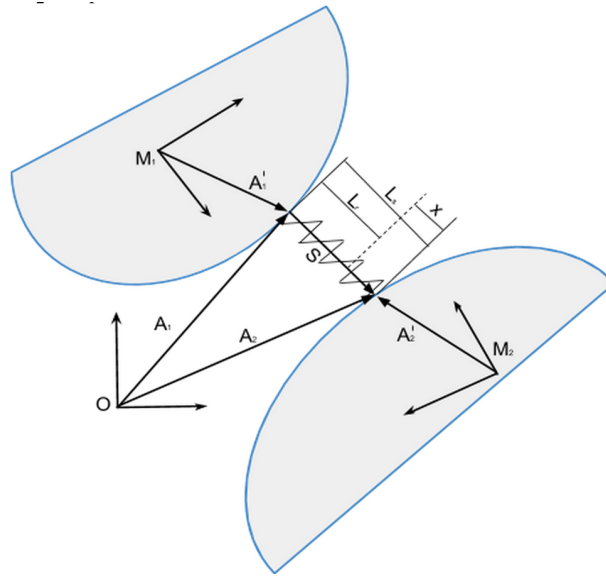


Figure 3.13: The detailed representation of a single tensile/compressive spring attachment in the bushing element.

Figure 3.13 shows how the displacements of springs are calculated in the simulation software when objects are connected with either a tensile or a compressive spring. Two objects are connected by a tensile/compressive spring with a resting length of L_r at the attachment points \vec{A}_1' and \vec{A}_2' . The current length of the spring is denoted by L_s . The attachment points \vec{A}_1' and \vec{A}_2' of the spring are defined in the local coordinates of the objects they are connected to. The world coordinates

\vec{A}_1 and \vec{A}_2 are calculated by transforming the local attachment coordinates by the transformation matrices of the corresponding objects. The current length L_s is calculated as the difference of the world vectors: $\vec{A}_2 - \vec{A}_1$. Finally, the spring displacement x is calculated as the difference of the current and resting lengths: $L_s - L_r$.

3.2.4.1.3 Torsional spring

Implemented torsion springs to approximate the overall resistance of the vertebral column to side rotations. The torque exerted by the torsion springs onto the bodies are calculated according to the angular form of Hooke's law:

$$\tau = -k\theta \quad (3.8)$$

where τ - torque, k - torsion coefficient, θ - angle of twist from an object's equilibrium position

3.2.4.1.4 Restricting rotational motion around a specific axis

By allowing only one rotational degree of freedom, where the other rotational degrees of freedom are locked, it makes it easy to calculate the angle between two rigid bodies. Figure 3.14 and 3.15 shows how the angle is calculated for a lateral bending of a skull, i.e. around Z-axis. \vec{X}'_1 and \vec{X}'_2 are local X unit vectors along X-axis of the head and body respectively. The angle between the local unit vectors of the rigid bodies along X-axis is derived from the algebraic and geometric definitions of the dot product.

Algebraic definition of the dot product:

$$a \cdot b = \sum_{i=1}^n a_i b_i = a_1 b_1 + a_2 b_2 + \dots + a_n b_n \quad (3.9)$$

where \sum denotes summation and n is the dimension of the vector space.

Geometric definition of the dot product:

$$a \cdot b = |a||b| \cos \theta \quad (3.10)$$

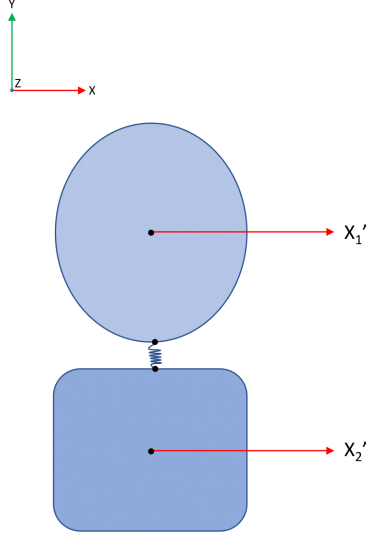


Figure 3.14: Head in normal position (front view). Rotation is around Z-axis.

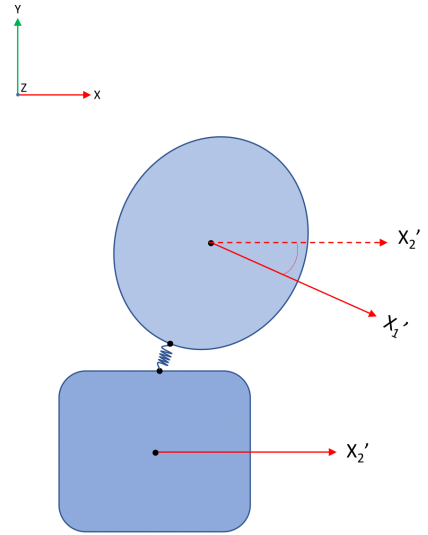


Figure 3.15: Head is flexed laterally (front view). Rotation is around Z-axis.

where θ is the angle between a and b , and $|a|$ and $|b|$ are their lengths.

From Equation 3.10 we find that:

$$\cos \theta = \frac{a \cdot b}{|a||b|} \quad (3.11)$$

$$\theta = \arccos \frac{a \cdot b}{|a||b|} \quad (3.12)$$

Finally by substituting the numerator in the last equation with the algebraic definition of the dot product we arrive at the solution for finding the angle between two vectors:

$$\theta = \arccos \frac{a_1b_1 + a_2b_2 + \dots + a_nb_n}{|a||b|} \quad (3.13)$$

In case of all three rotational degrees of freedom available, it is possible that the object is rotated around the Y-axis, prior to the rotation around the Z-axis. Figure 3.16 and 3.17 shows the top and front views of a head and torso. Again \vec{X}'_1 and \vec{X}'_2 are unit vectors along the local X-axis and \vec{Z}'_1 and \vec{Z}'_2 are unit vectors

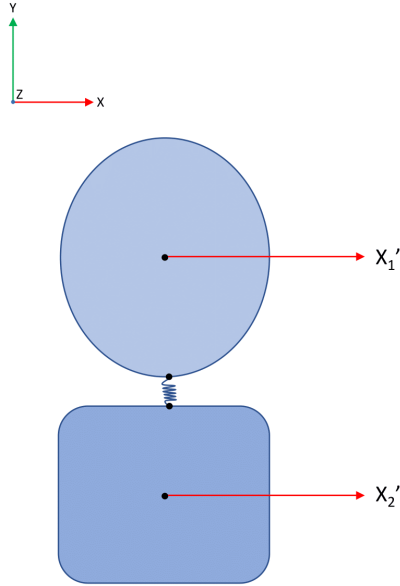


Figure 3.16: Head in normal position (front view). Rotation is around the Z-axis.

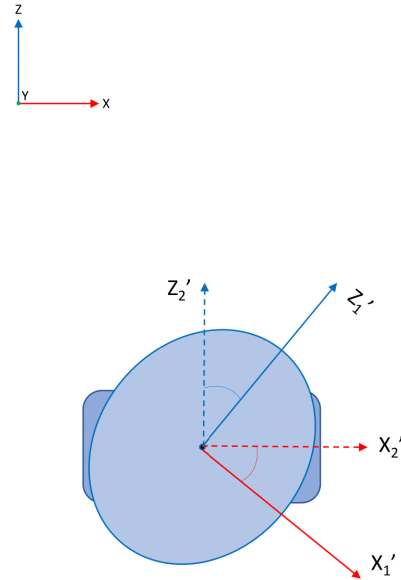


Figure 3.17: Head is rotated (top view). Rotation is around Y-axis.

along the local Z-axis of the head and body respectively. In Figure 3.17 the head is rotated by 45 degrees and, although, there is no side bending shown in Figure 3.16, the 45 degrees angle of the rotation will be used to calculate torques between the head and torso both in axial and coronal planes (rotation and side bending). An additional step is required in order to isolate side bending from a rotation.

In this particular case, by projecting the head's local \vec{X}_1 vector to torso's local \vec{X}_2 vector, prior to calculating the angle between these vectors, angles around other axes no longer contribute to the calculation of the torque in side bending. The projection is calculated with a dot product.

Although, the projection successfully isolates motion around a particular axis, there is a possibility of a Gimbal lock¹ (Hoag, 1963), when the head is rotated at 90 degrees with a torso at 0 degrees, one of the degrees of freedom is lost and projection results in zero. The problem can be addressed by using quaternions

¹Gimbal lock is the loss of one degree of freedom in a three-gimbal mechanism caused by the alignment of two of the three gimbals together, "locking" the system into rotation in a two-dimensional space.

(Diebel, 2006), however, they are not required at this stage to achieve the aim and objectives of the project. This will be further discussed in Section 5.3.

3.2.4.2 Ball and Socket Joint



Figure 3.18: Ball and Socket Joint

Ball and Socket joints only allow rotations between two bodies with no translations. Therefore, the bodies cannot move with respect to one another (Chappuis, 2013).

The joint was implemented in *BirthEngine* as a *Component*. The joint is implemented by calculating both angular and linear impulses required to limit the translation of the connected bodies. The algorithm is described as follows:

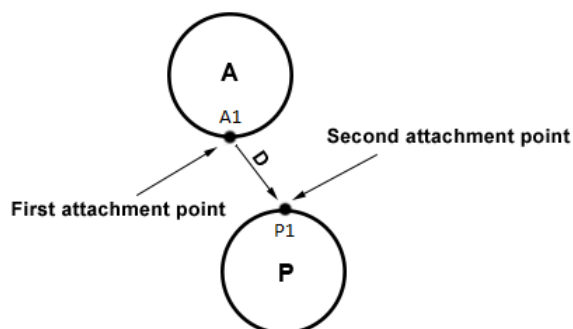


Figure 3.19: Displacement vector from $A1$ to $P1$

- Calculate a displacement vector \vec{D} from $A1$ to $P1$ (see Figure 3.16).

$$\vec{D} = \vec{P1} - \vec{A1} \quad (3.14)$$

- Take the first derivative of the displacement vector and acquire the required velocity:

$$\vec{V} = \dot{\vec{D}} = \lim_{t \rightarrow 0} \frac{\vec{P1} - \vec{A1}}{t} \quad (3.15)$$

where t is *time* and the overhead dot denotes differentiation with respect to *time*.

- Calculate linear impulse based on the calculated velocity and the mass m of the object A :

$$\vec{P} = m\vec{V} \quad (3.16)$$

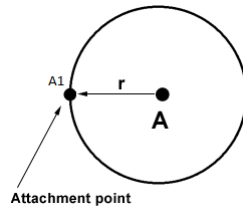


Figure 3.20: Object's distance from the attachment point

- Calculate angular momentum based on the linear impulse P and r , which is the position of the object A relative to the attachment point $A1$ (see Figure 3.20):

$$\vec{L} = \vec{r} \times \vec{P} = (\vec{A1} - \vec{A}) \times \vec{P} \quad (3.17)$$

- Apply the angular momentum to the attachment point A
- Recalculate the displacement vector (see Figure 3.21).
- Recalculate the velocity
- Recalculate the linear impulse
- Apply the linear impulse to the attachment point $A1$

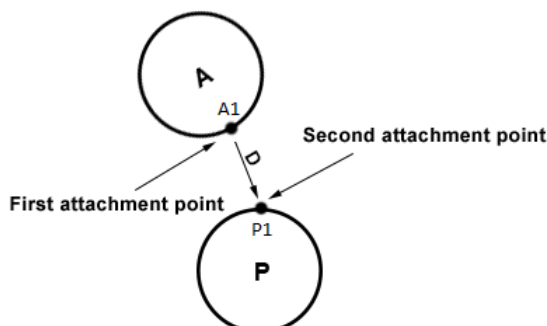


Figure 3.21: Displacement vector from rotated point $A1$ to point $P1$

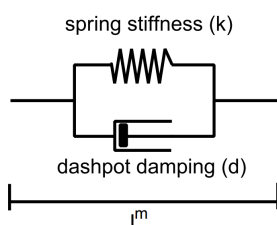


Figure 3.22: Mass-Spring-Damper system.

3.2.4.3 Spring-Damper system

The system consists of a spring and a damper (Figure 3.22). There are three forces involved in this system, namely the applied force and two reaction forces. The spring reaction force reacts when the object is displaced from its equilibrium, while the damper reaction force acts only when the object is in motion. Equation 3.18 is used to calculate the force acting on the object.

$$F = -kx - cv \quad (3.18)$$

where c - *damping coefficient*, v - *object velocity*

3.2.5 Validation of the fetal neck range of motion

3.2.5.1 Overview

The range of motion of the existing neck model in the BirthView software required validation to establish the necessity of an improved neck model. The range of motion of the neck has been measured and validated in a video player for sports

Table 3.5: Mechanical properties of NM01

Cervical vertebrae	3 linear springs	
	stiffness, N/m	damping, N s/m
C1	330	10
C2		
C3		
C4		
C5		
C6		
C7		

analysis Kinovea, using goniometer tools.

3.2.5.2 Goniometry

The term goniometry is derived from two Greek words: *gonia*, meaning "angle," and *metron*, meaning "measure." Goniometry refers to the measurement of angles created at human joints by the bones of the body. These measurements are obtained by placing the parts of the measuring instrument, called a goniometer (see Figure 3.23), along the bones immediately proximal and distal to the joint being evaluated. Norkin and White (2016).

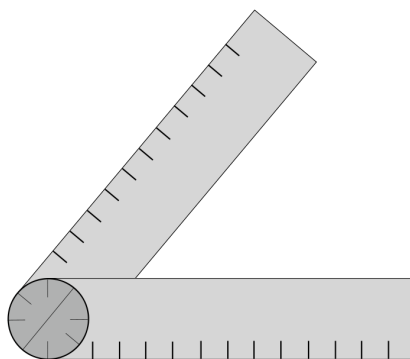


Figure 3.23: Goniometer. The fixed arm is referred to as a proximal arm, whereas the non-fixed one is called a distal arm. The base of the goniometer is called fulcrum.

It is essential to stabilize the shoulder girdle to prevent motion of the thoracic and lumbar spine while measuring ROM for the cervical spine.

3.2.5.2.1 Measuring flexion

Flexion occurs in the sagittal plane around a coronal axis.

Goniometer alignment (Norkin and White, 2016):

- Center the fulcrum of the goniometer over the external auditory meatus.
- Align the proximal arm so that it is either perpendicular or parallel to the ground.
- Align the distal arm with the base of the nostrils.



Figure 3.24: In the starting position for measuring cervical flexion, the examiner aligns the proximal goniometer arm so that it is perpendicular to the floor. The goniometer body is centered over the subject's external auditory meatus. The examiner aligns the distal arm with the base of the nostrils (Norkin and White, 2016).



Figure 3.25: At the end of the ROM, the examiner's left hand aligns the proximal goniometer arm. The examiner uses her right hand to maintain alignment of the distal arm with the base of the nostrils (Norkin and White, 2016).

3.2.5.2.2 Measuring extension

The position, stabilization and alignment are the same as for measuring cervical flexion.

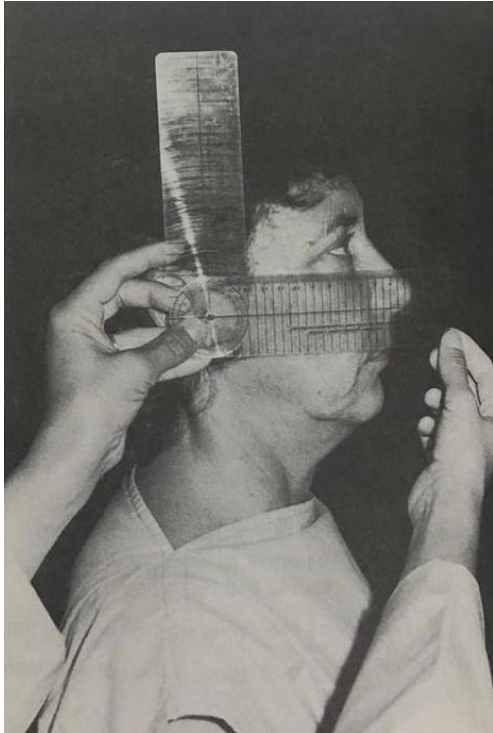


Figure 3.26: In the starting position for measuring cervical extension, goniometer alignment is the same as for measuring cervical flexion (Norkin and White, 2016).



Figure 3.27: At the end of cervical extension, the examiner maintains the perpendicular alignment of the proximal goniometer arm with her left hand. The examiner's right hand aligns the distal arm with the base of the nostrils (Norkin and White, 2016).

3.2.5.2.3 Measuring side rotation

Goniometer alignment (Norkin and White, 2016):

- Center the fulcrum of the goniometer over the center of the head.
- Align the proximal arm parallel to an imaginary line between the shoulders.
- Align the distal arm with the tip of the nose.

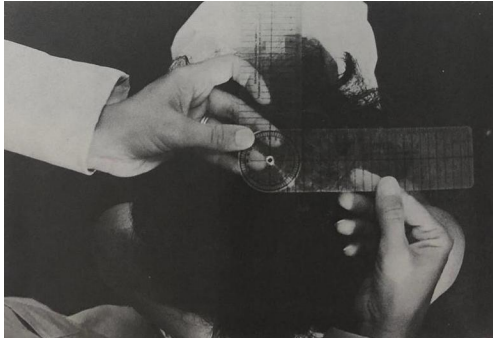


Figure 3.28: Starting position for measuring side rotation.

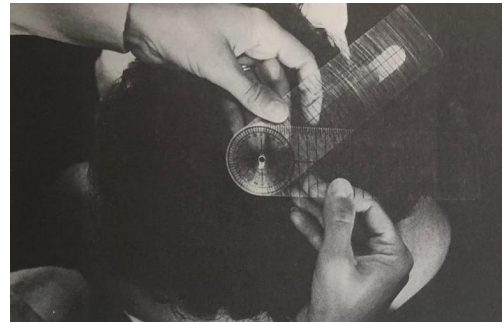


Figure 3.29: Measuring side rotation with a goniometer.

3.2.5.2.4 Measuring side bending

Goniometer alignment (Norkin and White, 2016):

- Center the fulcrum of the goniometer over the C-7 vertebra.
- Align the proximal arm with the thoracic vertebrae so that the arm is perpendicular to the ground.
- Align the distal arm with the midline of the head.



Figure 3.30: Measuring ROM for lateral bending.

3.2.5.3 Kinovea

Kinovea provides tools for capture, observation, annotation and measurement of human motion (Kinovea, 2016). In particular, among many other functions, it provides tools for tracking trajectories of points in a video recording, measuring distances and angles between human joints, with subpixel accuracy, using goniometer tools. In addition, it provides grid-based calibration which allows to perform measurements even when the plane of motion is not aligned with the camera.

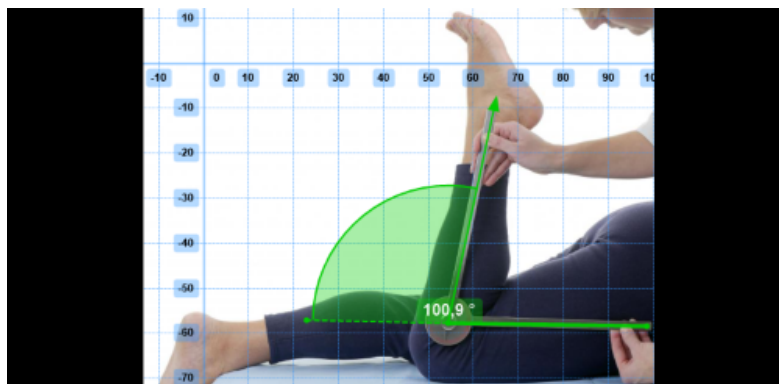


Figure 3.31: Measuring angles in Kinovea (Kinovea, 2016)

3.3 Computational Neck Models

3.3.1 Overview

This section is concerned with the description of the developed computational neck models. It is worth mentioning that all of the neck models can be simulated in real time. Firstly the preliminary neck models are described, which were utilized in the older simulation software BirthEngine (see Appendix E.1). The section then follows with a description of the default basic neck model (NM01) and its validation in the latest childbirth simulation software BirthView (see Appendix E.2).

NM01 can only resist motion of the head when rotated and, therefore, has been extended to introduce resistance to motion in other directions. Thus, NM02 complements NM01 by adding resistance in flexion and extension, however, the stiffness values can not be set individually for either flexion or extension. NM03 and NM04 are using a 6DOF bushing element, which can restrict motion along all axes.

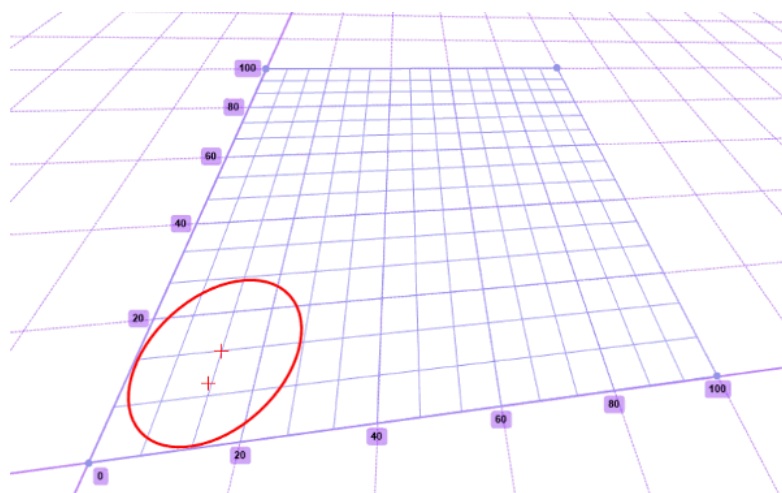


Figure 3.32: Perspective measurements in Kinovea (Kinovea, 2016)

3.3.2 Preliminary experiments in BirthEngine .

3.3.2.1 Spring-Damper model with Ball and Socket Joint (NM00A).

3.3.2.1.1 Overview

The model consists of seven vertebrae interconnected with three ligaments ¹ (see Figures 3.33 and 3.34). The latter is simulated with three simple springs obeying Hooke's Law. In addition, the motion of a vertebra is restricted by the ball and socket joint constraint implemented using the heuristic Ball and Socket Joint Resolver (ball and socket joint is not visible in Figures 3.33 and 3.34). To put it simply, the only allowed movement for each vertebra is a rotation, so that every vertebra can only rotate around a certain fixed point with the springs limiting that rotation.

3.3.2.1.2 Validation in BirthEngine (see Appendix E.1)

A number of experiments were conducted with the integrated dynamic neck model (NM00A). Mass of both the fetal skull and trunk were set to 1 kg and the linear

¹The model was developed in BirthEngine (written in C#) simulation software, which is a generic medical simulation engine. The screenshot is given in Appendix E.1.

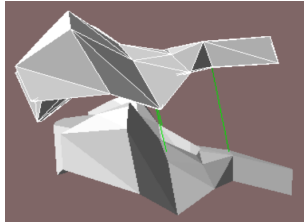


Figure 3.33: Flexion of the top vertebra. In this figure two cervical vertebrae are connected by the ball and socket joint. In addition, the motion of each vertebra is restricted by three compression/elongation springs simulating ligamentum flavum and supraspinous ligament (see Figure F.12).

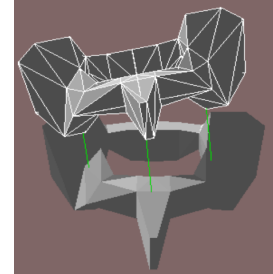


Figure 3.34: Lateral bending of the top vertebra. In this figure two cervical vertebrae are connected by the ball and socket joint. In addition, the motion of each vertebra is restricted by three compression/elongation springs simulating ligamentum flavum and supraspinous ligament (see Figure F.12)

and rotational damping were set to 12 Ns/m and 12 Ns/degree each. Finally the magnitude of the uterine expulsion force was set to 4 N.

The first experiment showed certain improvements of the childbirth simulation. As such the cardinal movements have become prominent (engagement, descent, flexion and internal rotation) compared to the simulation without the neck model.

Another set of experiments was carried out, but this time there was an ellipsoid fetal trunk connected to the neck model. The experiment resulted in some extension and external rotation (see Figure 3.35).

Table 3.6 summarizes the described experimental results.

3.3.2.2 Improved Spring-Damper model (NM00B).

3.3.2.2.1 Improvements

The following improvements were made to the previous model (NM00A):

1. Introduced tensile and compression-only springs to simulate certain ligaments (see Figures 3.33 and 3.34). The forces exerted by the springs onto

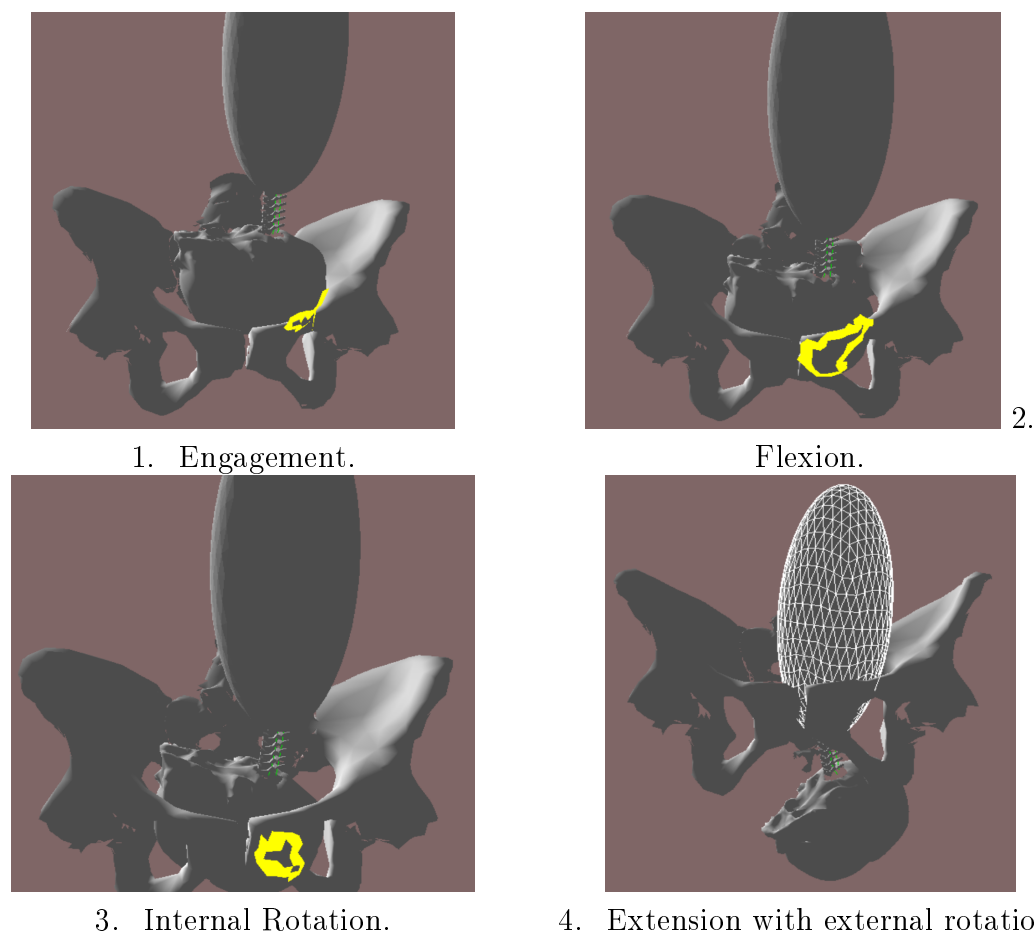


Figure 3.35: Childbirth simulation in BirthEngine software using the neck model “NM00A”. The numbers correspond to the cardinal movements (see Section 1.2.5). The simulation resulted in some extension and external rotation.

the bodies that it is connected to are calculated according to Hooke’s law:

$$F = -kx \quad (3.19)$$

where k – spring stiffness, x – spring displacement

Figure 3.13 shows how the forces are calculated in the simulation software when objects are connected with either a tensile or a compressive spring. Two objects are connected by a tensile spring with a resting length L_r . The current length of the spring is denoted by L_s . The attachment points A'_1 and A'_2 of the spring are defined in the local coordinates of the objects

Table 3.6: Experimental results

Cardinal movement	Neck models		
	No neck	NM00	NM00 with trunk
Descent	+	+	+
Engagement	+	+	+
Flexion	+	+	+
Internal rotation	?	?	?
Extension			+
External rotation			?
Expulsion			

they are connected to. The world coordinates \vec{A}_1 and \vec{A}_2 are calculated by transforming the local attachment points by the transformation matrices of the corresponding objects. The current length S is calculated as the difference of the world vectors: $\vec{A}_2 - \vec{A}_1$. Therefore, spring displacement x is equal to $L_s - L_r$.

2. Torsion springs were implemented to approximate the overall resistance of the vertebral column to side rotations. The torque exerted by the torsion springs onto the bodies are calculated according to the angular form of Hooke's law:

$$\tau = -k\theta \quad (3.20)$$

where τ - torque, k - torsion coefficient, θ - angle of twist from an object's equilibrium position

3. Implemented bending springs to stop the connected objects from sliding along the transverse plane;
4. Introduced constraints to limit the range of movement of each vertebra in the neck;

3.3.2.2.2 Validation in BirthEngine (see Appendix E.1)

The conducted experiments with the improved neck model led to a decrease in the number of observed cardinal movements. Moreover, the simulation became very

unstable in terms of extreme oscillations due to the force caused by accumulated large spring constants. The analysis of instabilities is described in the following subsection.

3.3.2.2.3 Analysis

First of all the instability in behaviour of Hookean springs for large stiffness constants were expected. The main cause of the abnormal oscillations of the rigid bodies connected with springs were allegedly produced by the accumulating errors of the semi-implicit Euler integration. There were a few solutions available to improve the accuracy and stability of the springs: either decreasing the timestep or using a more accurate numerical integration method.

Due to the architecture of BirthEngine software, implementing a more accurate Runge-Kutta integrator was not a trivial task. Therefore, the timestep was decreased from 0.016 to 0.0016 and that indeed stabilized the springs and simultaneously slowed down the simulation. The latter made it possible to identify a problem with collision response in certain areas between the pelvis and a fetal skull. In particular, the outer side of the pelvis mesh model in those areas was slightly damaged and, hence, presumably caused errors in collision response.

The mesh model was smoothed in the Blender software. The repaired pelvic mesh model solved the instability problem even when using the previous timestep using Euler integration. However, the neck model itself has not improved the simulation.

The new complex model consisted of a higher number of various springs and hence required manually adjusting an increased number of stiffness/damping values. The process of calibrating stiffness values for each spring in the model proved to be a time-consuming process. In addition, the fact that the adopted stiffness coefficients had been selected randomly¹, and had not been based on the real data led to a decision to simplify the neck model by removing the cervical vertebrae and connecting the fetal skull directly to its trunk.

¹The coefficients were selected randomly due to lack of data for mechanical properties of the fetal cervical spine's intervertebral discs and ligaments

3.3.3 Basic Neck model (NM01)

3.3.3.1 Overview

Due to the complexity of cervical vertebrae and lack of accurate data on the mechanical properties of the fetal neck, which are necessary to adjust the stiffness and damping values of the springs, it was decided to further simplify the neck model and simulate the whole neck by using one spring only. The newly developed model combines within itself a compression/tension spring and a torsional spring and, therefore, it resists *compression*, *elongation* and *side rotations* (see Table 3.7).

Table 3.7: Mechanical properties of NM01 and NM02 (see 3.3.5)

Neck Models	Neck properties					
	Linear spring		Torsional spring		Bending spring	
	compression	stretch	k, N/m	active angle	k, N/m	active angle
	k, N/m	k, N/m				
NM01	9000	10000	100	45	n/a	n/a
NM02	9000	9000	100	45	100	45

3.3.3.2 Implementation

It has already been discussed above (see equation 3.19) how the forces are calculated in the simulation software when objects are connected with either a tensile or a compressive spring. The following code shows how the torques are calculated for the two objects connected with a torsional spring.

```

// an auxiliary vector to calculate the angle
glm::vec3 x { 1.0f, 0.0f, 0.0f };
// transform the vector above by the rotational matrix only
glm::vec3 one = Math::transformNormal(x, m_startXform);
glm::vec3 two = Math::transformNormal(x, m_endXform);
// calculate an angle between the vectors
float angle = Math::angleBetween(one, two);
float limit = glm::radians(m_torsionLimitDeg);

```

```

// only apply the torque if the angle is bigger than
// a specified angle (45 degrees have been selected
// in our case as bigger values led to extreme rotations)
// The reason behind specifying such an angle is to avoid
// constant resistance of the fetal neck during rotation

if(std::abs(angle) > limit)
{
// calculate the axis around which we need to rotate
// an object
auto axis = glm::normalize(glm::cross(one, two));
// calculating an effective angle between the vectors
auto croppedAngle = (glm::abs(angle) - limit);
// m_kTorsion is the stiffness coefficient
auto torque = croppedAngle * m_kTorsion * axis;
// projecting torque onto the original local direction
// (transverse plane) so as to avoid applying torque
// on bending
torque = m_originalDirectionLocal *
glm::dot(m_originalDirectionLocal, torque);
}

```

3.3.3.3 Experiments and results (see Appendix E.2)

The developed model was used in the latest birthing simulation software and the experiments resulted in observation of all the cardinal movements described in section 1.1, apart from expulsion. The latter may require flexible fetal shoulders (Dietze, 2001).

The length of the neck was set to 1.2 cm and the masses of a trunk and head are 2.5 kg and 1.5 kg respectively. The linear damping is equal to 9650 Ns/m and 3650 Ns/m for the fetal skull and torso respectively and the rotational damping is 3 Ns/degree for both the skull and torso. Finally the periodically changing uterine expulsion force interpolates between 30 and 150 N (Moreau et al., 2008).

Table 3.8 depicts the results of the experiments with NM01 and one can clearly

see an increase in the number of cardinal movements if compared to table 3.6, which represents the results of the experiments with NM00 (see Section 3.3.2.2). However, it should be noted that NM01 was validated in BirthView (see section E.2), whereas NM00 was validated in BirthEngine (see section E.1), which differ in terms of utilized mesh models, collision detection and response techniques. Nevertheless the main difference between the mentioned simulation software is that BirthView is comprised of additional explicit FE cervix and pelvic muscle models. Therefore, it is not necessarily the case that NM01 is more biofidelic or accurate than NM00B, but rather a combination of both biomechanical properties of NM01, FE cervix and pelvic models and updated collision response techniques led to the aforementioned improvements.

Table 3.8: Experimental results with NM01 and NM02 (see 3.3.5)

Cardinal movement	Neck models		
	No neck	NM01	NM02
Descent	+	+	+
Engagement	+	+	+
Flexion	+	+	+
Internal rotation	+	+	+
Extension		+	+
External rotation		+	+
Expulsion			

3.3.4 Validation of the basic neck model in BirthView

3.3.4.1 Introduction

The default neck model in BirthView (see Figure 3.36) is a basic spring-damper model and consists of a combined linear ($k=10000$) and torsional spring ($k=100$) which resists rotation, when the fetal head turns by 45 degrees ¹ either side. Although the neck seems to be sufficient for the successful simulation of cardinal movements in BirthView (Lapeer et al., 2019; Gerikhanov, 2017), it needed to be validated extensively in order to compare the future neck models. The biggest

¹45 degrees is the current default value.

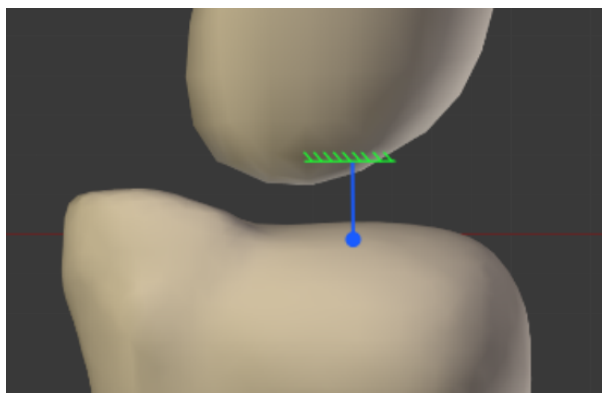


Figure 3.36: Basic Neck in BirthView.

concern about the neck model was its possible incorrect motion of the head while undergoing forward and lateral flexion. The following experiment demonstrates the level of accuracy of the basic neck model in BirthView.

3.3.4.2 Head trajectory and ROM in extension

A video of a newborn was used in order to acquire the trajectory of the head during extension. It can be observed in the video that the head extends until its occiput comes into contact with the back¹. The same seems to be true for flexion, i.e. head flexes until the baby's chin touches the chest.

The ROM was measured here in accordance with goniometrical methods for measuring head motion (see Figure 3.27) and was found to range between 72 and 76 degrees in this particular case. The measurement is depicted in Figure 3.37. This measurement corresponds to the data by Luck (2012).

The basic neck model in BirthView does not have bending springs and, hence, the head's motion in flexion is only restricted by contact between its occiput and the back and a tensile spring. However, since the neck is comprised of one spring only with high stiffness, the head's bending in extension and flexion occurs mainly as a rotation around one point, which is the origin of the head (see Figure 3.38).

¹Video: newborn_n_16 in the collection "PediNeurologic Exam: A Neurodevelopmental Approach" (https://library.med.utah.edu/pedineurologicexam/html/home_exam.html). Published by Paul D. Larsen, M.D., University of Nebraska Medical Center and Suzanne S. Stensaas, Ph.D., University of Utah School of Medicine

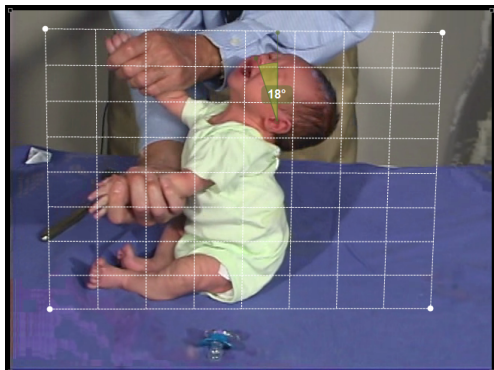


Figure 3.37: Measuring extension from NIPE video in Kinovea.

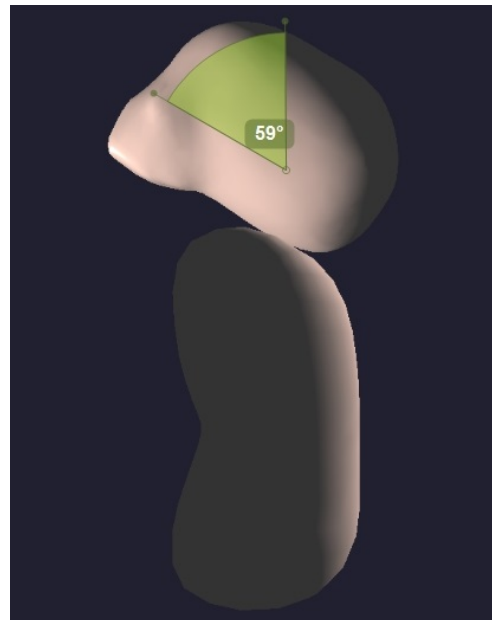


Figure 3.38: Measuring extension in BirthView

In Figure 3.39 it can be seen how the trajectory is measured in Kinovea. The marker was set near the auditory meatus, and the head of the baby followed a relatively long curve. It can also be observed that the change in the position of the head and its rotation occur simultaneously.

Table 3.9 summarizes range of motion of the head in extension with and without the tensile spring in BirthView:

Table 3.9: ROM of the head in extension with and without the tensile spring (BirthView)

Extension	Angle (degrees)
with tensile spring	31
without tensile spring	35.5

Nevertheless, since the tensile spring allows some leeway with regards to the position of the head, relative to the trunk, the head allows further extension up to 43 degrees (see Figure 3.40). However it is still smaller than the aforementioned 72-76 degrees, acquired from the video.

The aforementioned ROM and trajectory problems can potentially be resolved



Figure 3.39: A newborn's head trajectory in flexion/extension.

by increasing the height of the neck, i.e. by increasing the gap between head and trunk.

3.3.4.3 Extreme lateral bending and flexion

The existing basic neck model consists of a tensile/compression and torsional springs with arbitrary stiffness values. The tensile stiffness coefficient is set to 10000 N/m, whereas the torsional stiffness is set to 100 Nm/deg at 30deg of axial rotation. Such configuration successfully simulated the cardinal movements with the neck's length of 12 mm as shown in the work by Gerikhanov (2017). However, the reported values for a fetal neck length, in the literature, are almost three times higher and around 36 mm on average (Luck et al., 2008).

With the adjusted length of the fetal neck, the simulation leads to the lateral bending of around 70deg, during internal rotation, which is possible according to the reported ROM by Öhman and Beckung (2008) (see Figure 3.42). However, the extreme lateral bending occurs when the head is flexed and rotated, which is physiologically impossible. There is a possibility that the elevated shoulders are blocking further lateral bending in real labour, however, this cannot be verified due to the lack of articulated shoulders in the simulation. Also there is a possibility that the birth canal itself does not allow the head to undergo extreme lateral flexion, however, this cannot be verified either due to the absence of a complete

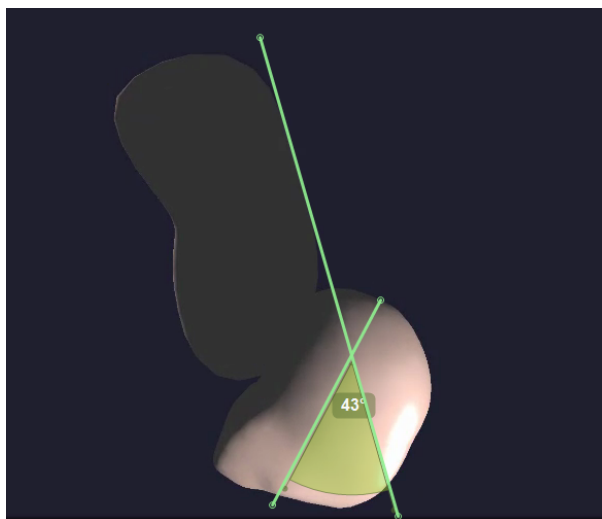


Figure 3.40: Measuring the extension angle of the fetal head in Kinovea. The screenshot was taken in BirthView at the peak extension of the fetal head. The pelvis and soft tissues are hidden for better visibility.

birth canal.

3.3.4.4 Rotation

The external rotation occurs with the improved neck model, however, due to a small rotational stiffness, takes a long time to follow a rotating trunk. Such phenomena is believed to take place due to neglecting the passive stiffness of neck muscles. The utilized stiffness values are of intervertebral discs and ligaments only. Therefore, it is evident that the real combined stiffness values, including muscle resistance, are higher than the predicted ones. When the rotational stiffness is increased up to 0.8 Nm/deg, which is 40 times higher than the reported 0.02 Nm/deg, the head rotates faster as expected. In fact, any value higher than the approximated 0.02 Nm/deg leads to a faster rotation, but 0.8 Nm/deg is considered to be visually plausible and sufficient.

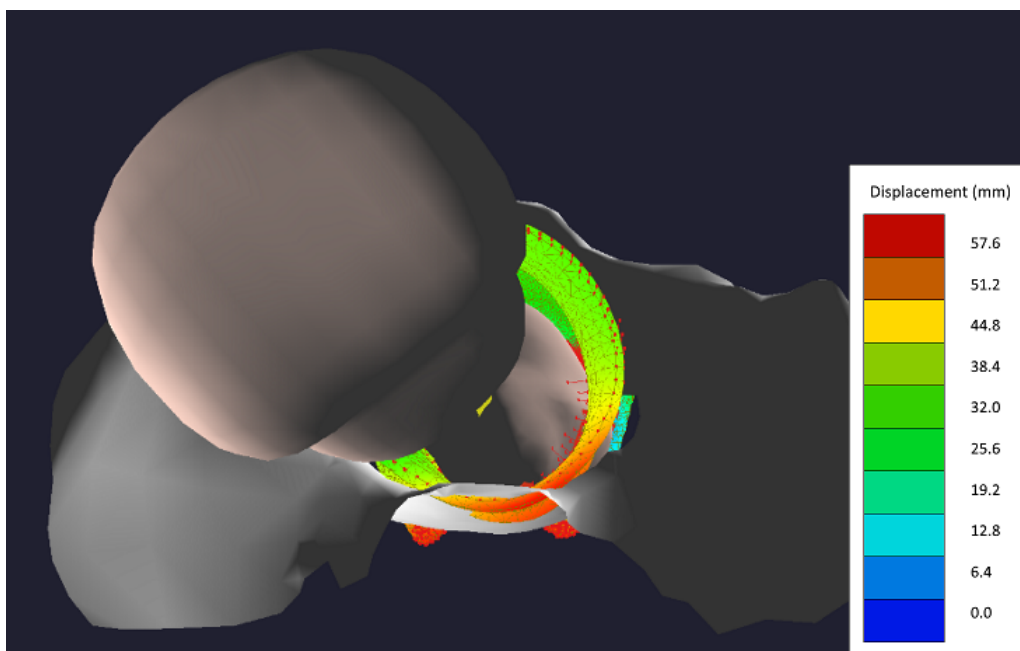


Figure 3.41: Extreme lateral bending of the fetal head with a longer neck. While the head is in flexion and is undergoing internal rotation, the expulsion force, propagated from the trunk to the head asymmetrically, laterally flexes the head. The displacements of the soft tissues (cervix, pelvic floor muscles and ligaments) are visualised through a colour legend.

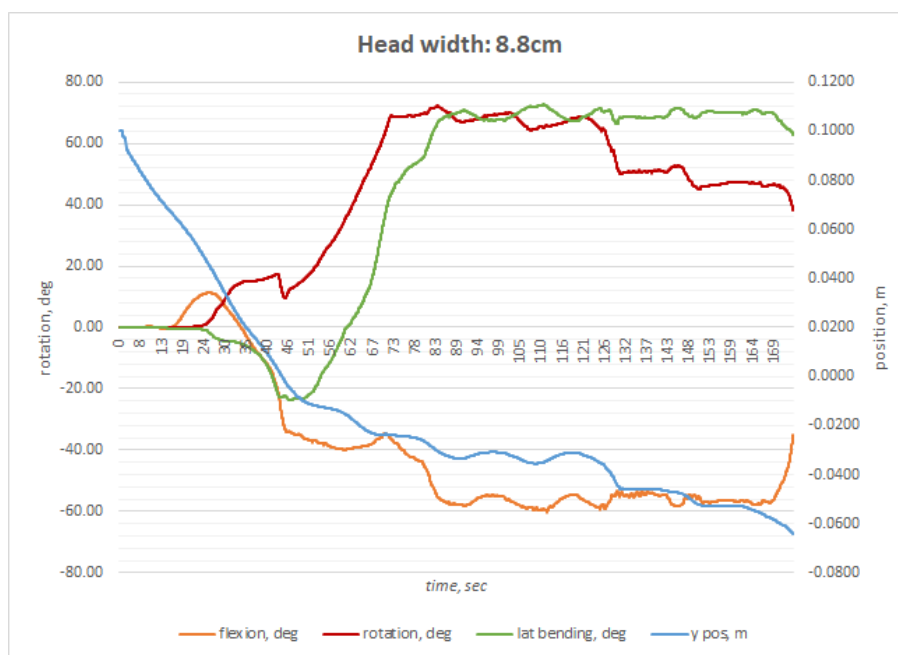


Figure 3.42: Simulating childbirth with a head width of 8.8cm and using the neck model NM01.

3.3.5 Improved Neck model (NM02)

3.3.5.1 Overview

The improved model has all the functionality of the previous model (NM01) and also facilitates resistance on bending movements namely flexion/extension. The calculation of the torque for the bending resistance has been performed similar to the torsional spring, but this time the torque is projected to the sagittal plane.

NM02 is utilizing the stiffness parameters presented in the research papers by Luck et al. (2008) and Luck (2012). In addition masses of the fetal skull, trunk and neck have also been changed in accordance with the data provided in these papers (Table 3.10). Hence, the new length of the neck is 3.61 cm and the masses of a trunk and head are 2.085 kg and 0.665 kg respectively. The linear and rotational damping values, for the fetal skull and trunk, are kept the same as in NM01 (see 3.3.3). The stiffness values for the tensile and bending springs are directly incorporated from Luck's data, specifically subject 07P, aged 0 months.

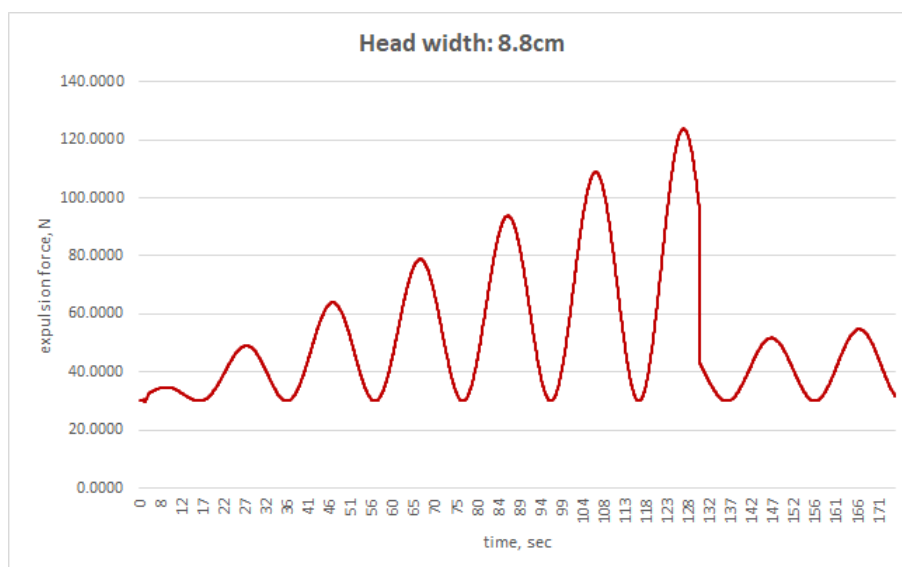


Figure 3.43: Graph of the increasing periodic expulsion force (red curve). The expulsion force is decreased after the delivery of the fetal head.

The tensile stiffness coefficient is equal to 7900 N/m under load displacement of 0.69mm (musculature is not considered at the moment). The flexion bending stiffness is the sum of stiffness values of three cervical segments (O-C2, C4-C5 and C6-C7) and is equal to 0.0245 Nm/degree. The extension bending stiffness is calculated to be 0.1271 Nm/degree. In addition, to avoid extreme bending, the stiffness values will increase 1000 times once the maximum angle has been reached. Since we do not possess data on torsional and lateral bending stiffness, these values will be set to 0 and spring constraints will be introduced to stop neck at angles specified in the studies of range of motion. Thus, the range of side rotation and lateral bending for the neck is limited to 52.6 and 34.05 degrees respectively (Öhman and Beckung, 2008).

3.3.5.2 Validation revisited

Although the previous neck models had both positive and negative effects on the simulation, none of them have actually been validated separately according to the realistic property values. Furthermore, the newly adopted mechanical properties, from the studies of Luck et al. and Coats et al., have not improved the childbirth

Table 3.10: Newborn PMHS Anthropometric Data (Luck et al., 2008)

PHMS ID	Age	Sex	Whole Body		Head			Cervical Spine
			Mass (kg)	Height (cm)	Mass (kg)	Breadth (cm)	Length (cm)	Length (cm)
05P	1 day	F	2.75	-	0.665	9.1	11.7	4.14
03P	3 days	M	-	-	0.492	8.5	10.3	3.61
06P	11 days	F	2.02	44.5	0.702	10.4	11.2	3.83

simulation in regards to the prominence of cardinal movements. In other words, a more accurate biofidelic infant neck model may not be accurately validated by means of the childbirth simulation. Therefore, a separate application has been developed specifically to allow professional obstetricians to test and validate the neck models and obtain their expert opinion on the biofidelity of the developed models (see Section 3.2.3.)

3.3.6 A one-pivot neck model with 6DOF spring constraint (NM03)

3.3.6.1 Overview

The model is only using a 6DOF spring constraint with the combined stiffness values from Section 3.2.2. In order to combine the stiffness values, we first find the mean of the stiffnesses for the whole cohort of newborns. Then we use the following equation (springs in series) in order to find the combined equivalent stiffness of the six cervical spine's segments.

$$\frac{1}{k_{eq}} = \frac{1}{k_1} + \frac{1}{k_2} + \frac{1}{k_3} + \frac{1}{k_4} + \frac{1}{k_5} + \frac{1}{k_6} \quad (3.21)$$

The acquired values are only approximations and needs to be adjusted in the simulation software. As reported by Duncan (1874), the tensile stiffness of newborns' neck, including muscles, is twice as bigger than the stiffness of ligaments and intervertebral discs. Therefore, we make an assumption that the approximated values will need to be increased depending on the observed behaviour of the neck. The model is compared to NM01 and NM02 in Chapter 4.

Table 3.11: Mean stiffness values for each cervical spine's segment and the combined equivalent stiffness of all segments. Compression and tension are given in N/m. Flexion, extension, lateral bending and axial rotation are given in Nm/deg.

Segments	Flexion	Extension	Compression	Tension	Lateral bending	Axial rotation
O-C2	0.31	0.37	2540.00	9580.00	0.08	0.23
C2-C3	0.31	0.37	2540.00	9580.00	0.08	0.23
C3-C4	0.03	0.14	24650.00	46637.50	0.29	0.02
C4-C5	0.03	0.14	24650.00	46637.50	0.29	0.02
C5-C6	0.31	0.40	28225.00	43662.50	0.14	0.13
C6-C7	0.31	0.40	28225.00	43662.50	0.14	0.13
Combined	0.01	0.04	1064.51	3361.82	0.02	0.01

3.3.6.2 Validation

The neck model NM03 is compared to NM01 and NM02 in Sections 4.6 and 4.7. It is shown that NM01 and NM02 neck models are incapable of resisting lateral bending and, therefore, the fetal head undergoes extreme lateral flexion especially with a longer neck. In addition, since both NM01 and NM02 can only simulate the neck length of around 1.24cm, the fetal head comes into contact with the chest at 30 degrees.

NM03 resolves both issues by introducing resistance in lateral bending and allowing for longer necks to be used in the simulation software. However, when using the approximated stiffness values (see Section 3.2.2) of the cervical spine segments, NM03 is not capable of resisting the extreme lateral bending either due. Hence, to compensate for the unrealistic extreme lateral bending, the stiffness of the torsional spring, resisting lateral bending, is increased up to an arbitrary 2 Nm/deg when the head is flexed and rotated¹. These adjustments lead towards successful internal rotation, however, the head undergoes increased flexion due to the increased length of the neck and gets arrested between sacrum and pelvic floor muscles. The forehead is pushing against sacrum and that contributes to further flexion. In order to deflex the head the expulsion force is increased up to 180N to widen the pelvic outlet by stretching the pelvic floor muscles. Increasing the expulsion force up to 180N leads to a successful delivery of the fetal head with a longer neck (see Section 4.7).

3.3.7 Two pivot neck model (NM04)

3.3.7.1 Overview

Once the validation of the neck model in Section 3.3.5 has been performed, it was evident that a more complex neck model is required in order to simulate realistic motion of the fetal head.

As the next step towards a more realistic neck model, a two-pivot neck model was developed with an additional cylinder between the skull and torso. The

¹When the head is flexed and rotated, the ROM for the side bending drastically decreases due to the physiology of the cervical spine

Table 3.12: Combined stiffness for upper cervical spine

Segments	Flexion (Nm/deg)	Extension (Nm/deg)	Compression (N/m)	Tension (N/m)	Lateral bend (Nm/deg)	Axial rot (Nm/deg)
O-C2	0.3130	0.3665	2540.0000	9580.0000	0.0804	0.2259
C2-C3	0.3130	0.3665	2540.0000	9580.0000	0.0804	0.2259
Combined	0.1565	0.1833	1270.0000	4790.0000	0.0402	0.1130

Table 3.13: Combined stiffness for lower cervical spine

Segments	Flexion (Nm/deg)	Extension (Nm/deg)	Compression (N/m)	Tension (N/m)	Lateral bend (Nm/deg)	Axial rot (Nm/deg)
C3-C4	0.0319	0.1449	24650.00	46637.50	0.2870	0.0249
C4-C5	0.0319	0.1449	24650.00	46637.50	0.2870	0.0249
C5-C6	0.3110	0.4012	28225.00	43662.50	0.1369	0.1289
C6-C7	0.3110	0.4012	28225.00	43662.50	0.1369	0.1289
Combined	0.0145	0.0532	6579.1608	11275.2483	0.0463	0.0104

cylinder is connected to the skull and torso with two 6DOF spring constraints on both sides with the combined stiffness values of the cervical vertebrae.

As mentioned in Section 2.2.2 two-pivot models are capable of efficiently predicting global head positions and orientations.

3.3.7.2 Stiffness of springs in 6DOF constraint

Since the model consists of two pivot points the whole cervical spine needs to be split into two parts, unlike the one-pivot neck model wherein the whole neck was approximated by one constraint. Therefore, the acquired stiffness values in Section 3.2.2 are combined into two parts: upper and lower cervical spine. This is done by using the same approach as in the previous section, i.e. by calculating spring stiffness that is equivalent to a system of springs in series. The resulting values are presented in Tables 3.13 and 3.12.

3.3.8 Conclusion

A number of neck models have been presented in this section. The main objective of the developed neck models is to improve BirthView to arrive at a patient-

specific simulation. Among all the developed models, NM03, in conjunction with the complete mechanical properties (see Section 3.2.2), has proven to produce better results and led to successful simulations of childbirth for different lengths of the fetal neck (see Appendix A). NM03 is sufficiently accurate, customisable and computationally efficient. NM03 is capable of simulating different strength of the fetal neck due to the 6dof bushing element, allowing to specify separate stiffness for the motion of the fetal head in any direction. The limitations of the model are discussed in Section 5.3.

Chapter 4

Optimization of childbirth simulation

4.1 Mesh Generation

4.1.1 Overview

This section is dedicated to describing the sources of the acquired CT scans, the techniques used in processing the scans and modelling the meshes of a female pelvis, infant shoulder complex, ribs and cervical vertebrae, used for validating the simulation software.

A computer graphics software Blender¹ was used for processing of the meshes.

The main techniques employed for the mesh processing in Blender are remeshing, knife/bisect tools, smoothing and decimation (Garland and Heckbert, 1997).

4.1.2 Gynecoid pelvis

The mesh was acquired in STL format from CT scans openly published on Embody3D ².

¹Blender is a free and open-source 3D computer graphics software toolset used for creating animated films, visual effects, art, 3D printed models, interactive 3D applications and video games.

²Embod3D is an online library of medical 3D printable models

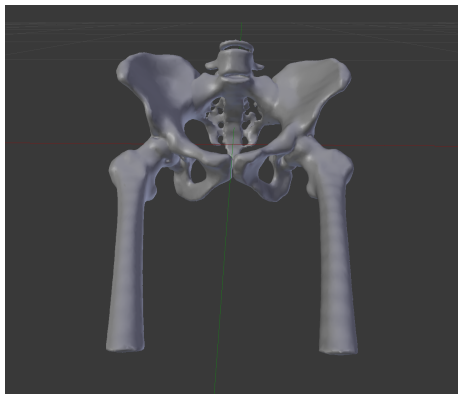


Figure 4.1: Gynecoid pelvis with rigid sacrum and coccyx.

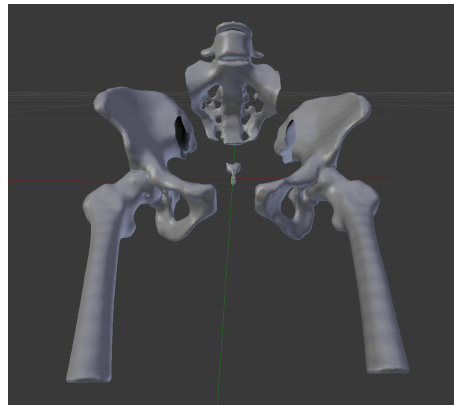


Figure 4.2: Gynecoid pelvis with separated sacrum and coccyx.

The initial mesh consisted of the pelvis, spine and ribs. Since we were interested in the pelvis only, the former was separated from the spine and ribs by using Bisect tool.

The separated pelvis had around 500K triangles. The high number of triangles requires more computational power, especially, during collision detection and response phase. Therefore, the mesh was decimated down to 12K triangles.

For simulating pelvic moulding, the mesh was further cut into separate sacrum, coccyx, left and right bones using a Knife tool.

Figures 4.1 and 4.2 illustrate the mesh before and after the separation.

4.1.3 Spine, shoulders and rib cage

The anonymized CT scans of 6 months and 15 months old baby girls were obtained from the Department of Roentgenology in Children Hospital No 2, Grozny, Russia. The scans were used to acquire realistic 3D models of the skull, spine, shoulders and chest of a newborn.

The volume was segmented in the software 3DSlicer, using thresholding, into an STL mesh model. Following that the model was decimated in Blender in order to decrease the number of triangles for the sake of increased computational speed.

The model was used to simulate a shoulder complex.

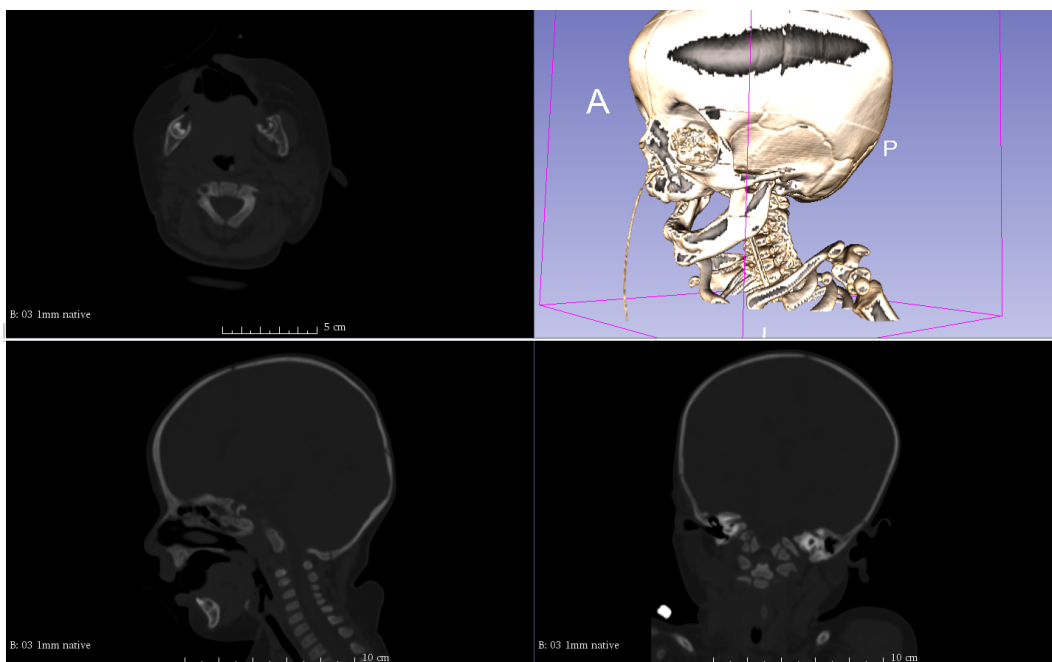


Figure 4.3: A CT scan of a 6 months old baby girl rendered in 3D Slicer

4.2 Sacrum mobility

4.2.1 Introduction

Sacroiliac body (SI) or sacrum undergoes an increase in mobility during labour (Vleeming et al., 2012). Limited mobility of the sacrum may lead to the arrest of the fetal head during internal rotation due to lack of space in the anterior-posterior diameter of the pelvic outlet. In this section two experiments are conducted with the new pelvic mesh model (see Section 4.1.2) to study the effects of the pelvic moulding on labour. The first experiment is using a static sacrum (see Figures 4.4 and 4.5), whereas the second experiment is using a mobile sacrum. The coccyx is deflexed by twenty degrees in both cases to create more space in the pelvic outlet.

4.2.2 Experimental setup

The experimental setup is summarized in Table 4.1. FE sacrospinous ligaments are used in the simulation with the bulk and shear modulus equal to 1MPa and 66kPa respectively. The sacrum is connected to the rest of the pelvis with a bushing element. The stiffness values for the bushing element in flexion and rotation have been set to 0.0125 Nm/degree. These values have been found experimentally.

Table 4.1: The experimental setup of BirthView for the experimental study on pelvic moulding

	<i>Lin damping</i>	<i>Rot damping</i>	<i>Mass</i>	<i>Position</i> x,y,z	<i>Orientation</i>			
Fetal head	9650	3	1.5 kg	[0.0133, 0.1, 0.0]	LOT*			
Fetal trunk	3650	3	2.5 kg	[0.0133, 0.2151, 0.0]	LOT*			
Maternal pelvis	3650	1	1 kg	[0.0, 0.0, 0.0]	n/a			
* LOT - left-occiput transverse position (see Figure)								
	<i>Lin damping</i>	<i>Rot damping</i>	<i>Mass</i>	<i>Bushing element</i>				
				k_f	k_e	k_{lb}	k_t	k
Sacrum	3650	1	1 kg	0.0125*	0	0	0.0125*	3000
* the spring starts resisting motion only when the rotation is equal to 10 degrees								
	<i>Length</i>	<i>Position on skull</i>	<i>Bushing element</i>					
			k_f	k_e	k_{lb}	k_t	k	
Fetal neck	1.2	[0.0, 0.0, 0.0]*	0.01	0.04	2	0.1	3600	
* origin of the skull is at foramen magnum								
k_f, k_e, k_{lb}, k_t - stiffness coefficients in flexion, extension, lateral bending and rotation								
k - stiffness coefficient resisting elongation, compression and shear translations								
	<i>Bulk modulus</i>	<i>Shear modulus</i>	<i>Number of elements</i>	<i>Number of nodes</i>				
PF muscles	1MPa	66kPa	18788	6577				
Sacrospinous ligaments	1MPa	66kPa	8767	2816				

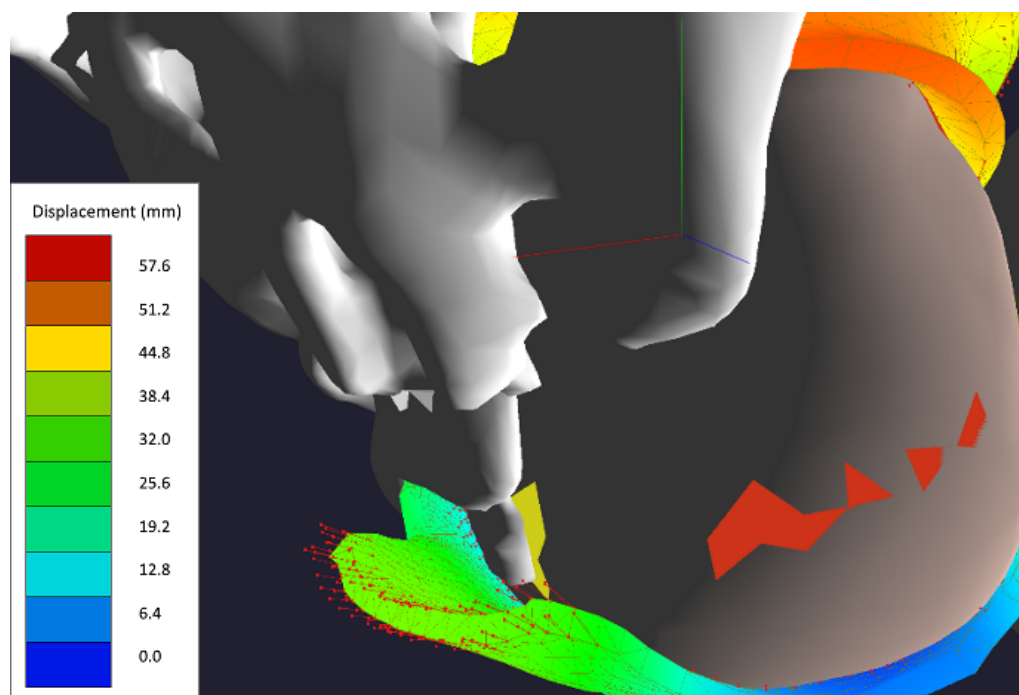


Figure 4.4: The fetal head is undergoing internal rotation and the sacrum, including the coccyx, is static. The yellow highlights represent contacts of the head with the pelvis. Sacrospinous ligaments are hidden to have a better view of the contact (red highlights represent contacts with the sacrospinous ligaments). The coccyx is already deflexed by twenty degrees (see Section 1.4.4). Further rotation of the head is not possible due to the static coccyx pushing the head toward ischial spines. The displacements of the soft tissues (cervix, pelvic floor muscles and ligaments) are visualised through a colour legend.

4.2.3 Analysis

The results show that with a static sacrum for the smallest reported fetal head of 9.07 cm, the head is unable to complete the internal rotation due to the coccyx and sacrum obstructing the motion (see Figure 4.6). However, with a mobile sacrum, the pelvic outlet is capable of accommodating the head due to the increased anterior-posterior diameter (see Figure 4.7).

The sacrum in the simulation opened by 10 degrees around X-axis, which is larger than the reported total 3.3 degrees (see Section 1.4.3). However, as

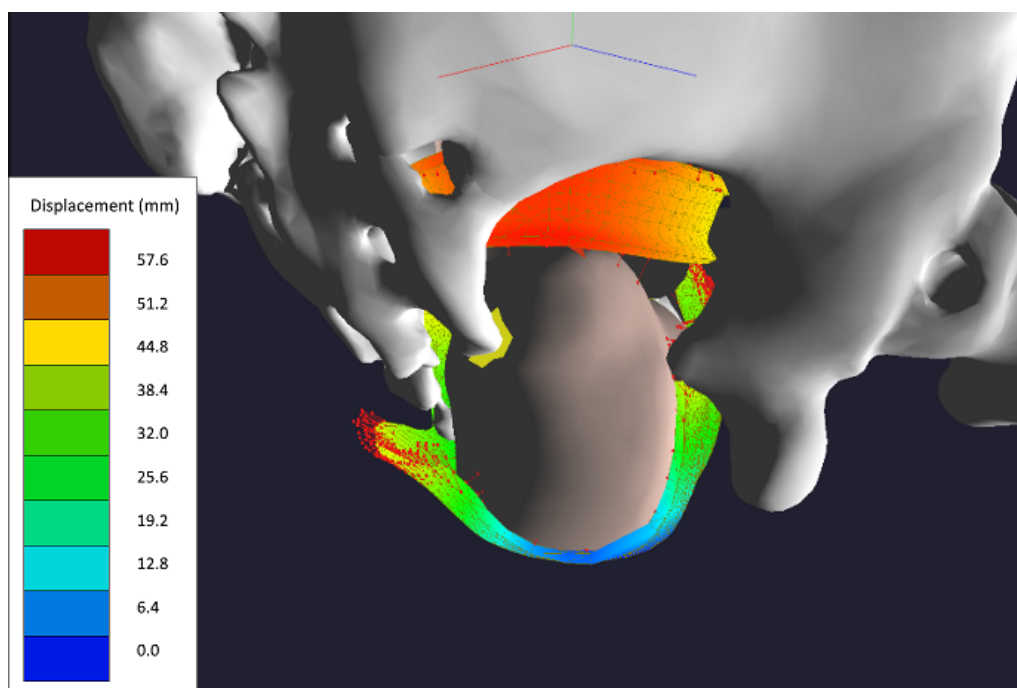


Figure 4.5: With a bigger expulsion force exerted on the fetal head, the latter comes into contact with the part of sacrum above the coccyx, which further restricts the motion of the head. The highlighted yellow area on the fetal face represents the contact of the face with the sacrum. The displacements of the soft tissues (cervix, pelvic floor muscles and ligaments) are visualised through a colour legend.

reported by Vleeming et al. (2012) there should be an increase in mobility of the sacrum during labour.

4.3 Expulsion

4.3.1 Introduction

BirthView successfully simulated the majority of the cardinal movements. However, the last cardinal movement, namely, expulsion was not possible due to the fetal trunk being stuck in the pelvic floor muscles.

A number of experiments have been conducted in order to resolve the above-

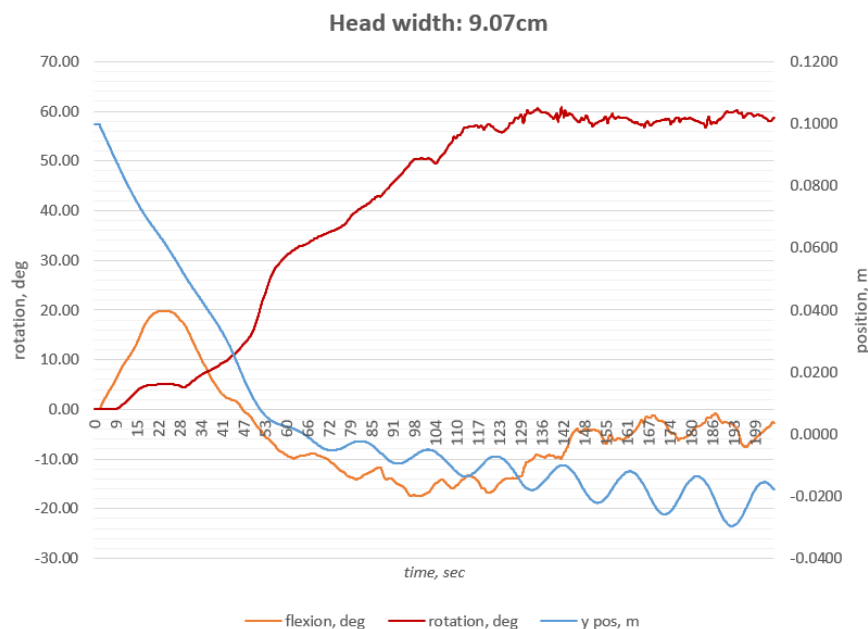


Figure 4.6: Graph of simulating labour with a **static sacrum**. The head is initially deflexed (the positive orange curve) however after engaging with the pelvic inlet goes into flexion. While flexing the head simultaneously rotates up to 60 degrees clockwise (the red curve) and halts due to hitting the sacrum and, as a result, being unable to complete the internal rotation. The blue curve represents descent. Further deflexion and descent are associated with downward stretch of pelvic floor muscles, nevertheless, the rotation is remains the same.

mentioned issue and to successfully simulate expulsion, i.e. delivery of the trunk.

4.3.2 Analysis

From the MRI video (Bamberg et al., 2012) (see Figures 4.8 and 4.9) it is clearly visible that the fetal body is following the curved birth canal, which is currently absent in the simulation. Moreover, even if the birth canal was present, the rigid body cannot possibly fit through the birth canal due to the latter being curved. Hence, a complete spine with a rib cage is required in order for the fetal body to be born.

Additionally, currently the fetal trunk is kept upright by a bending spring, which tries to keep the orientation of the trunk vertical and, therefore, the body

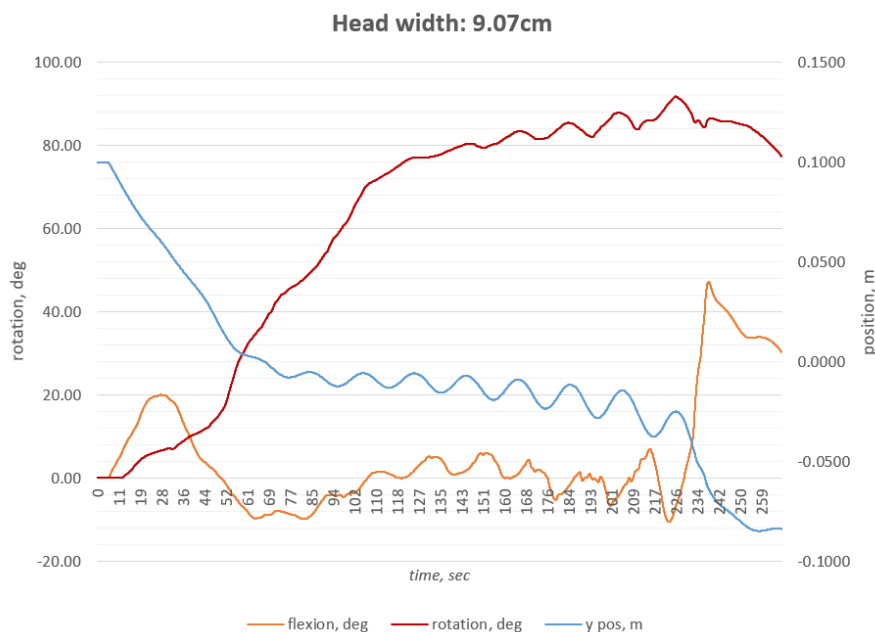


Figure 4.7: Graph of simulating labour with a **mobile sacrum**. The head is initially deflexed (the positive orange curve) however after engaging with the pelvic inlet goes into flexion. Unlike in the Figure 4.6 the head gradually turns by 90 degrees (the red curve), thus, completing the internal rotation and is now in OA position. The jiggling between flexion and extension (the orange curve) between 94 and 217 seconds corresponds to the motion of the sacrum, rotating along sagittal and transverse planes.

is not capable of following the fetal head through the birth canal (see Figure 4.10).

It is essential to have the body following the fetal head through the birth canal in order to simulate difficult birth scenarios and complications such as shoulder dystocia.

4.3.3 Affects of disabling the bending spring after the fetal head is born

An observation was made from the video that the fetal trunk follows more or less the same trajectory as the fetal head. For that reason, the bending spring, keeping the trunk in upright position, was disabled when the head was born.



Figure 4.8: The fetal head is fully flexed and is about to undergo extension (Bamberg et al., 2012).

The experiment resulted in the bottom of the trunk coming into contact with the back side of the maternal pelvis and its subsequent arrest between the bony pelvis and pelvic floor muscles.

This result reconfirms the necessity to develop a flexible torso to observe expulsion and potentially shoulder dystocia.

4.3.4 Expulsion of shoulders

Due to the trunk being rigid and incapable of bending in order to go through the birth passage, an alternative solution was employed. A new scene was set up with only the upper half of the trunk to avoid contact with the pelvis while changing its direction to follow the trajectory of the fetal head (see Figure 4.11). Figures 4.12 and 4.13 show successful delivery of the shoulders and since shoulders are the widest part of the body, it is fair to conclude that an additional cardinal movement was observed.

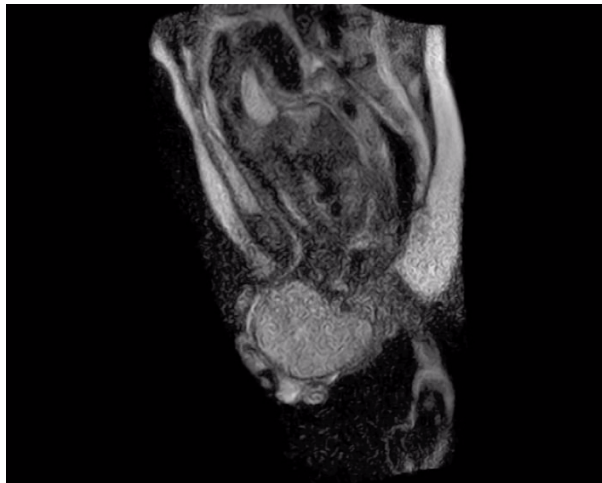


Figure 4.9: The fetal head is undergoing extension (Bamberg et al., 2012).

4.4 Shoulder dystocia

4.4.1 Introduction

In this section an attempt was made to observe shoulder dystocia by adjusting the trajectory of the fetal trunk. After running the simulations in the previous Section 4.3 it was visually evident that the width of the shoulders was too small in order for the shoulder dystocia to happen. The width of the shoulders was around 7cm for a fetal head with BPD of 8.8cm, whereas average shoulders' width for newborns is around 12.06-12.76cm (Verspyck et al., 1999; Kastler et al., 1993).

Therefore, the shoulders were initially widened in Blender up to 11cm. This lead to the shoulders' arrest below and to the left of the pubic bone (see Figure 4.14). This is most likely caused by absence of a complete birth canal to direct the shoulders to the correct position. Currently we simulate the affects of the curvature of the birth canal by disabling the spring, keeping the body in upright position. By running the simulation multiple times, a conclusion was made that the outcome of the simulation depends on the curvature of the birth canal.

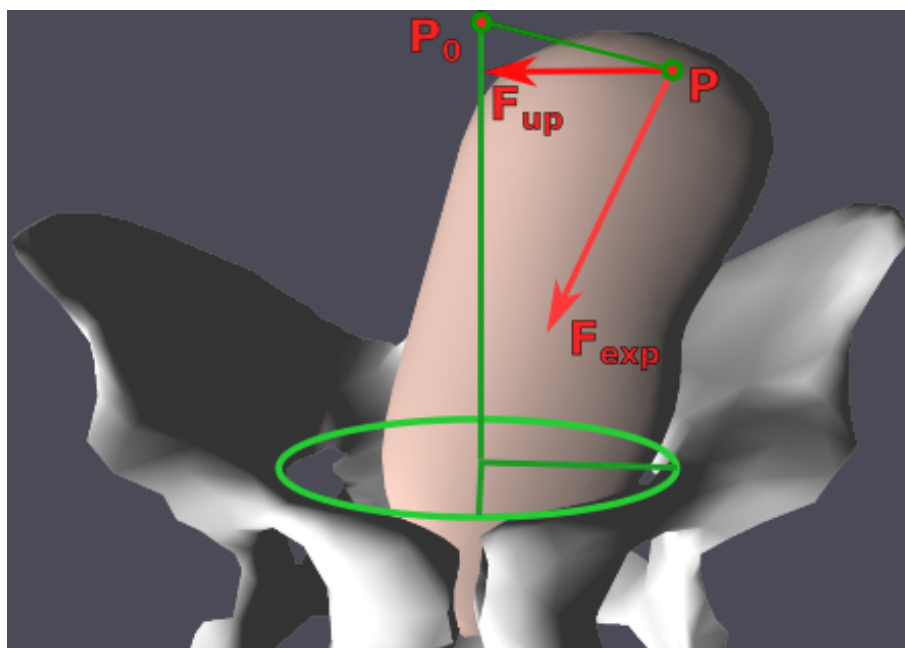


Figure 4.10: The expulsion force F_{exp} is exerted at the point P . The force F_{up} is pulling the trunk in the upwards position to keep the trunk vertical. (Gerikhanov, 2017).

4.4.2 Experiment

In the latest experiment we increased the width of the shoulders up to 12cm, which lead to the shoulders being arrested behind the pubic symphysis (see Figure 4.15). Currently the only possible way to resolve the problem is by simulating application of the suprapubic pressure or Rubin maneuver¹ due to absence of articulated shoulders. Potentially a haptic device can be integrated into the simulation in order to resolve the observed phenomenon.

As mentioned above, the simulation lack mobile fetal shoulders, which are crucial to deliver the shoulders during expulsion stage (see Section 1.2.5). Articulated shoulders would facilitate observing different scenarios of shoulder dystocia and their resolutions.

¹Rubin maneuvers are used to deliver the baby in case of shoulder dystocia. The first Rubin maneuver is the rotation of the fetal anterior shoulder under the maternal symphysis pubis. The second Rubin maneuver is the rotation of the posterior shoulder in a clockwise direction by pressing on the dorsal surface of the posterior shoulder (Benrubi, 2010)

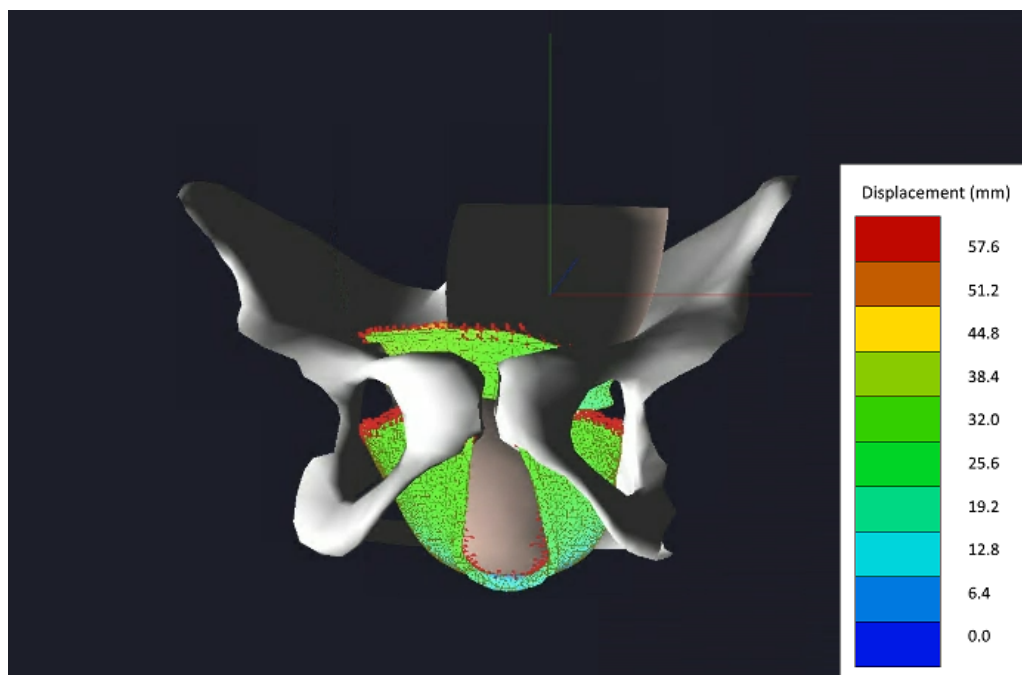


Figure 4.11: Simulation with a trunk cut in half. The displacements of the soft tissues (cervix, pelvic floor muscles and ligaments) are visualised through a colour legend.

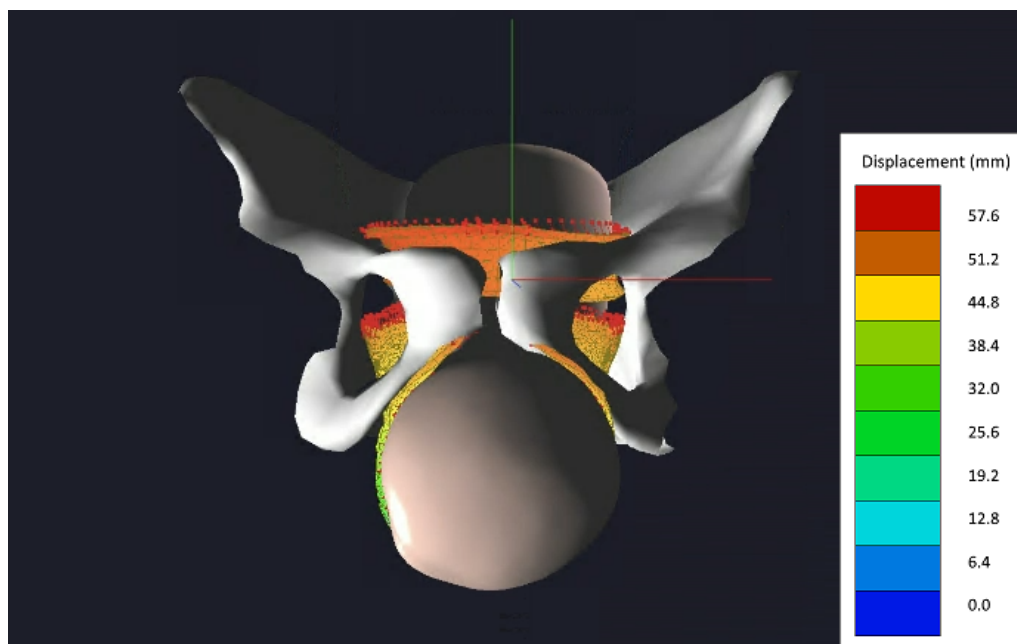


Figure 4.12: Delivery of a fetus, front view. The displacements of the soft tissues (cervix, pelvic floor muscles and ligaments) are visualised through a colour legend.

4.5 Validation of the BirthView TLED procedure

4.5.1 Introduction

Total Lagrangian Explicit Dynamics (TLED) BirthView is using an explicit finite-element method, also known as the Total Lagrangian Explicit Dynamics (TLED) to calculate the deformations of the soft tissues, namely cervix, pelvic floor muscles and sacrospinous ligaments (Lapeer et al., 2019). TLED is coupled with a modified projection based contact method used to calculate the contact forces causing the deformation in the aforementioned soft tissues.

A number of experiments were conducted in order to validate the accuracy of TLED against Abaqus software in BirthView (Gerikhanov, 2017). The validation setup consisted of a simple finite element cube, comprised of 244 tetrahedral elements, with dimensions of 1m x 1m x 1m. The cube had Neo-Hookean hyper-elastic material properties with a shear modulus of 660 kPa and a bulk modulus of 1 MPa. The material density was 1000 kg/m³. The cube was encastred at

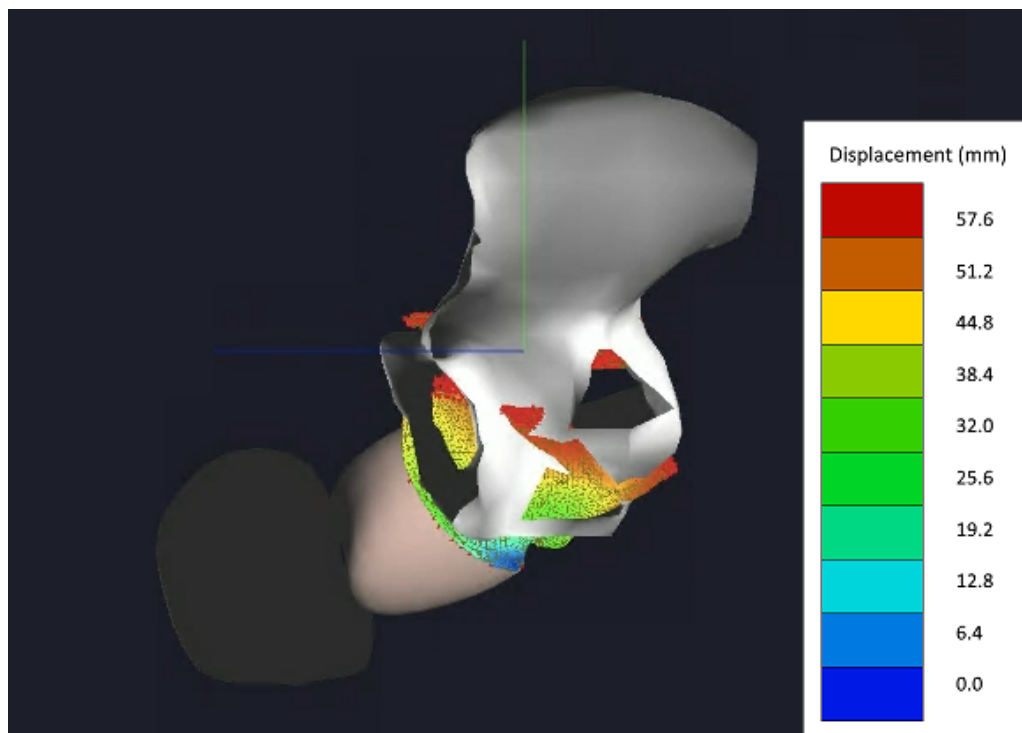


Figure 4.13: Delivery of a fetus, side view. The displacements of the soft tissues (cervix, pelvic floor muscles and ligaments) are visualised through a colour legend.

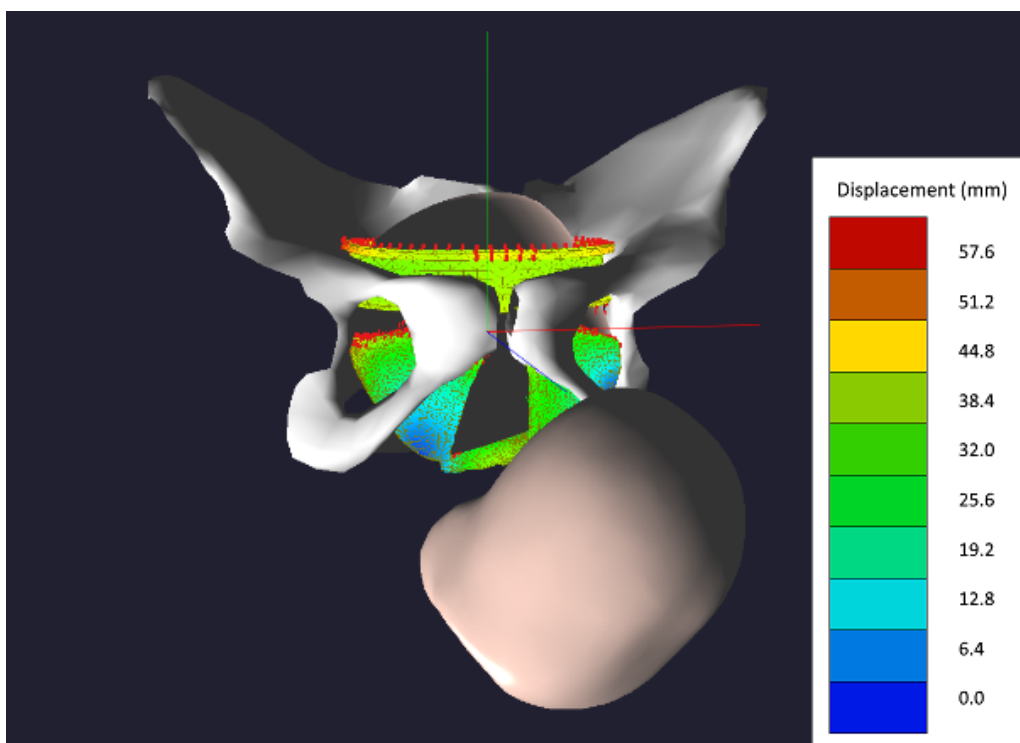


Figure 4.14: Shoulder arrest (shoulder dystocia) below and left to the pubic symphysis. Shoulder width is 11cm. The displacements of the soft tissues (cervix, pelvic floor muscles and ligaments) are visualised through a colour legend.

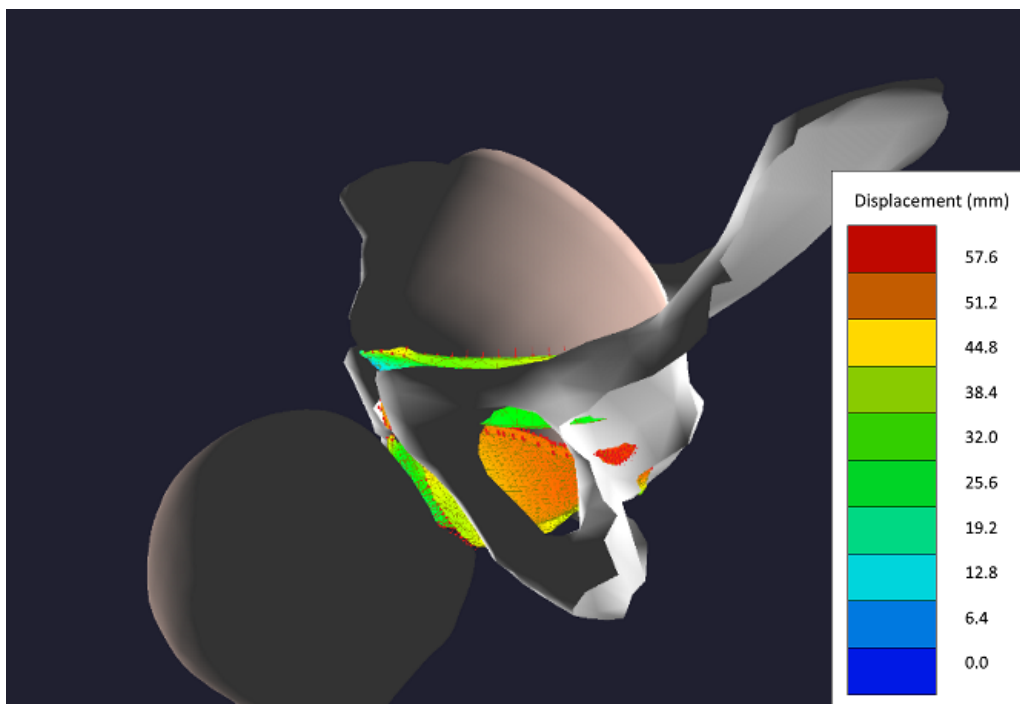


Figure 4.15: Shoulder arrest (shoulder dystocia) behind the pubic symphysis. Shoulders width is 12cm. The displacements of the soft tissues (cervix, pelvic floor muscles and ligaments) are visualised through a colour legend.

Table 4.2: Comparison of BirthView implementation of TLED with projection based contact against Abaqus Explicit Contact.

Force (N)	Uy,max(mm)		Error	
	BirthView	Abaqus	mm	%
98.1	5.91	5.795	0.115	1.95
196.2	11.12	11.125	0.005	4.5e-4

Table 4.3: Increasing the number of tetrahedral elements of a Neo-hookean hyperelastic cube subjected to distributed force shows that project based contact method implemented in BirthView is not sensitive to mesh complexity.

# elements	Uy,max(mm)	Error(mm)
157	24.44	0.06
570	24.46	0.04
2887	24.48	0.02
21588	24.50	0.00

the base. The top face was subjected to compression force of 98.1 N and 196.2 N, replicating the pressure from a pressure plate with masses 10kg and 20 kg respectively. The results are summarized in Table 4.2.

For 98.1 N there is 1.95% error between the projection based method and Abaqus Explicit, whereas the error is even smaller for 196.2 N.

The next experiment by Gerikhanov (2017) showed that the project based contact method is not sensitive to the mesh complexity. The same cube was subjected to a compressive force of 491 N. The number of tetrahedral elements ranged from 127 to 21588. Table 4.3 shows the results.

However, the abovementioned validation experiments are not representative of a real childbirth scenario in BirthView, since both fetal head and pelvic floor muscles have curved surfaces. Also, as mentioned earlier, the compression force above is only a replication of a pressure plate and, therefore, we extended and combined these experiments to include a real rigid body plate, as well as a sphere, pushing vertically down by their weight on top of the cube under gravitational force of 9.81 N. These experiments were run both in BirthView and Abaqus.

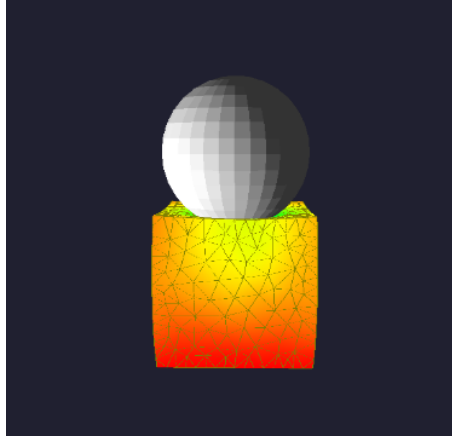


Figure 4.16: Sphere on cube experiment in BirthView.

4.5.2 Sphere on cube experiment

Around 173 experiments have been conducted in total with the following setup. The same cube, comprised of first-order tetrahedral elements, is encastred at the base. The cube had a Neo-Hookean material properties with a bulk modulus of 1MPa and a shear modulus of 66 kPa. These values needed to be converted to polynomial coefficients C_{10} and D_1 for Abaqus, where

$$C_{10} = \mu/2 = 33kP \quad (4.1)$$

$$D_1 = 2/k = 0.002kPa^{-1} \quad (4.2)$$

where μ - shear modulus, k - bulk modulus

The number of tetrahedral elements were increased from 126 to 12490 in 5 steps. Two spheres, 10 kg and 15 kg, were separately placed on top of the cube's surface. Table 4.4 shows the results of the experiments.

The results show that the difference between TLED/pDN and Abaqus Explicit for higher number of elements is 5% when a 10 kg sphere is placed on the cube and only 1% for a 15 kg sphere.

In addition, the results confirm that, indeed, BirthView implementation of projection based contact method (TLED/pDN) is less sensitive to a number

Table 4.4: Comparison of BirthView implementation of project based contact method against Abaqus explicit.

Masssphere	# elements	BirthView	Abaqus	Diff. (%)
10	126	17.86	14.85	-17
	558	19.23	16.11	-16
	1256	19.53	17.77	-9
	5720	20.19	20.40	+1
	12490	20.21	21.27	+5
15	126	26.74	20.04	-25
	558	27.69	21.53	-22
	1256	27.56	24.25	-12
	5720	28.77	27.48	-5
	12490	28.72	28.42	-1

of tetrahedral elements as compared to Abaqus Explicit contact method. Also TLED/pDN even with the least number of elements is closer to the exact solution. We made an educated assumption that deflection of a cube for a higher number of elements presents the most accurate solution (20.21mm for BirthView and 21.27mm for Abaqus).

Moreover, Figures 1 and 2 illustrates that TLED/pDN exhibits more stable behaviour at around 6000 elements and above for the cube and is closer to the correct solution even for lower number of elements.

Other contributions to the paper:

- A number of changes had to be done to BirthView software in order to facilitate the aforementioned experiments. The sphere used to slide off the cube while it was in contact due to asymmetrical position of tetrahedrons in the generated tetrahedral cube. For that reason, we implemented an option to clamp motion of the sphere vertically by introducing a new member variable to RigidBody Component class.
- The ExportInp Component is responsible for exporting meshes into Abaqus INP format. It had to be slightly adjusted to produce clean INP files of the cube in BirthView. The component previously used to produce five different copies of elements and nodes and, hence, the generated file could not be uploaded into Abaqus to run corresponding experiments.

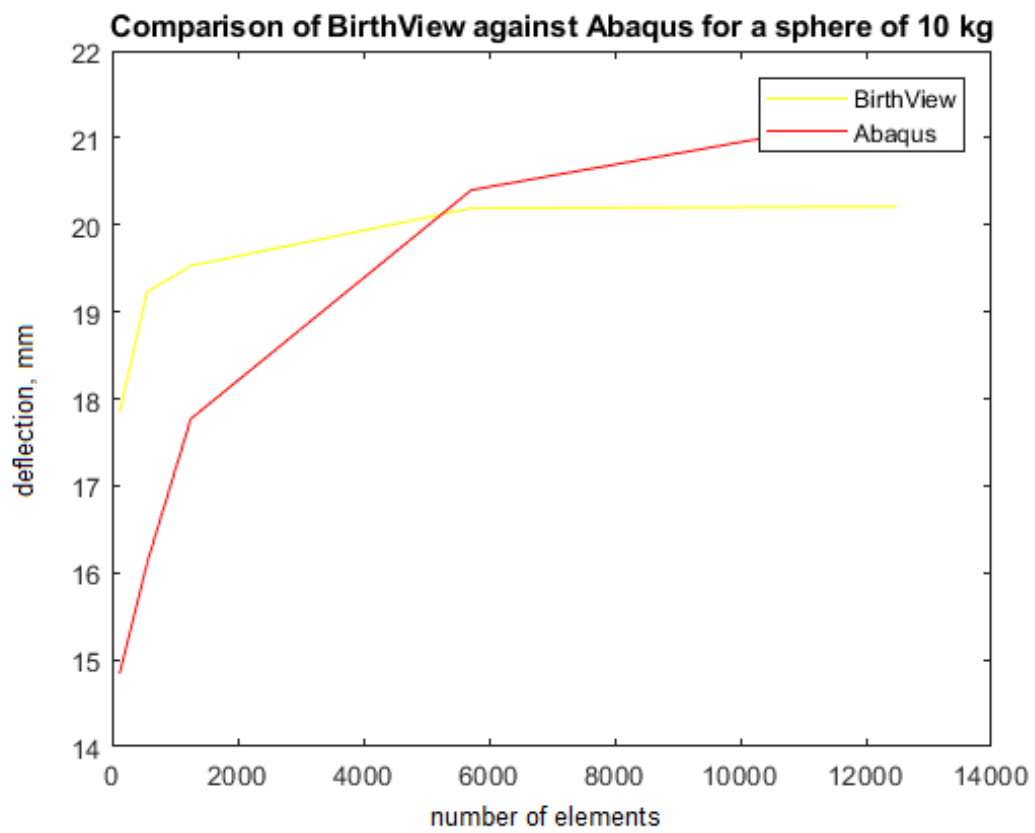


Figure 4.17: Comparison of BirthView TLED/pDN against Abaqus Explicit for a sphere of 10 kg released on a cube.

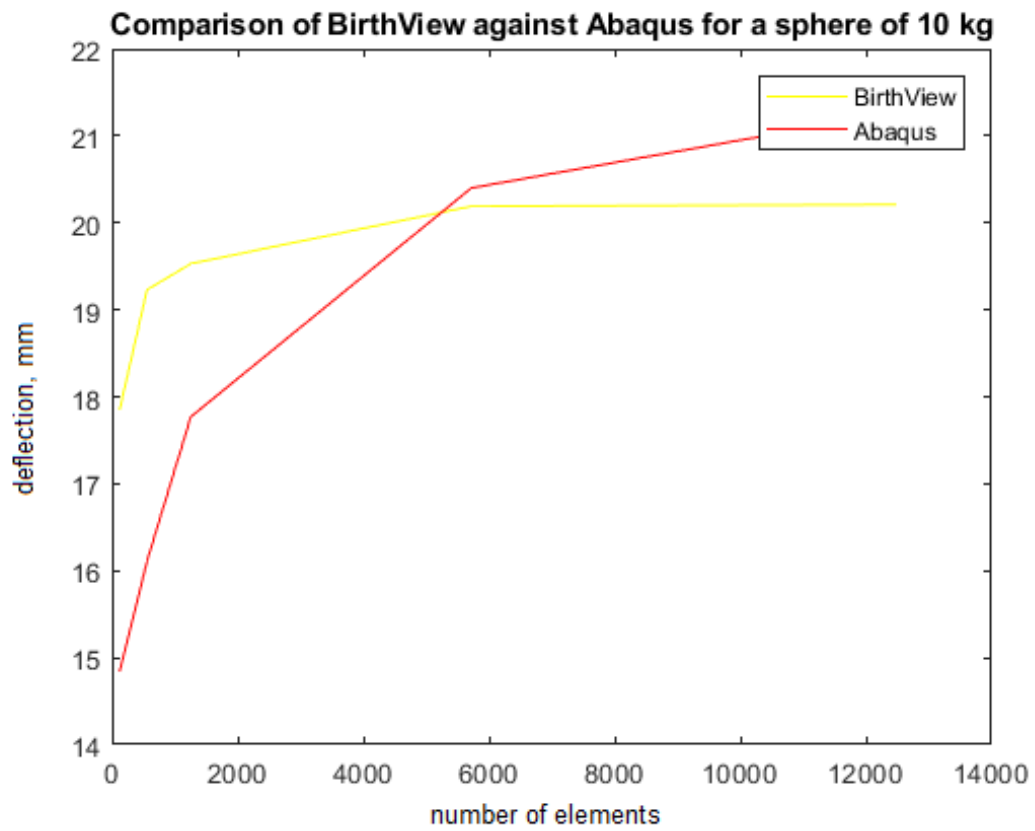


Figure 4.18: Comparison of BirthView TLED/pDN against Abaqus Explicit for a sphere of 15 kg released on a cube.

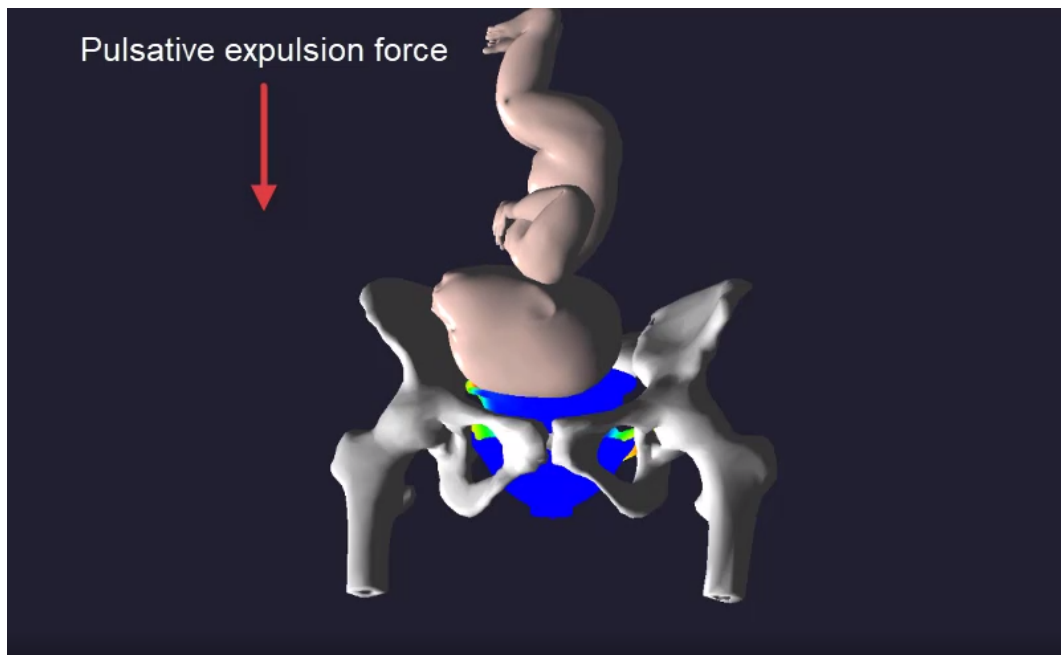


Figure 4.19: New mesh models for the fetus and maternal pelvis.

- Mesh adjustments in Blender. The initial fetal head and trunk meshes were replaced by more visually appropriate meshes (see Figure 4.19).
- Camtasia Studio was used in order to record videos of the childbirth simulation in both LOA (left occipital anterior) and ROA (right occipital anterior) positions (see Figure 1.7).
- The previous pelvic mesh model was overly simplified and, therefore, was adjusted accordingly to include a more detailed mesh model (see Figure 4.19).

4.6 Experimental study of OP position

4.6.1 Overview

This section describes childbirth when the head is in a direct occipitoposterior (OP) position. In direct OP the fetal head's forehead is pointing anteriorly with

respect to the maternal pelvis (see Figure 1.7). The OP positions prolong labour and potentially can cause traumas to the pelvic floor muscles (Biancuzzo, 1993).

In real labour midwives use various techniques in order to facilitate delivery of a fetus in direct OP position. One of such techniques is tilting the pelvis forward and arching the spine to facilitate early flexion.

This section covers scenarios with both the basic neck model (NM01) and 6DOF spring constraint neck model (NM03). It is important to cover the case with the basic spring neck model for the complete picture and to observe how the updated neck model affects the simulation.

4.6.2 Direct OP using the old neck model (NM01)

The head in OP position is slightly above the pelvic brim. The head width is 8.80cm. The pelvis is in normal orientation, i.e. not tilted anteriorly. The initial applied expulsion force ranges between 30N and 40N. The expulsion force was reduced since the default range between 30N to 150N leads to extreme lateral flexion during internal rotation. On the onset of the simulation, the head descends into the pelvic inlet and gets engaged with the pelvic brim. The force, propagated through the neck, contributes towards flexion, which leads to further descent until the head comes into contact with the pelvic floor muscles. At this point, the head is fully flexed and the occiput is in contact with the pelvic floor muscles. Unless the expulsion force is increased, the head will remain in this position. Further increase of expulsion force up to 80N, at around 88 seconds of the simulation, results in onset of internal rotation of 30 degrees clockwise and results in extreme lateral bending (see Figure 4.20 and 4.21).

4.6.3 Direct OP using the new neck model (NM03)

The head in OP position is slightly above the pelvic brim. The head width is 8.80cm. The pelvis is in normal orientation, i.e. not tilted anteriorly. The initial applied expulsion force ranges between 30N and 150N. On the onset of the simulation, the head descends into the pelvic inlet and gets engaged with the pelvic brim. The force, propagated through the neck, contributes towards flexion, which leads to further descent until the head comes into contact with the

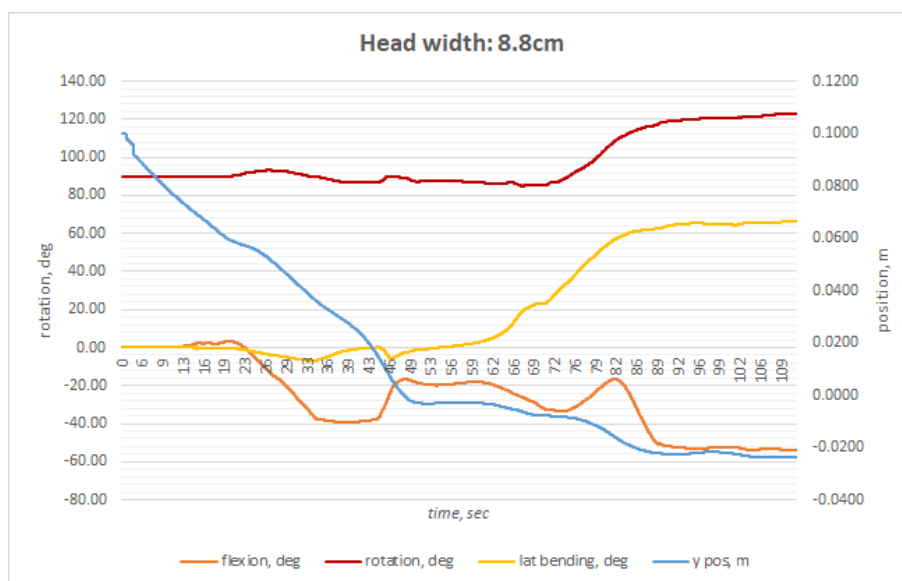


Figure 4.20: Graph of simulating a direct OP with NM01 neck model. The force, propagated through the neck, contributes towards flexion (descend of the orange curve), which leads to further descent until the head comes into contact with the pelvic floor muscles at around 47 second. At this point, the head is fully flexed (the peak for NM01 neck model is 40 degrees) and the occiput is in contact with the pelvic floor muscles. Unless the expulsion force is increased, the head will remain in this position. Further increase of expulsion force up to 80N, at around 88 seconds of the simulation, results in onset of internal rotation (red curve going up) of 30 degrees clockwise and results in extreme lateral bending (yellow curve going up).

pelvic floor muscles. At this point, the head is fully flexed and the occiput is in contact with the pelvic floor muscles. Once the expulsion force has reached 150N, this results in onset of internal rotation due to the shape of pelvic floor muscles and contact between the fetal trunk and sacrum (see Figure 4.22). However, maintaining the same amount of force results in extreme stretch of pelvic floor muscles and transverse arrest (see Figures 4.23, 4.24, 4.25). Maintaining the same expulsion force leads to delivery sideways.

In order to avoid the aforementioned overstretch the expulsion force had been manually controlled and heuristically decreased down to around 80-100N. Then the head continues internal rotation until it has reached 90 degrees, i.e. forehead

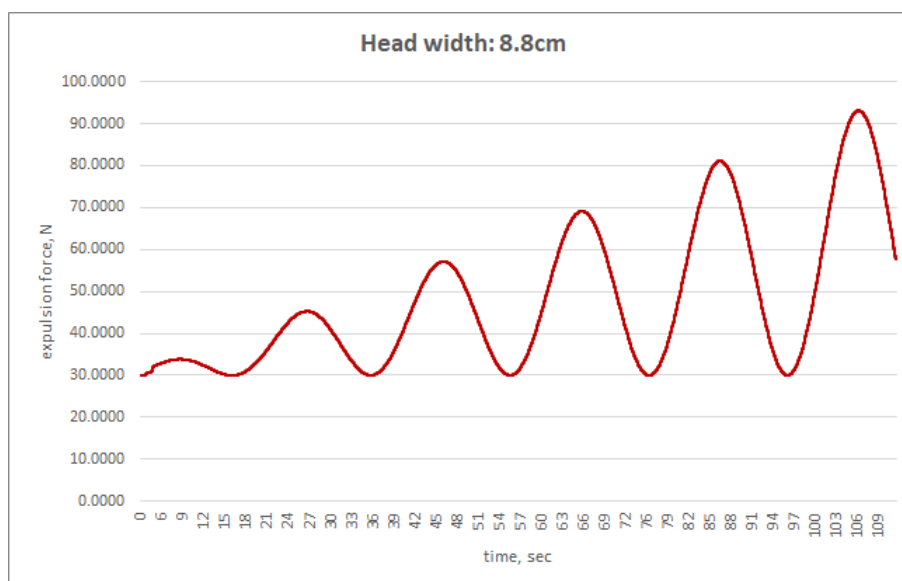


Figure 4.21: Graph of the increasing periodic expulsion force (red curve).

facing the back of the pelvis. Finally, once the head completed full rotation, the force needs to be increased up to around 180N in order for the delivery to occur (see Figures 4.26 and 4.27). This decreasing of expulsion force is in line with directions being given by midwives to the mother to push less, when a baby is in OP position (private communication, Kenda Crozier, Professor in Midwifery at UEA, 2018).

4.6.4 Pelvis tilted by 10 degrees

No particular improvements were observed in case when the pelvis was tilted anteriorly during the second stage of labour. In both cases the fetal head ends up completely flexed while in contact with pelvic floor muscles. However, with a tilted pelvis the simulation was noticeably faster. The head engaged quicker in case of the tilted pelvis and the rotation from OP to LOT (see Figure 1.7) occurred 90 seconds earlier. The latter may be due the manual adjustments of the expulsion force, which in turn introduced inconsistency in the applied force.

It is worth mentioning that with a tilted pelvis anteriorly by 10 degrees, the crown of the head enters the pelvis first simulating false flexion, although the

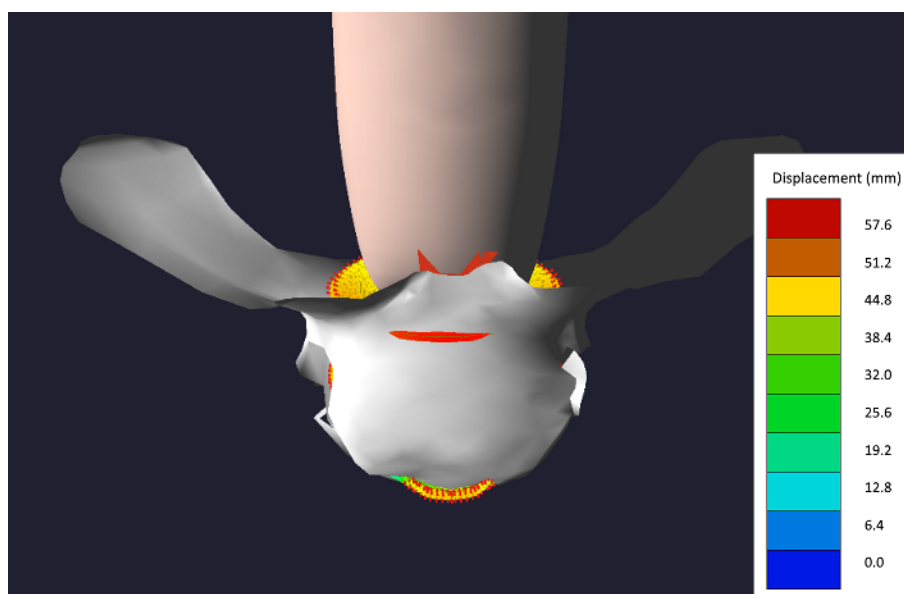


Figure 4.22: The trunk is in contact with sacrum and lower maternal spine (highlighted in red). The fetal trunk pushing against the maternal sacrum contributes to rotation of the fetal head in OP position.

head is deflexed. Having the pelvis rotated anteriorly even more would increase flexion of the head (see Figure 4.30).

Titling pelvis would arguably contribute toward faster dilation during the first stage of labour due to the crown of the head entering the pelvis inlet first when the pelvis is tilted anteriorly. This requires further investigation and development of a scene for simulating the first stage of labour.

It is difficult to comment on the observed movements of the fetus due to absence of variations in maternal pelvises and spines. In addition a number of maternal spine meshes would be required in order to simulate curled, straight and arched maternal spines. The curvature of the maternal spine can either cause the fetal head to flex or deflex and by doing so can either facilitate or hinder further descent of the fetus.

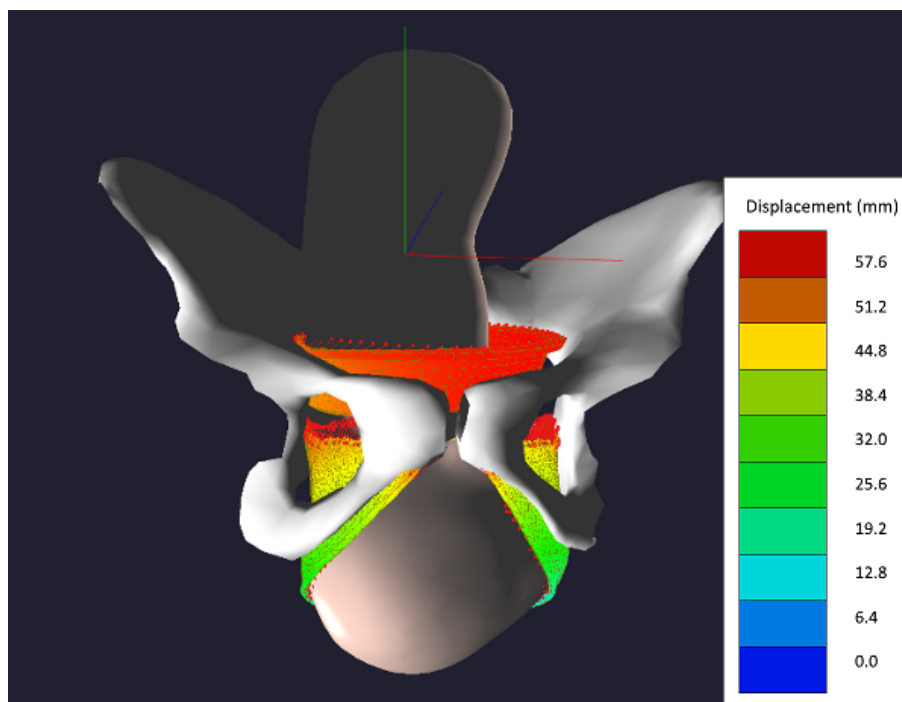


Figure 4.23: When a high expulsion force is exerted on the head during internal rotation in OP, the head overstretches the pelvic floor muscles. The displacements of the soft tissues (cervix, pelvic floor muscles and ligaments) are visualised through a colour legend.

4.7 Experimental study of cardinal movements with different dimensions of the fetal head

4.7.1 Introduction

In the following experiment we present the results of simulations in BirthView with various head widths of a fetus (biparietal diameters). First and foremost a cephalic index of the existing head was calculated in order to verify proportions of the head. Then the width was compared to the measurements presented in literature (Hall et al., 2006; Ismail et al., 2018). 18 experiments were conducted with various head widths in order to validate robustness of BirthView and the results are presented in plots.

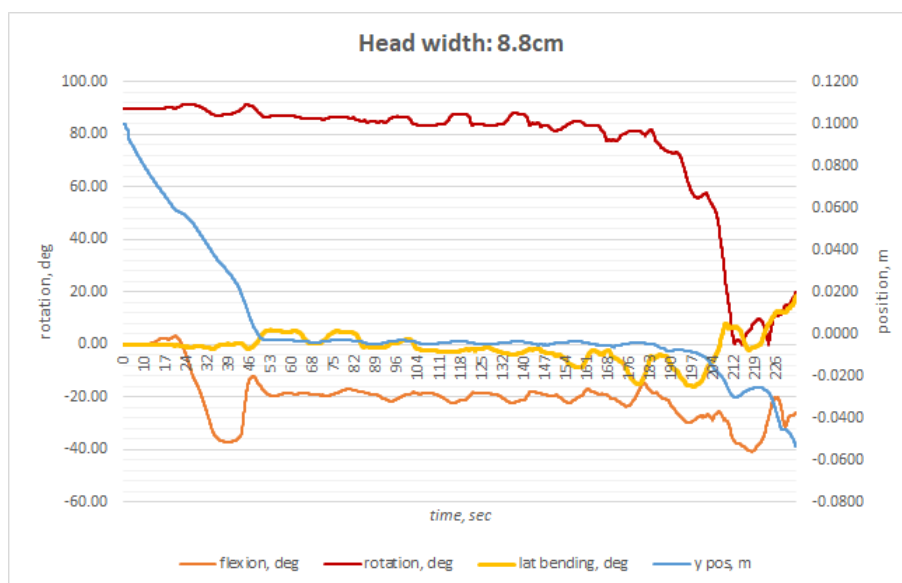


Figure 4.24: Graph of a non-controlled simulation of a direct OP with NM03 neck model.

4.7.2 Cephalic index

A cephalic index is the ratio of the maximum width of the head, multiplied by 100 divided by its maximum length. A cephalic index of a “normal” head of a child under three years old should fall between 74.39 and 81.45 percent (Likus et al., 2014).

$$CI = headwidth * 100 / headlength \quad (4.3)$$

The existing head in the simulation has a width of 8.3cm and a length of 11.83cm, including the mandible. However, in order to calculate a cephalic index, the length needs to be measured between the glabella¹ and the opisthocranium² (see Figure 4.31 and 4.32) (Hall et al., 2006). Hence, the length was measured to be 11.01cm (see Figure 4.33)).

¹Glabella - the most prominent point on the frontal bone above the root of the nose, between the eyebrows

²Opisthocranium - the most prominent portion of the occiput, close to the midline on the posterior rim of the foramen magnum

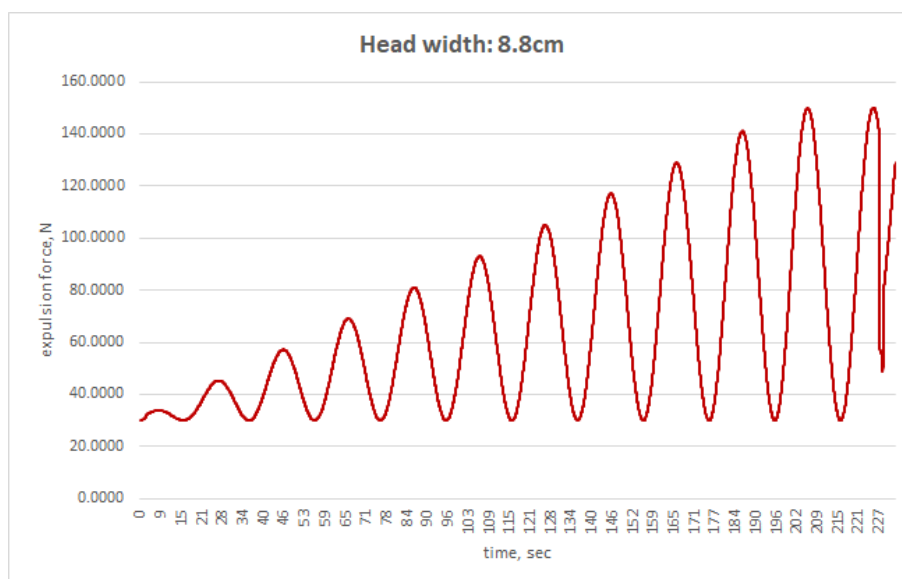


Figure 4.25: Graph of the non-controlled increase of periodic expulsion force (red curve).

Therefore, the cephalic index was calculated as follows:

$$CI = 8.3 * 100/11.03 = 75.38\% \quad (4.4)$$

The found CI is within the range of a “normal” head of a child under three years old (Likus et al., 2014).

4.7.3 Biparietal diameter (BPD)

Head width or biparietal diameter of the existing head is 8.3cm, excluding skin thickness, which has been approximated to be around 0.5mm from Lapeer (1999). Therefore, the width, including the skin, is around 8.8cm, which corresponds to the average head width at 36 weeks of gestational age and within 2 standard deviation of head width at 41 weeks of gestational age (Hall et al., 2006). In addition, Ismail et al. (2018) reported biparietal diameters in 551 neonates (right after birth), giving a mean value of 9.4cm (range 9.07 - 9.55cm) which is similar to the mean head width at 41 weeks (see Figure 4.34).

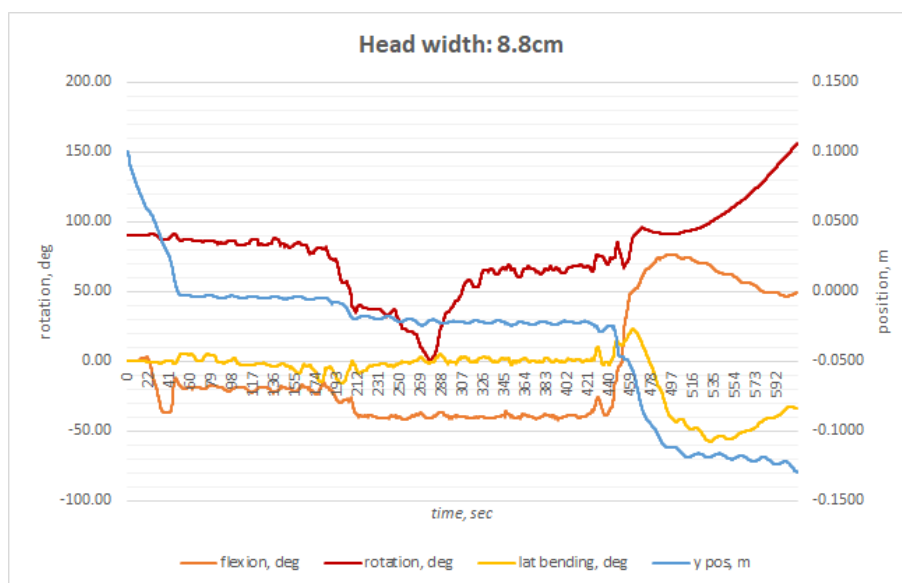


Figure 4.26: Graph of controlled simulation of a direct OP with NM03 neck model. Rotation (red curve) starts at 90 degrees from either LOT or ROT positions (see Figure 1.7) since the head is initially in OP position. Zero value corresponds to the head being in LOT position. Further increase up to 90 degrees correspond to “normal” internal rotation and the forehead of the fetal head being facing sacrum. Flexion (orange curve) occurs in the beginning when the head comes into contact with the pelvic inlet. It then decreases at around 41 seconds due to inability to descend further caused by the trunk being pushed forward by sacrum.

4.7.4 Experimental setup

Table 4.5 summarizes the experimental setup in BirthView.

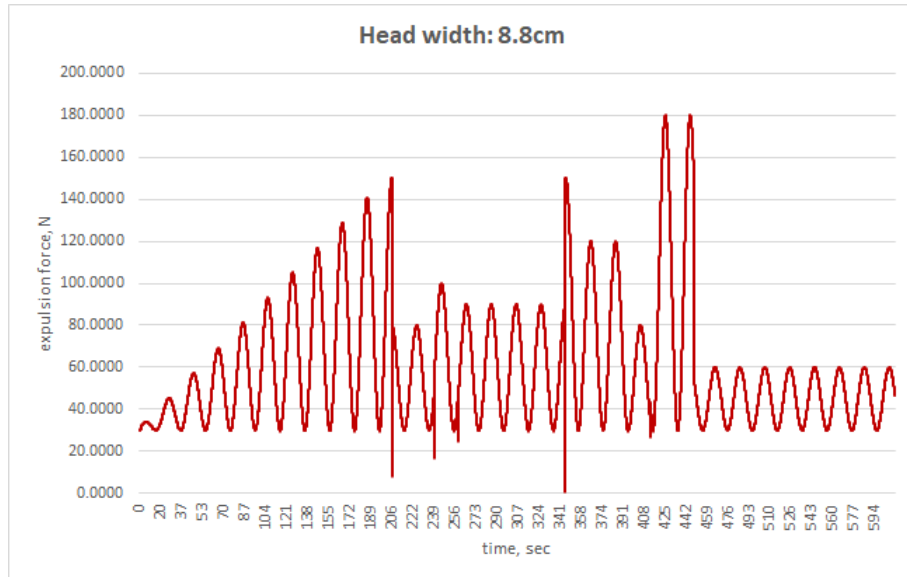


Figure 4.27: Graph of the controlled increase of periodic expulsion force (red curve). The spikes in the plot at 212, 250 and 345 seconds correspond to manual adjustments of the expulsion force.

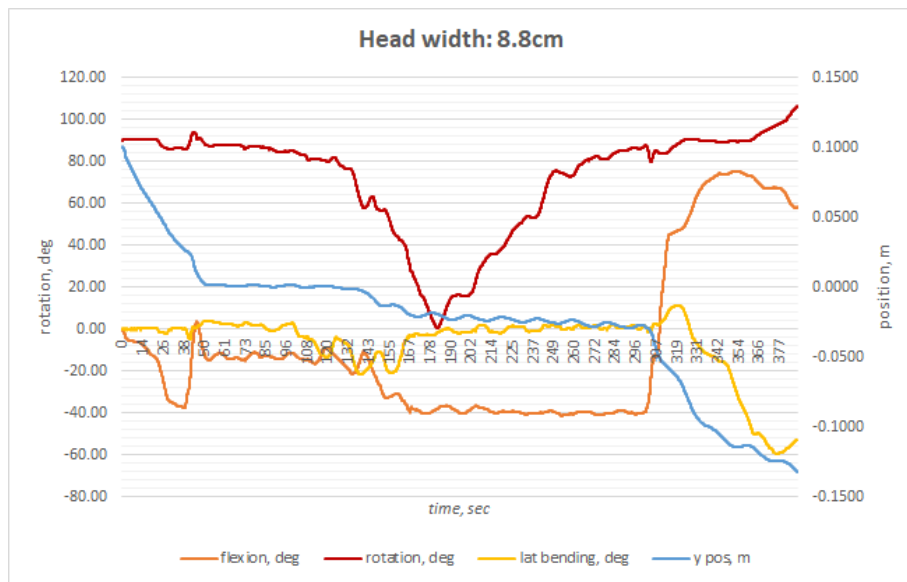


Figure 4.28: Graph of a non-controlled simulation of a direct OP with NM03 neck model.

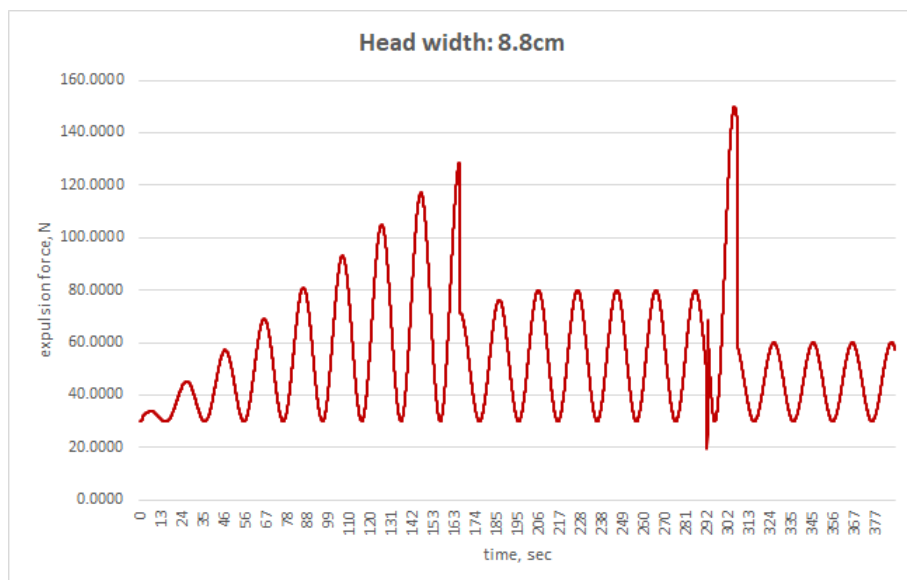


Figure 4.29: Graph of the non-controlled increase of periodic expulsion force (red curve).

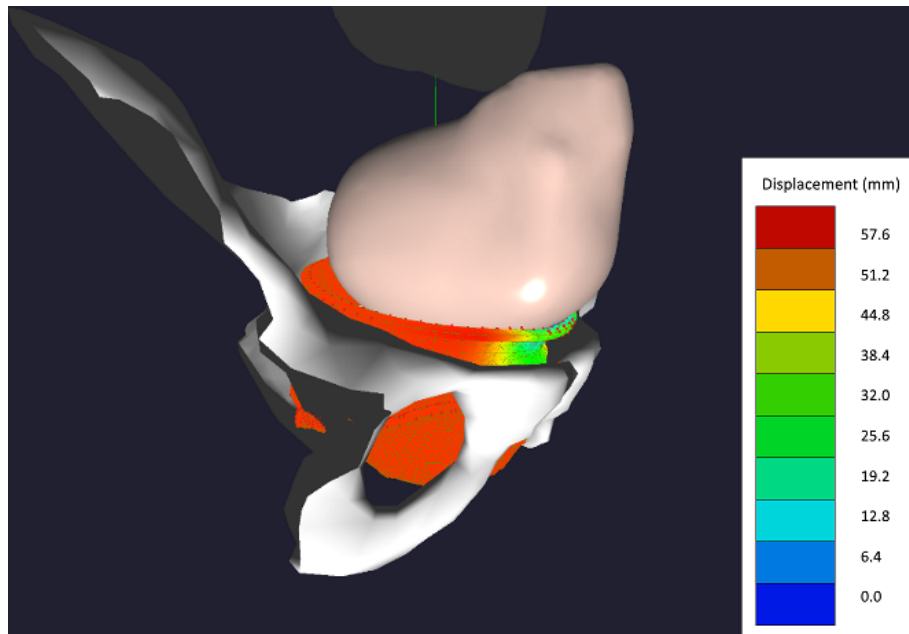


Figure 4.30: Picture of the simulation with a tilted pelvis anteriorly. It can be seen that with the tilted pelvis, the smaller diameter of the head enters the pelvis first. The displacements of the soft tissues (cervix, pelvic floor muscles and ligaments) are visualised through a colour legend.

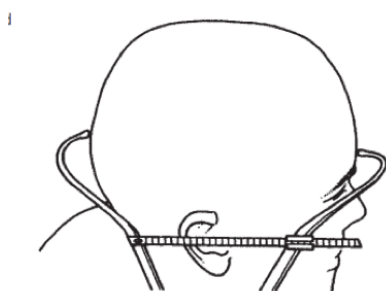


Figure 4.31: Measuring head length with calipers.

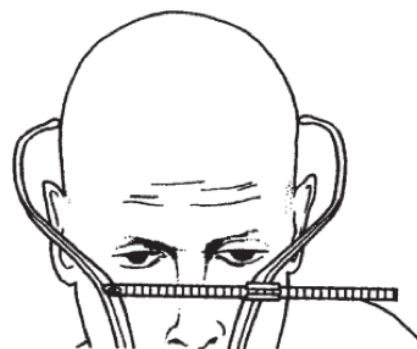


Figure 4.32: Measuring head width with calipers.

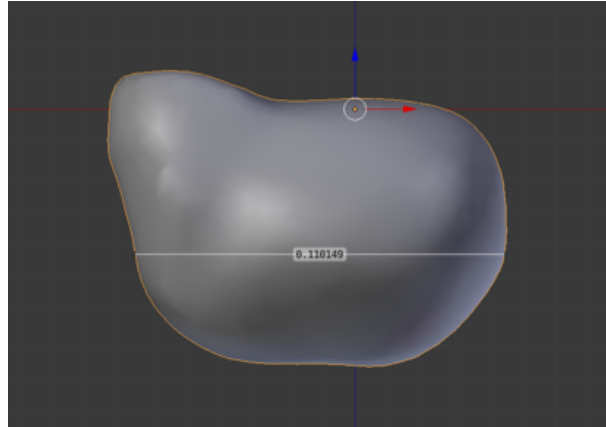


Figure 4.33: Measuring the fetal head's length in Blender with a ruler.

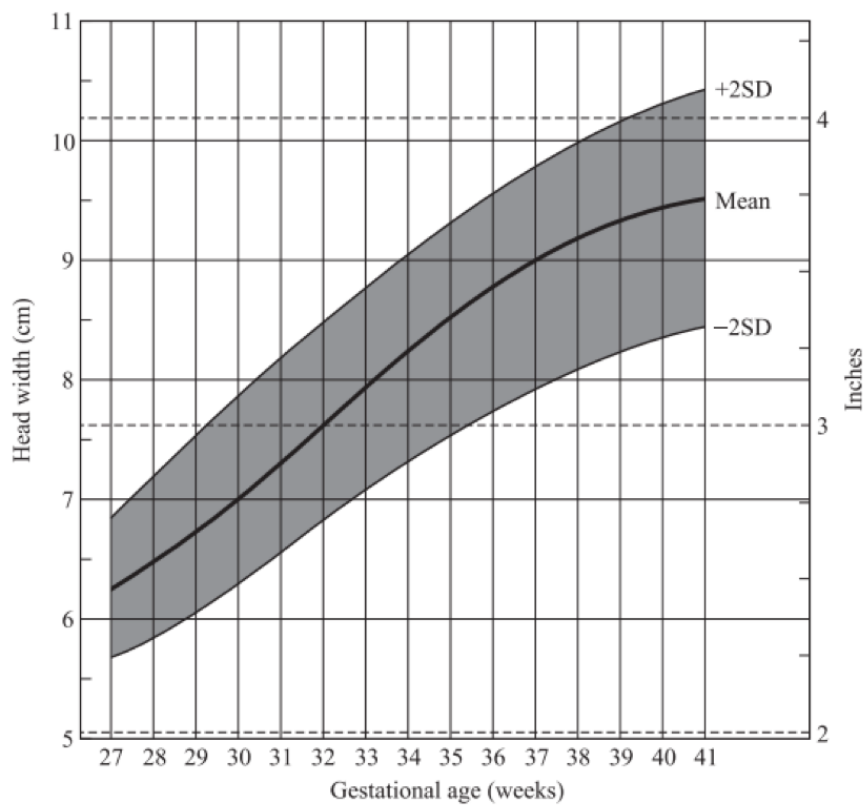


Figure 4.34: Head width, both sexes, at birth. From Merlob et al. (1984).

Table 4.5: The experimental setup of BirthView for the experimental study of cardinal movements with different dimension of the fetal head.

	<i>Lin damping</i>	<i>Rot damping</i>	<i>Mass</i>	<i>Positionx,y,z</i>	<i>Orientation</i>		
Fetal head	9650	3	1.5	[0.0133, 0.1, 0.0]	LOT*		
Fetal trunk	3650	3	2.5	[0.0133, 0.2151, 0.0]	LOT*		
Maternal pelvis	3650	1	1	[0.0, 0.0, 0.0]	n/a		
* LOT - left-occiput transverse position (see Figure 1.7)							
	<i>Length</i>	<i>Position on skull</i>	<i>Bushing element</i>				
			k_f	k_e	k_{lb}	k_t	k
Fetal neck	3.6	[0.0, 0.0, 0.0]*	0.01	0.04	2	0.1	3600
* <i>origin of the skull is at foramen magnum</i>							
k_f, k_e, k_{lb}, k_t - <i>stiffness coefficients in flexion, extension, lateral bending and rotation</i>							
k - <i>stiffness coefficient resisting elongation, compression and shear translations</i>							
	<i>Bulk modulus</i>	<i>Shear modulus</i>	<i>Number of elements</i>	<i>Number of nodes</i>			
PF muscles	1MPa	66kPa	18788	6577			

The fetus is in left-occiput transverse position (LOT). The fetal head position is at 0.0133 along x-axis, 0.1 along y-axis and 0.0 along z-axis.

Bulk and shear modulus for the pelvic floor muscles are equal to 1MPa and 66kPa respectively. Bony sacrospinous ligaments (rigid bodies) were used in order to speed up the simulation. The length of the neck is around 3.6cm.

Head width was scaled up from initial value of 8.8cm in steps of 0.5 up. The maximum head width in the table is within the range reported by Ismail et al. (2018).



Figure 4.35: Simulating childbirth (LOT) with a head width of 9.07cm. Bony pelvis, FE cervix, FE pelvic floor and bony sacrospinous ligaments are present. The head can be seen undergoing all cardinal movements. The flexion (descent of the orange curve) and the extension (the peak of the orange curve at around 288 sec) are shown. The internal rotation is shown gradually reaching the full value of around 90 degrees (red curve going up). The external rotation (red curve goes further up to 170 degrees) occurs after extension (peak on orange curve) and further descent of the head (blue curve going down).

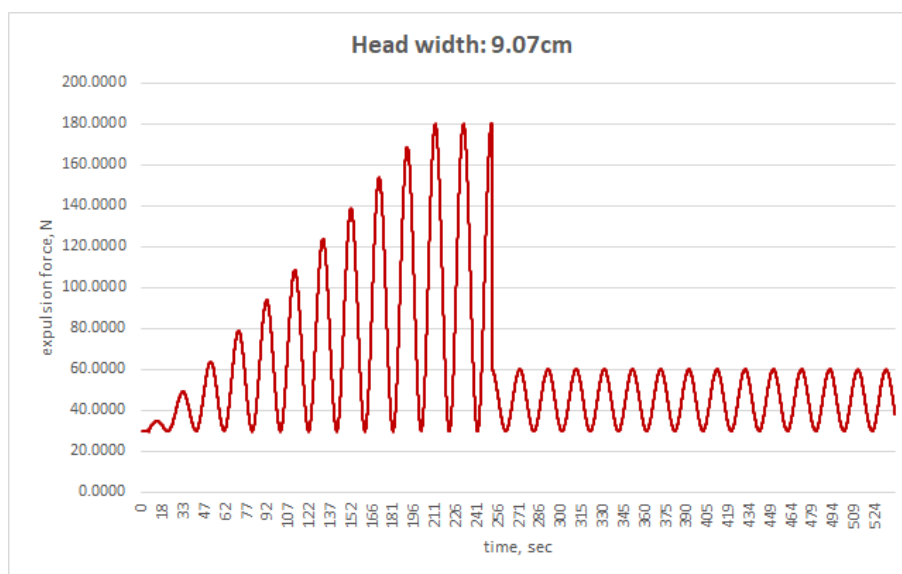


Figure 4.36: Graph of the increasing periodic expulsion force (red curve). The expulsion force is decreased after the delivery of the fetal head.

4.7.5 Analysis

From the plots (see Figures 4.35 and Appendix A) it can be seen that BirthView, with a new neck model (NM03), is capable of simulating childbirth for the whole range of the reported biparietal diameters. Larger heads require a higher amount of expulsion force in order for expulsion to occur (see Figure 4.37). Thus, a head with a width of 9.55cm requires around 220N of expulsion force. In addition, the minimum force required to deliver the smallest head (8.8cm) increased from 150N, reported by Gerikhanov (2017), to 180N (see Figure 4.36). This is due to the increased flexion, caused by the longer neck.

The external rotation occurred in the same direction (clockwise) as the internal rotation, when the fetus is initially in left-occiput transverse position. However, when the fetus is in right-occiput transverse position (see Figures 4.38 and 4.39), at the onset of the simulation, the internal rotation occurs in the opposite direction (anti-clockwise) (Gerikhanov, 2017), whereas the external rotation remains the same. This is caused by the asymmetrical shape of the pelvis and other factors such as one shoulder coming into contact with the pelvic floor

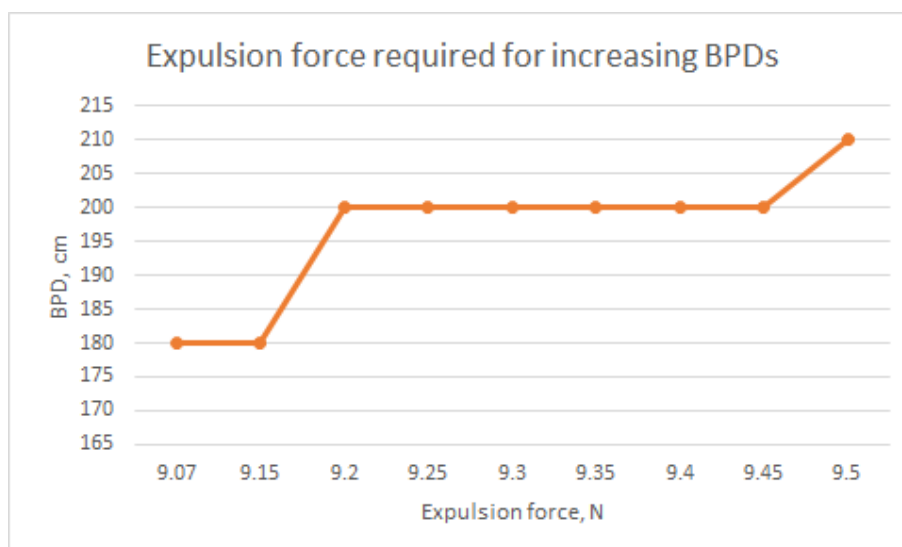


Figure 4.37: Graph of the expulsion force required for successful delivery of the fetal head with increasing BPDs.

muscles before the another. This has been experimentally verified in BirthView and the results have shown that more than one factor affects the direction of external rotation.

4.7.6 Additional experiments

4.7.6.1 Neck length of 2.4 cm

Same experiment as in Section 4.7.4 has been rerun this time with the shorter neck of, randomly selected, 2.4 cm (see Figure 4.41). The shorter neck corresponds to the lesser expulsion force of 150N required (see Figure 4.42) as compared to 180N for the longer neck (see Figure 4.36). Generally fetuses with shorter necks required less expulsion force for a successful delivery (see Figure 4.40). As can be seen in Figure 4.41 the shorter neck only flexed up to 30 degrees, whereas the longer neck flexed up until 40 degrees in Figure 4.35. The head can only deflex if there is sufficient space in the anterior part of the pelvic outlet for the fetal head to move away from the sacrum, otherwise further pushing contributes to higher flexion. With smaller flexion the head initially requires more space in the pelvic



Figure 4.38: Simulating childbirth (ROT) with a head width of 9.15cm. Bony pelvis, FE cervix, FE pelvic floor and bony sacrospinous ligaments are present. The head can be seen undergoing all cardinal movements. The flexion (descent of the orange curve) and the extension (the peak of the orange curve at around 308 sec) are shown. Rotation starts at 180 degrees since the fetus in ROT position. The internal rotation is shown gradually reaching the full value of around 90 degrees (red curve going down). The external rotation (red curve goes up to 180 degrees) occurs after extension (peak on orange curve) and further descent of the head (blue curve going down).

outlet and, hence, it is gradually stretching the pelvic floor muscles, to fit the pelvis, even before the completion of the internal rotation. That seems to be the reason the shorter neck takes longer to complete the internal rotation (compare Figures 4.35 and 4.41). As a result, with the shorter neck, the pelvic floor muscles need to stretch less in order for the extension to commence.

Another possibility, which requires further investigation is that a mobile sacrum contributes towards the deflexion of the fetal head by moving and rotating backwards.

In addition to the above experiments, the following experiments were con-

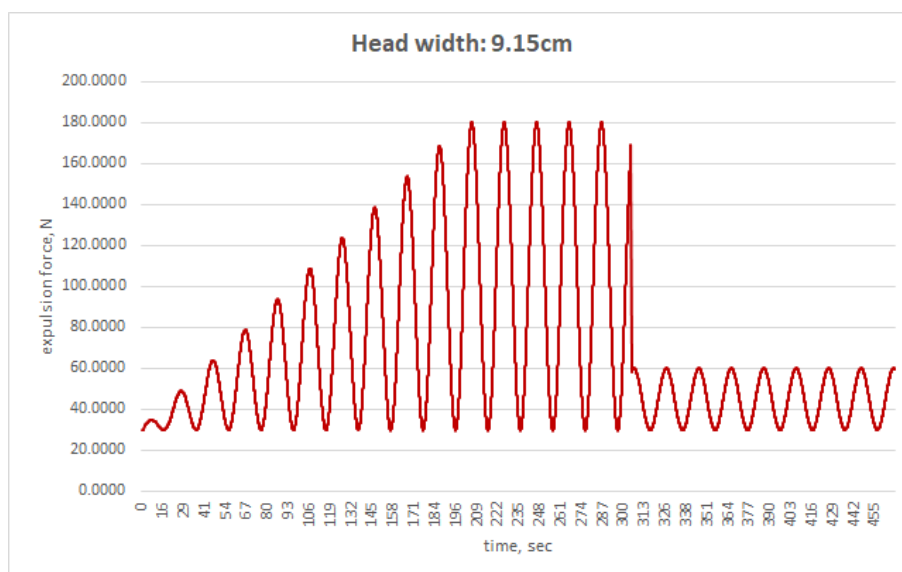


Figure 4.39: Graph of the increasing periodic expulsion force (red curve). The expulsion force is decreased after the delivery of the fetal head.

ducted:

- Fetus is in ROT position with the neck length of 3.6 cm.
- Variations in the neck length for LOT position: 1.2, 2.4, 3.6 and 4.2 cm.

4.7.7 Conclusion

It is important to note that the aforementioned experiments were not possible with the old neck model (NM01). That is due to inability of NM01 to resist lateral bending with a longer neck, whereas the new neck model (NM03) is using a 6DOF spring constraint to introduce a combined resistance of the neck in every direction, including the lateral bending. In addition, NM03 is using the mechanical properties acquired from the literature (Luck, 2012; Nuckley et al., 2013b).

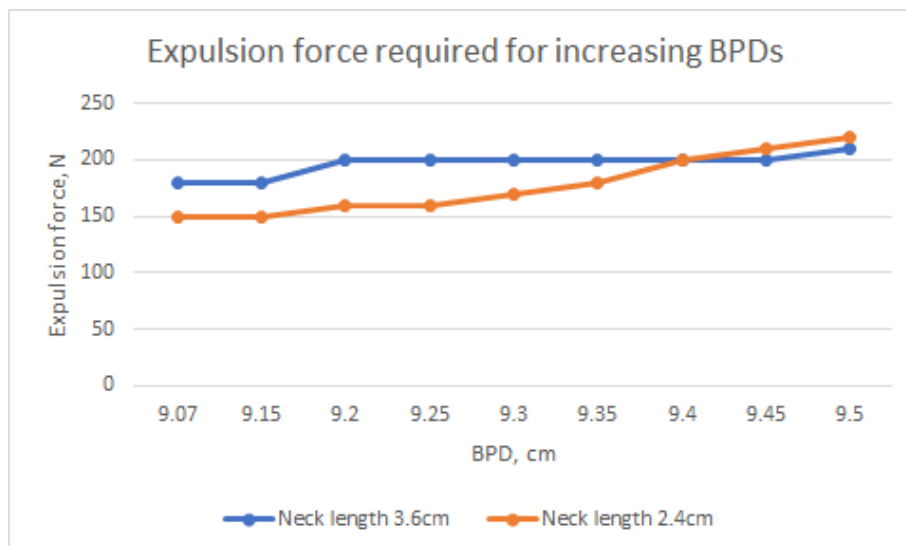


Figure 4.40: Comparison of the expulsion force required for successful delivery of the fetal head with increasing BPDs for the neck of length 2.4cm and 3.6cm.

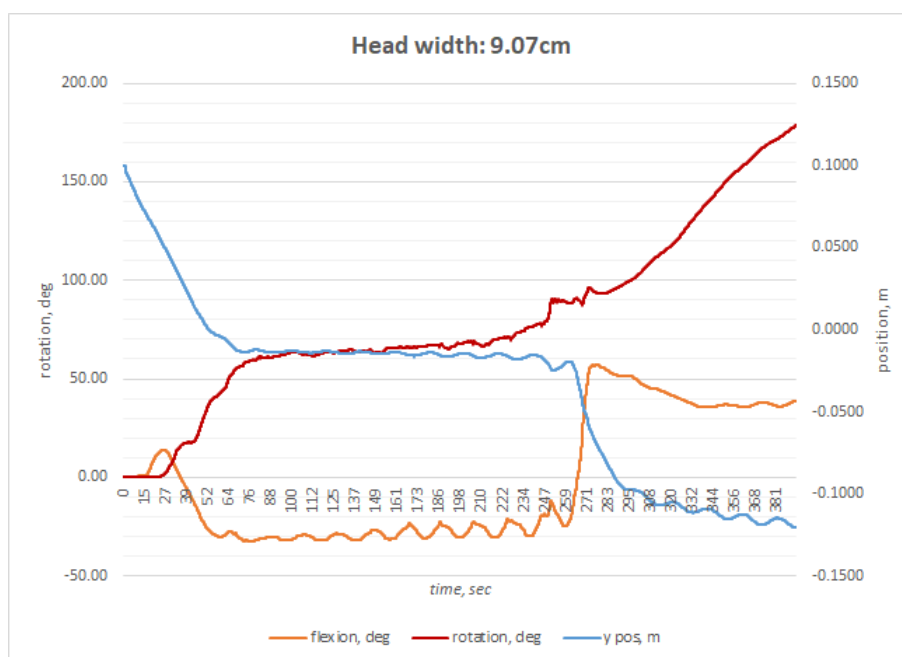


Figure 4.41: Simulating childbirth (LOT) with a head width of 9.07cm and neck length of 2.4cm. Bony pelvis, FE cervix, FE pelvic floor and bony sacrospinous ligaments are present. The head can be seen undergoing all cardinal movements. The flexion (descent of the orange curve) and the extension (the peak of the orange curve at around 275 sec) are shown. The internal rotation is shown gradually reaching the full value of around 90 degrees (red curve going up). The external rotation (red curve goes further up to 180 degrees) occurs after extension (peak on orange curve) and further descent of the head (blue curve going down).

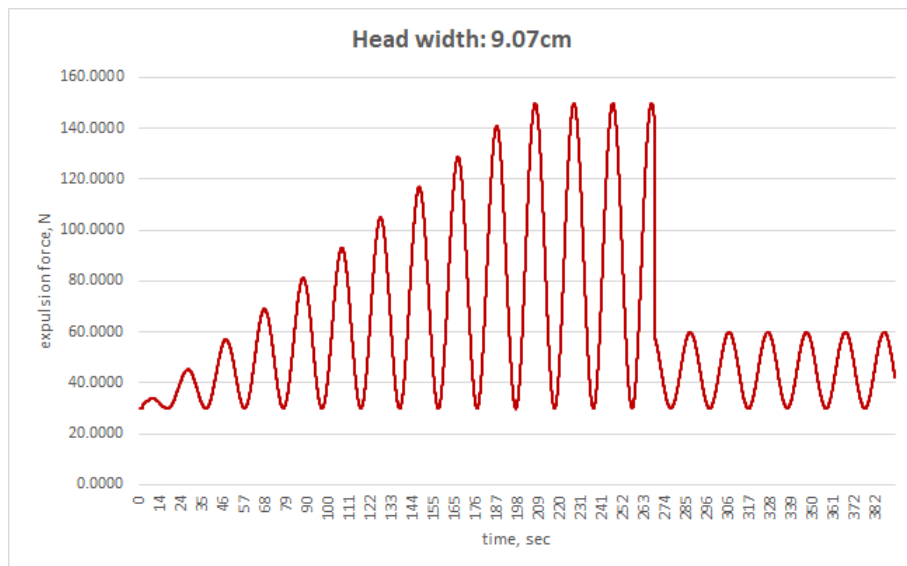


Figure 4.42: Neck length is 2.4cm. Graph of the increasing periodic expulsion force (red curve). The expulsion force is decreased after the delivery of the fetal head.

Chapter 5

Summary and Conclusions

5.1 Conclusion

In this project a childbirth simulation software BirthView has been validated and improved to eventually arrive at a patient-specific simulation. The existing neck model in the software was not capable of simulating cardinal movements with an average height of a cervical spine. Also the model used arbitrary stiffness values for the neck motion. The model was improved to incorporate a six degrees-of-freedom spring constraint to introduce resistance of the spine in various ranges of motion. In addition the new model is using approximated stiffness values from the existing pediatric and adult data. With the improved neck model, the software is capable of simulating childbirth with a bigger variety of the neck's mechanical properties such as the neck's length, separate stiffness values, i.e. resistance for stretch/compression, lateral bending, flexion, extension and rotation (see Appendix A). Hence, the null hypothesis (H0) was rejected and the alternative hypothesis (H1) was proven (see Section 1.5). The variations of the mechanical properties of a computer model of a fetal neck and its implementation can significantly affect the outcome of the virtual childbirth simulation.

Once the neck model was improved, a further validation of BirthView has been implemented for various biparietal diameters of fetal heads. Also a number of experiments were done on direct occipito-posterior position of a fetus to test a heuristic method of resolving direct OP position.

In addition, a simulation software BirthViewH was developed, which is using a haptic device to provide information on the effort needed to manipulate the fetal skull. This software can be improved and potentially used to estimate the combined stiffness of a newborn's head, including muscle resistance. The software has been clinically tested and the results are published in a conference paper (Sadulaev et al., 2017).

Another contribution of this research is validation of a projection based contact method with Total Lagrangian Explicit Dynamics in BirthView. The results have been published in the paper by Lapeer et al. (2019).

5.2 Summary

- A better neck model was developed as part of the childbirth simulator BirthView, which allowed for running the simulation with a higher variety of mechanical properties such as neck lengths and rotational stiffness parameters.
- An additional simulation software BirthViewH was developed to provide information on the effort needed to manipulate the fetal skull.
- A validation of the TLED method has been implemented.
- A number of experiments were performed for the validation of the neck and simulation software.
- A heuristic method of resolving direct occiput-posterior (OP) presentation was validated in BirthView. The results show that tilting a pelvis can potentially contribute towards faster labour especially during the first stage of labour and possibly contribute towards rotation of the fetal head in direct OP position.
- A new pelvis model was developed with a mobile sacrum. A number of experiments were conducted with both static and mobile sacrum. The results show that the mobile sacrum contributes towards complete internal rotation by increasing the pelvic outlet.

- Shoulder dystocia was simulated in BirthView.
- A device for measuring ROM of a fetal head and a protocol was developed, which can potentially be used in the future studies of newborns' neck properties

5.3 Limitations and Future work

5.3.1 Limitations

The implemented neck models and BirthViewH have a number of limitations mainly due to scarcity of available data and partially due to the implementation itself.

The list of limitations for the neck model:

- The combined stiffness values, incorporated into the neck models, are only approximations and ideally should include the effects of passive resistance of the neck muscles.
- The implemented bushing element may lose one of the rotational axes (Gimbal lock), when an object is rotated at 90 degrees. The problem can be addressed by using quaternions (Diebel, 2006), however, they were not required at this stage to achieve the aim and objectives of the project.
- Measuring ROM from the video with a perspective distortion will affect the accuracy of the measurement.
- The implemented neck model (NM03) is not capable of simulating the coupled motion of the neck, i.e. when the head is either completely rotated sideways or flexed, the ROM of lateral bending is supposed to decrease. Similarly when the head is in complete lateral bending, the ROM in flexion and side rotation decreases.

The list of limitations for BirthViewH:

- Lateral bending and separate flexion from extension needs to be implemented in the software.

- The spherical proxies should be replaced by animated hands which can grasp the fetal head for more realistic manipulations. Currently, the spherical proxies occasionally slip off the virtual head in particular with users who are not familiar with using a haptics UI.
- A stylus based interface of the haptic device (Phantom Omni) should also be extended to have a shape of a hand to make the experience of holding a baby, in the virtual environment, more realistic. Such a hand stylus could be made using a 3D printer.
- Another important limitation of the BirthViewH is the maximum force range of the used haptic devices which is around 3.3 N (see Figure 3.4). Depending on whether the baby is being held or is lying on the bed in the software, the maximum force may not be enough to simulate the resistance of a fetal head. To simulate the gravity of a baby being held in an experimenter's arms, the haptic device should be able to exert force of at least 4.9 N given a head mass of 0.5 kg.
- The current haptic devices only provides 3DoF haptic feedback, however, when holding and turning a baby's head a 6DoF haptic feedback would be more appropriate to realistically simulate the resistance of the head.
- More realistic 3D meshes of a newborn's head (rather than a skull model) and a trunk with shoulders and articulated arms. The legs are not important in this particular simulation.
- The effect of gravity needs to be improved on as we did not have exact data of the centre of gravity of the fetal/newborn head at the time we conducted the first series of the experiments.

5.3.2 Future work

5.3.2.1 Neck model

Currently the coupled motion of the neck is simulated by adjusting the stiffness values at runtime and it seems to be the only way with the existing neck

model. The next logical step in improving the neck model would be identifying the strength or resistance of the fetal neck as a whole, including the surrounding muscles and incorporating the found values in the neck model. The provided protocol for a clinical study of ROM in healthy newborn babies (see Appendix B), with a few adjustments, could be potentially used to acquire the required data.

In addition it is essential to have the ROM and stiffness data on combined flexion-rotation, flexion-lateral bending, rotation-lateral bending and flexion-rotation-lateral bending of the fetal head to accommodate for all possible scenarios. These tests need to be included in the above protocol.

5.3.2.2 First stage of labour

Is it important to be able to simulate the first stage of labour to observe various complicated birth scenarios such as direct OP position. Currently the cervix in BirthView is always fully dilated and, therefore, it is impossible to make conclusions on whether certain heuristic techniques for resolving direct OP would be helpful.

5.3.2.3 Additional meshes for maternal spines

The curvature of maternal spines (arched, curled and straight) is believed to have an effect on the childbirth during the first stage of labour. The arched maternal spine can cause the fetal head to flex and, by doing so, facilitate presentation of the narrower diameter of the head during the first stage of labour.

5.3.2.4 Additional meshes for fetal skulls and trunks

In order to complete the validation of BirthView additional meshes for fetal skulls and trunks are required. This would involve either gathering CT data of newborns or adjusting the existing meshes to correspond to the reported dimensions in the literature.

5.3.2.5 Complete birth canal

A complete birth canal is necessary to direct the fetal body to a successful delivery. The complete birth canal is especially important once a flexible fetal torso is introduced in BirthView. In addition, the birth canal could potentially contribute to resisting extreme lateral flexion of the fetal head in the simulation.

5.3.2.6 Flexible fetal torso and articulated shoulders

It has been shown experimentally that a flexible torso is essential for the last cardinal movement, expulsion, to occur since otherwise the torso would not progress further into the birth canal (see Section 4.3.3). Articulated shoulders are essential in order to simulate various scenarios of shoulder dystocia and their resolution.

Bibliography

- Autodesk Maya (2019). Bullet Constraint Types.
<https://knowledge.autodesk.com/support/maya/learn-explore/caas/CloudHelp/cloudhelp/2019/ENU/Maya-SimulationEffects/files/GUID-CDB3638D-23AF-49EF-8EF6-53081EE4D39D-htm.html>
Website accessed 3rd July, 2019. vi, 64
- Bamberg, C., Rademacher, G., Güttler, F., Teichgräber, U., Cremer, M., Bühner, C., Spies, C., Hinkson, L., Henrich, W., Kalache, K. D., et al. (2012). Human birth observed in real-time open magnetic resonance imaging. *American journal of obstetrics and gynecology*, 206(6):505–e1. vii, 4, 106, 108, 109
- Belytschko, T., Andriacchi, T., Schultz, A., and Galante, J. (1973). Analog studies of forces in the human spine: computational techniques. *Journal of Biomechanics*, 6(4):361–371. 26
- Benrubi, G. I. (2010). *Handbook of obstetric and gynecologic emergencies*. Lippincott Williams & Wilkins. 110
- Biancuzzo, M. (1993). How to recognize and rotate an occiput posterior fetus. *The American journal of nursing*, 93(3):38–41. 122
- Bogduk, N. and Mercer, S. (2000). Biomechanics of the cervical spine. i: Normal kinematics. *Clinical biomechanics*, 15(9):633–648. 45
- Bondy, M., Altenhof, W., Chen, X., Snowdon, A., and Vrkljan, B. (2014). Development of a finite element/multi-body model of a newborn infant for restraint analysis and design. *Computer methods in biomechanics and biomedical engineering*, 17(2):149–162. 37, 38, 39, 40, 64, 179

- Borell, U. and Fernström, I. (1957a). The movements in the mechanism of disengagement with special reference to the attitude of the foetal head. *Acta obstetricia et gynecologica Scandinavica*, 36(3):347–355. 3, 4
- Borell, U. and Fernström, I. (1957b). Shape and course of the birth canal a radiographic study in the human. *Acta obstetricia et gynecologica Scandinavica*, 36(2):166–178. 3
- Borell, U. and Fernström, I. (1958). Radiographic studies of the rotation of the foetal shoulders during labour. *Acta obstetricia et gynecologica Scandinavica*, 37(1):54–61. v, 3, 4, 9, 10, 11, 18
- Borell, U. and Fernström, I. (1959). Internal anterior rotation of the foetal head a contribution to its explanation. *Acta obstetricia et gynecologica Scandinavica*, 38(1):103–108. 3
- Bosio, A. C. and Bowman, B. M. (1986). Simulation of head-neck dynamic response in- gx and+ gy. Technical report, SAE Technical Paper. 25
- Caldwell, W. E. and Moloy, H. C. (1938). Anatomical Variations in the Female Pelvis: Their Classification and Obstetrical Significance: (Section of Obstetrics and Gynaecology). *Proceedings of the Royal Society of Medicine*, 32(1):1–30. v, 13, 21
- Chamberlain, G. V. P. (1995). *Obstetrics by Ten Teachers*. Oxford University Press, Inc. 2, 4, 6, 8, 11
- Chancey, V. C., Nightingale, R. W., Van Ee, C. A., Knaub, K. E., and Myers, B. S. (2003). Improved estimation of human neck tensile tolerance: reducing the range of reported tolerance using anthropometrically correct muscles and optimized physiologic initial conditions. *Stapp Car Crash Journal*, 47:135. 29
- Chappuis, D. (2013). Constraints derivation for rigid body simulation in 3D. <https://www.danielchappuis.ch/download/ConstraintsDerivationRigidBody3D.pdf>
Website accessed 11th September, 2019. 69

- Ching, R. P., Nuckley, D. J., Hertsted, S. M., Eck, M. P., Mann, F. A., and Sun, E. A. (2001). Tensile mechanics of the developing cervical spine. *Stapp car crash journal*, 45:329–336. [28](#)
- Coats, B. and Margulies, S. S. (2008). Potential for head injuries in infants from low-height falls: Laboratory investigation. *Journal of neurosurgery: pediatrics*, 2(5):321–330. [28](#), [38](#), [57](#)
- Cramer, H., Liu, Y. K., and Von Rosenberg, D. (1976). A distributed parameter model of the inertially loaded human spine. *Journal of biomechanics*, 9(3):115–130. [25](#)
- Crelin, E. S. (1969). *Anatomy of the Newborn*. Lea & Febiger. [v](#), [19](#), [20](#)
- Crelin, E. S. (1973). *Functional Anatomy of the Newborn*. Yale University Press. [12](#)
- De Jager, M., Sauren, A., Thunnissen, J., and Wismans, J. (1994). A three-dimensional head-neck model: Validation for frontal and lateral impacts. *SAE transactions*, pages 1660–1676. [26](#), [27](#)
- Deng, Y.-C. and Goldsmith, W. (1987). Response of a human head/neck/upper-torso replica to dynamic loading—i. physical model. *Journal of biomechanics*, 20(5):471–486. [26](#)
- Diebel, J. (2006). Representing attitude: Euler angles, unit quaternions, and rotation vectors. *Matrix*, 58:15–16. [69](#), [145](#)
- Dietze, M. (2001). A re-evaluation of the mechanism of labour for contemporary midwifery practice. *Midwifery Matters*, 88:3–8. [2](#), [3](#), [7](#), [9](#), [85](#)
- Drake, R. L., Vogl, W., Mitchell, A. W. M., Tibbitts, R., Richardson, P., and Horn, A. (2015). *Gray's anatomy for students*. Philadelphia, PA : Churchill Livingstone/Elsevier, [2015]. [v](#), [21](#), [198](#), [199](#), [200](#), [201](#), [202](#), [203](#), [204](#)
- Duncan, J. M. (1874). Laboratory note: on the tensile strength of the fresh adult foetus. *British medical journal*, 2(729):763. [29](#), [94](#)

- Esat, V. and Acar, M. (2007). A multi-body model of the whole human spine for whiplash investigation. *Journal of Biomechanics*, pages 1–7. [64](#)
- Ewing, C., Thomas, D., Lustik, L., Muzzy, W., Willems, G., and Majewski, P. (1977). Dynamic response of the human head and neck to + gy impact acceleration. Technical report, SAE Technical Paper. [25](#)
- Exponent (2019). Sled Test Development.
<https://www.exponent.com/experience/sled-test-development/>
Website accessed 14th September, 2019. [25](#)
- First Technology Safety Systems (2008). Q0 user manual. [37](#), [42](#)
- Gabbe, S., Niebyl, J., Galan, H., Jauniaux, E., Landon, M., Simpson, J., and Driscoll, D. (2012). *Obstetrics: Normal and Problem Pregnancies, 6th Edition*. Saunders Elsevier. [8](#), [10](#), [11](#)
- Garland, M. and Heckbert, P. S. (1997). Surface simplification using quadric error metrics. In *Proceedings of the 24th annual conference on Computer graphics and interactive techniques*, pages 209–216. [99](#)
- Gerikhanov, Z. (2017). *Simulating the cardinal movements of childbirth using finite element analysis on the graphics processing unit*. PhD thesis, University of East Anglia. [2](#), [86](#), [89](#), [110](#), [112](#), [116](#), [136](#)
- Gerikhanov, Z., Audinis, V., and , R. (2013). Towards a forward engineered simulation of the cardinal movements of human childbirth. In *E-Health and Bioengineering Conference (EHB)*. [24](#)
- Goode, A., Hegedus, E. J., Sizer, P., Brismee, J.-M., Linberg, A., and Cook, C. E. (2008). Three-dimensional movements of the sacroiliac joint: a systematic review of the literature and assessment of clinical utility. *Journal of Manual & Manipulative Therapy*, 16(1):25–38. [13](#)
- Hall, J., Allanson, J., Gripp, K., and Slavotinek, A. (2006). *Handbook of physical measurements*. Oxford University Press. [126](#), [127](#), [128](#)

- Heitjan, D. F. and Little, R. J. (1991). Multiple imputation for the fatal accident reporting system. *Journal of the Royal Statistical Society: Series C (Applied Statistics)*, 40(1):13–29. 45
- Hietanen, M. and Alanko, T. (2005). Occupational exposure related to radiofrequency fields from wireless communication systems. *Online]. <http://www.ursi.org/Proceedings/ProcGA05/pdf K, 3>*. 182
- Hill, A. (1938). The heat of shortening and the dynamic constants of muscle. *Proceedings of the Royal Society of London B: Biological Sciences*, 126(843):136–195. 27
- Hoag, D. (1963). Apollo guidance and navigation considerations of apollo imu gimbal lock. *Canbridge: MIT Instrumentation Laboratory*, pages 1–64. 68
- Hoyte, L., Damaser, M. S., Warfield, S. K., Chukkapalli, G., Majumdar, A., Choi, D. J., Trivedi, A., and Krysl, P. (2008). Quantity and distribution of levator ani stretch during simulated vaginal childbirth. *American journal of obstetrics and gynecology*, 199(2):198–e1. 23
- Humanetics ATD (2017). Available Models.
<http://www.humaneticsatd.com/virtual-models/finite-element/available-models>
Website accessed 15th January, 2017. 37
- Huston, J., Passerello, C., and Huston, R. (1976). Numerical prediction of head/neck response to shock-impact. Technical report, Cincinnati Univ Ohio Dept of Engineering Analysis. 25
- Huynh, K. T., Gibson, I., and Gao, Z. (2012). Development of a detailed human spine model with haptic interface. In *Haptics Rendering and Applications*, pages 179–180. IntechOpen. 64
- Ismail, A.-Q. T., Yates, D., Chester, J., and Ismail, K. M. (2018). Exploring the newborn head diameters in relation to current obstetric forceps’ dimensions: A systematic review. *European Journal of Obstetrics & Gynecology and Reproductive Biology*, 220:25–29. 126, 128, 135

- Jalalian, A., Gibson, I., and Tay, E. H. (2013). Computational biomechanical modeling of scoliotic spine: Challenges and opportunities. *Spine Deformity*, 1(6):401–411. 24
- Janssen, P. A., Thiessen, P., Klein, M. C., Whitfield, M., MacNab, Y. C., and Cullis-Kuhl, S. (2007). Standards for the measurement of birth weight, length and head circumference at term in neonates of european, chinese and south asian ancestry. *Open Medicine*, 1(2):74–88. 40
- Jing, D., Ashton-Miller, J. A., and DeLancey, J. O. (2012). A subject-specific anisotropic visco-hyperelastic finite element model of female pelvic floor stress and strain during the second stage of labor. *Journal of biomechanics*, 45(3):455–460. v, 3
- Jones, M., Holt, C., and Franyuti, D. (2008). Developing a methodology for the analysis of infant spine kinematics for the investigation of the shaken baby syndrome. *Journal of Biomechanics*, 41:S3–55. 39
- Jones, M. D., Martin, P. S., Williams, J. M., Kemp, A. M., and Theobald, P. (2015). Development of a computational biomechanical infant model for the investigation of infant head injury by shaking. *Medicine, Science and the Law*, 55(4):291–299. 179
- Kastler, B., Gangi, A., Mathelin, C., Germain, P., Arhan, J.-M., Treisser, A., Dietemann, J. L., and Wackenheim, A. (1993). Fetal shoulder measurements with mri. *Journal of computer assisted tomography*, 17(5):777–780. 109
- Kinovea (2016). FEATURES.
<https://www.kinovea.org/features.html>
Website accessed 15th April, 2019. 77, 78, 79
- Lapeer, R., Audinis, V., Gerikhanov, Z., and Dupuis, O. (2014). A computer-based simulation of obstetric forceps placement. In *International Conference on Medical Image Computing and Computer-Assisted Intervention*, pages 57–64. Springer. 1, 194

- Lapeer, R., Gerikhanov, Z., Sadulaev, S.-M., Audinis, V., Rowland, R., Crozier, K., and Morris, E. (2019). A computer-based simulation of childbirth using the partial dirichlet–neumann contact method with total lagrangian explicit dynamics on the gpu. *Biomechanics and modeling in mechanobiology*, 18(3):681–700. [v](#), [2](#), [4](#), [16](#), [24](#), [86](#), [112](#), [144](#)
- Lapeer, R. and Prager, R. (2001). Fetal head moulding: finite element analysis of a fetal skull subjected to uterine pressures during the first stage of labour. *Journal of Biomechanics*, 34(9):1125–1133. [5](#), [23](#), [59](#)
- Lapeer, R. J. A. (1999). *A biomechanical model of foetal head moulding*. PhD thesis, University of Cambridge. [128](#)
- Lee, S.-H. and Terzopoulos, D. (2006). Heads up!: biomechanical modeling and neuromuscular control of the neck. *ACM Trans. Graph.*, 25(3):1188–1198. [27](#)
- Li, X., Kruger, J. A., Chung, J.-H., Nash, M. P., and Nielsen, P. M. (2008). Modelling childbirth: comparing athlete and non-athlete pelvic floor mechanics. In *International Conference on Medical Image Computing and Computer-Assisted Intervention*, pages 750–757. Springer. [23](#)
- Li, X., Kruger, J. A., Nash, M. P., and Nielsen, P. M. (2010). Modeling childbirth: elucidating the mechanisms of labor. *Wiley Interdisciplinary Reviews: Systems Biology and Medicine*, 2(4):460–470. [23](#)
- Lien, K.-C., Mooney, B., DeLancey, J. O., and Ashton-Miller, J. A. (2004). Levator ani muscle stretch induced by simulated vaginal birth. *Obstetrics and gynecology*, 103(1):31. [24](#)
- Likus, W., Bajor, G., Gruszczyńska, K., Baron, J., Markowski, J., Machnikowska-Sokołowska, M., Milka, D., and Lepich, T. (2014). Cephalic index in the first three years of life: study of children with normal brain development based on computed tomography. *The Scientific World Journal*, 2014. Article ID: 502836. [127](#), [128](#)
- Lopik, D. v. (2004). *A computational model of the human head and cervical spine for dynamic impact simulation*. PhD thesis, © David van Lopik. [25](#), [26](#)

- Luck, J. F. (2012). *The Biomechanics of the Perinatal, Neonatal and Pediatric Cervical Spine: Investigation of the Tensile, Bending and Viscoelastic Response*. PhD thesis, Duke University. ii, vi, xi, 28, 30, 31, 32, 33, 40, 41, 44, 45, 46, 47, 57, 58, 59, 63, 87, 92, 139, 180
- Luck, J. F., Nightingale, R. W., Cameron, R., and Bass, D. (2013). Compressive mechanical properties of the perinatal, neonatal and pediatric cervical spine. In *2013 IRCOBI Conference Proceedings - International Research Council on the Biomechanics of Injury*, page 655. xi, 31, 32, 33
- Luck, J. F., Nightingale, R. W., Loyd, A. M., Prange, M. T., Dibb, A. T., Song, Y., Fronheiser, L., and Myers, B. S. (2008). Tensile mechanical properties of the perinatal and pediatric pmhs osteoligamentous cervical spine. *Stapp car crash journal*, 52:107. ii, vi, xi, xii, 28, 29, 31, 32, 33, 38, 57, 58, 59, 89, 92, 94
- Luo, Z., Pronost, N., and Egges, A. (2013). Physics-based human neck simulation. In Bender, J., Dequidt, J., Duriez, C., and Zachmann, G., editors, *VRIPHYS*, pages 51–60. Eurographics Association. 27
- Maigne, J.-Y. (2002). Management of common coccygodynia. *Angers: Sociedad Francesa de Medicina Manual Osteopática y Ortopédica [Internet]*.
https://www.coccyx.org/medabs/Maigne%20Jean-Yves_Management%20of%20Common%20Coccygodynia.pdf. 14
- Maigne, J.-Y., Guedj, S., and Straus, C. (1994). Idiopathic coccygodynia. lateral roentgenograms in the sitting position and coccygeal discography. *Spine*, 19(8):930–934. 14
- Martin, A. (2007). Entity Systems are the future of MMOG development, Online Article 2007.
<http://t-machine.org/index.php/2007/09/03/entity-systems-are-the-future-of-mmog-development-part-1/>. 24, 195
- Merlob, P., Sivan, Y., and Reisner, S. H. (1984). Anthropometric measurements of the newborn infant (27 to 41 gestational weeks). *Birth defects original article series*, 20(7):1–52. 133

- Mertz, H. J. and Patrick, L. M. (1971). Strength and response of the human neck. Technical report, SAE Technical Paper. [37](#)
- Moreau, R., Pham, M. T., Redarce, T., and Dupuis, O. (2008). Simulation of forceps extraction on a childbirth simulator. In *Robotics and Automation, 2008. ICRA 2008. IEEE International Conference on*, pages 1100–1105. IEEE. [85](#)
- Norkin, C. C. and White, D. J. (2016). *Measurement of joint motion: a guide to goniometry*. Philadelphia, PA, F A Davis Co. [72](#), [73](#), [74](#), [75](#), [76](#), [77](#)
- Nuckley, D. J. and Ching, R. P. (2006). Developmental biomechanics of the cervical spine: tension and compression. *Journal of biomechanics*, 39(16):3045–3054. [28](#)
- Nuckley, D. J., Linders, D. R., and Ching, R. P. (2013a). Developmental biomechanics of the human cervical spine. *Journal of Biomechanics*, 46(6):1147–1154. [ii](#), [28](#), [30](#), [44](#), [45](#), [46](#), [57](#), [58](#)
- Nuckley, D. J., Linders, D. R., and Ching, R. P. (2013b). Developmental biomechanics of the human cervical spine. *Journal of biomechanics*, 46(6):1147–1154. [xi](#), [34](#), [35](#), [36](#), [44](#), [139](#)
- Ohlsén, H. (1973). Moulding of the pelvis during labour. *Acta Radiologica Diagnosis (Sweden)*, 14(4):417–434. [3](#)
- Öhman, A. M. and Beckung, E. R. (2008). Reference values for range of motion and muscle function of the neck in infants. *Pediatric Physical Therapy*, 20(1):53–58. [40](#), [63](#), [89](#), [93](#), [179](#), [180](#), [184](#)
- Ouyang, J., Zhu, Q., Zhao, W., Xu, Y., Chen, W., and Zhong, S. (2005). Biomechanical assessment of the pediatric cervical spine under bending and tensile loading. *Spine*, 30(24):E716–E723. [ii](#), [28](#), [29](#), [38](#), [46](#), [57](#), [58](#)
- Panjabi, M. M. (1973). Three-dimensional mathematical model of the human spine structure. *Journal of Biomechanics*, 6(6):671–680. [26](#)
- Parente, M., Jorge, R. N., Mascarenhas, T., Fernandes, A., and Martins, J. (2009). The influence of the material properties on the biomechanical behavior

- of the pelvic floor muscles during vaginal delivery. *Journal of biomechanics*, 42(9):1301–1306. 24
- Pintar, F. A., Mayer, R. G., Yoganandan, N., and Sun, E. (2000). Child neck strength characteristics using an animal model. *Stapp car crash journal*, 44:77–83. 28, 39
- Sadulaev, S.-M., Lapeer, R., Gerikhanov, Z., and Morris, E. (2017). A haptic user interface to assess the mobility of the newborn’s neck. In *Information Visualisation (IV), 2017 21st International Conference*, pages 218–223. IEEE. 16, 58, 144
- Sellheim, H., Der Geburtskanal, A., des Beckenraumes, F. D., Ebenen, H., des Beckenausgangs, F. D., vom Beckenausgang, R. V., Formveränderung, A., durch Positionswechsel, K. F., des Beckens, N., im grossen Becken, A. d. M., et al. (1906). *Die Beziehungen des Geburtskanales und des Geburtsobjektes zur Geburtsmechanik*. G. Thieme. 11
- Senteler, M., Weisse, B., Rothenfluh, D. a., and Snedeker, J. G. (2015). Intervertebral reaction force prediction using an enhanced assembly of OpenSim models. *Computer Methods in Biomechanics and Biomedical Engineering*, 5842(January):1–11. 64
- Simple DirectMedia Layer (2016). About SDL.
<https://www.libsdl.org/>
Website accessed 22th September, 2016. 195
- Smidt, G. L., McQuade, K., and Wei, S.-H. (1995). Sacroiliac kinematics for reciprocal. *Spine*, 20(9):1047–1054. 14
- Symonds, E. (1992). *Essential Obstetrics and Gynaecology*. Churchill Livingstone, 16 edition. 4, 6, 8, 9, 10, 11
- Tass International (2019). Madymo.
<https://tass.plm.automation.siemens.com/madymo>
Website accessed 14th September, 2019. 26

- The Touch Haptic Device (2019). The Touch™ Haptic Device.
<https://uk.3dsystems.com/haptics-devices/touch>
Website accessed 8th May, 2019. 51
- Tien, C. and Huston, R. (1987). Numerical advances in gross-motion simulations of head/neck dynamics. *Journal of Biomechanical Engineering*, 109(2):163–168. 25
- Van Ee, C. A., Nightingale, R. W., Camacho, D., Chancey, V. C., Knaub, K. E., Sun, E. A., and Myers, B. S. (2000). *Tensile properties of the human muscular and ligamentous cervical spine*. PhD thesis, Duke University Durham, NC. 29
- Van Lopik, D. and Acar, M. (2007). Development of a multi-body computational model of human head and neck. *Proceedings of the Institution of Mechanical Engineers, Part K: Journal of Multi-body Dynamics*, 221(2):175–197. 26, 64
- Verspyck, E., Goffinet, F., Hellot, M. F., Milliez, J., and Marpeau, L. (1999). New-born shoulder width: a prospective study of 2222 consecutive measurements. *BJOG: An International Journal of Obstetrics & Gynaecology*, 106(6):589–593. 109
- Vleeming, A., Schuenke, M., Masi, A., Carreiro, J., Danneels, L., and Willard, F. (2012). The sacroiliac joint: an overview of its anatomy, function and potential clinical implications. *Journal of anatomy*, 221(6):537–567. 101, 105
- Wismans, J., Philippens, M., Van Oorschot, E., Kallieris, D., and Mattern, R. (1987). Comparison of human volunteer and cadaver head-neck response in frontal flexion. Technical report, SAE Technical Paper. 25
- Wismans, J., Van Oorschot, H., and Woltring, H. (1986). Omni-directional human head-neck response. Technical report, SAE Technical Paper. 25
- Yamada, H., Evans, F. G., et al. (1970). Strength of biological materials. *AGRIS*. 37
- Zajac, F. E. (1988). Muscle and tendon: properties, models, scaling, and application to biomechanics and motor control. *Critical reviews in biomedical engineering*, 17(4):359–411. 27

Appendices

Appendix A

Experimental study of cardinal movements with different dimension of the fetal head

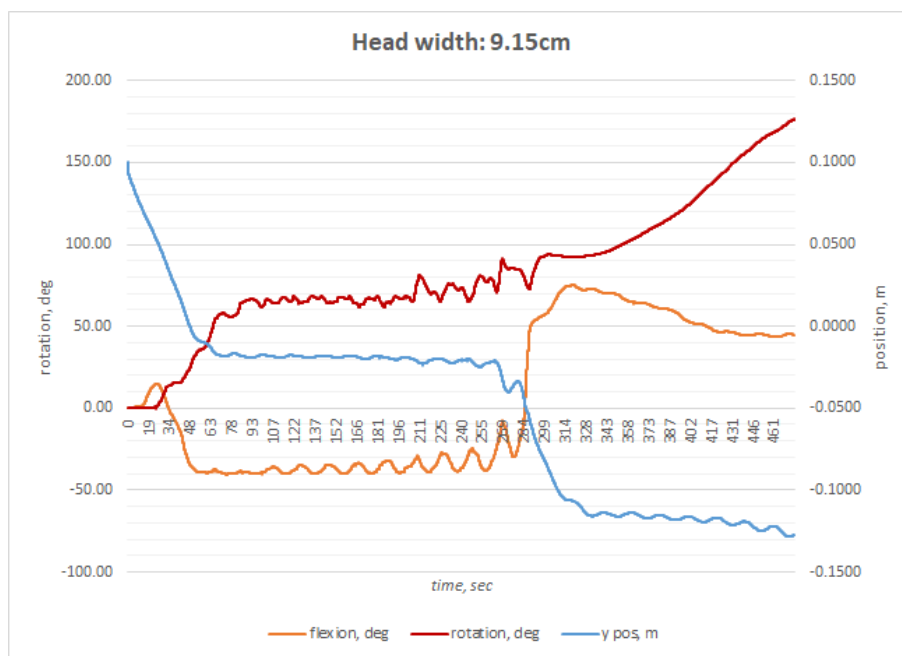


Figure A.1: Simulating childbirth (LOT) with a head width of 9.15cm.

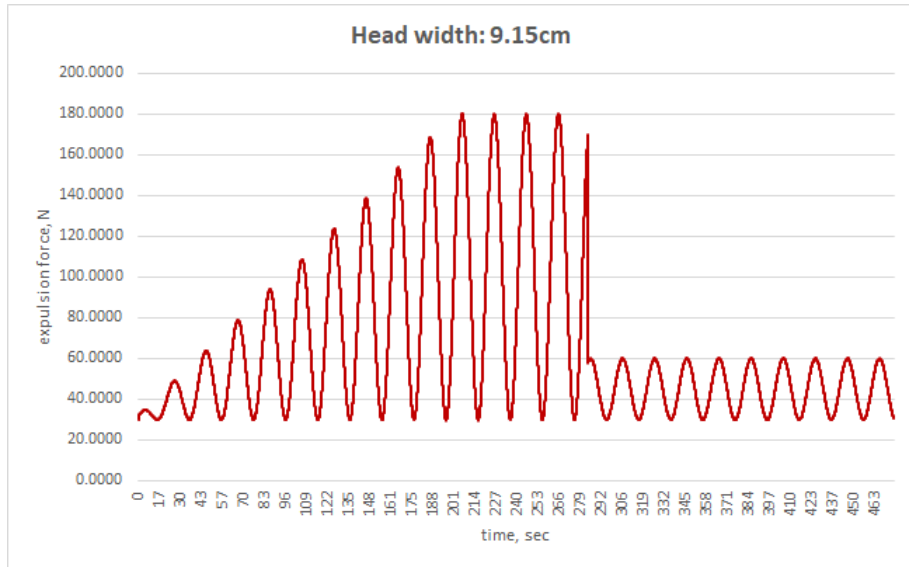


Figure A.2: Graph of the increasing periodic expulsion force (red curve). The expulsion force is decreased after the delivery of the fetal head.



Figure A.3: Simulating childbirth (LOT) with a head width of 9.2cm.

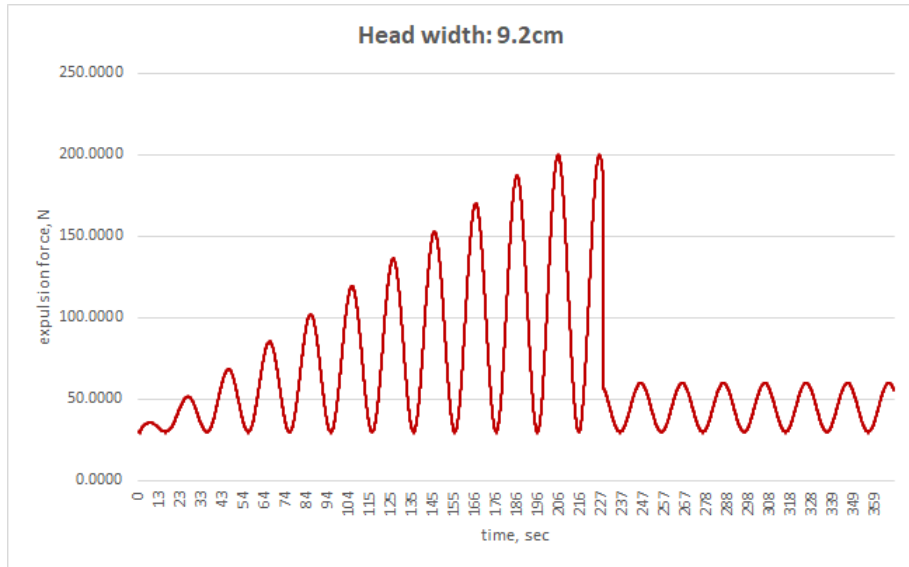


Figure A.4: Graph of the increasing periodic expulsion force (red curve). The expulsion force is decreased after the delivery of the fetal head.

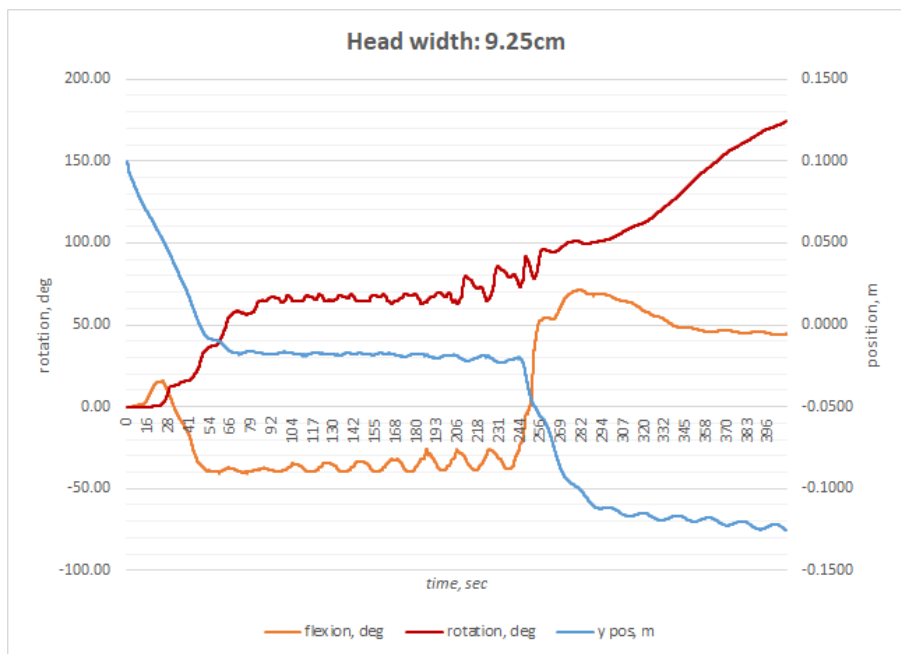


Figure A.5: Simulating childbirth (LOT) with a head width of 9.25cm.

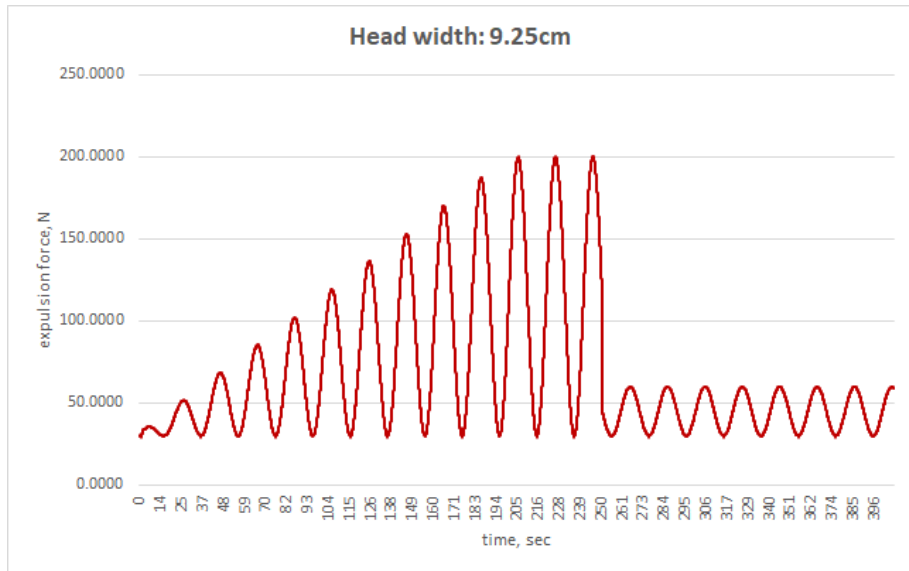


Figure A.6: Graph of the increasing periodic expulsion force (red curve). The expulsion force is decreased after the delivery of the fetal head.

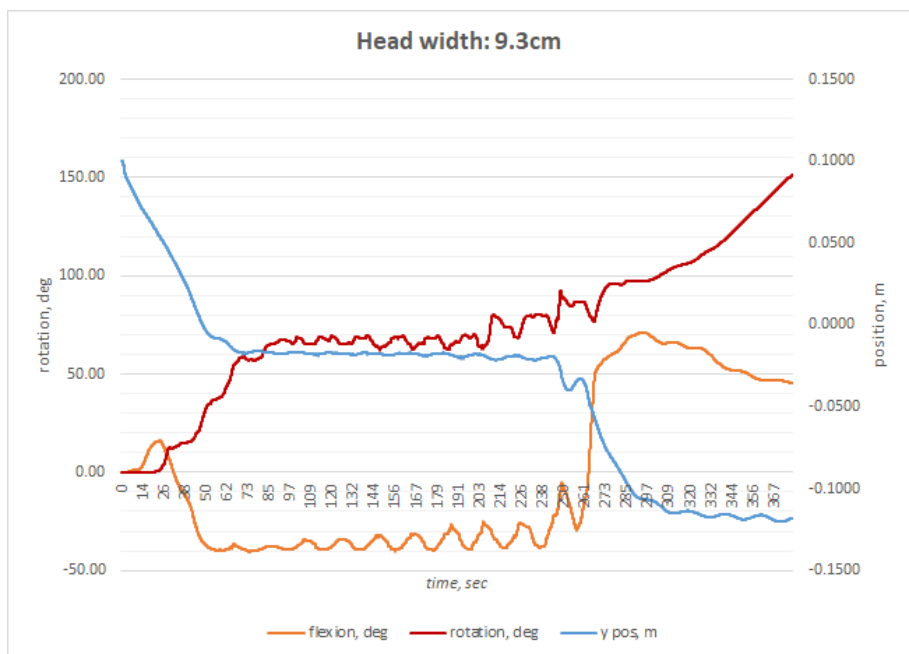


Figure A.7: Simulating childbirth (LOT) with a head width of 9.3cm.

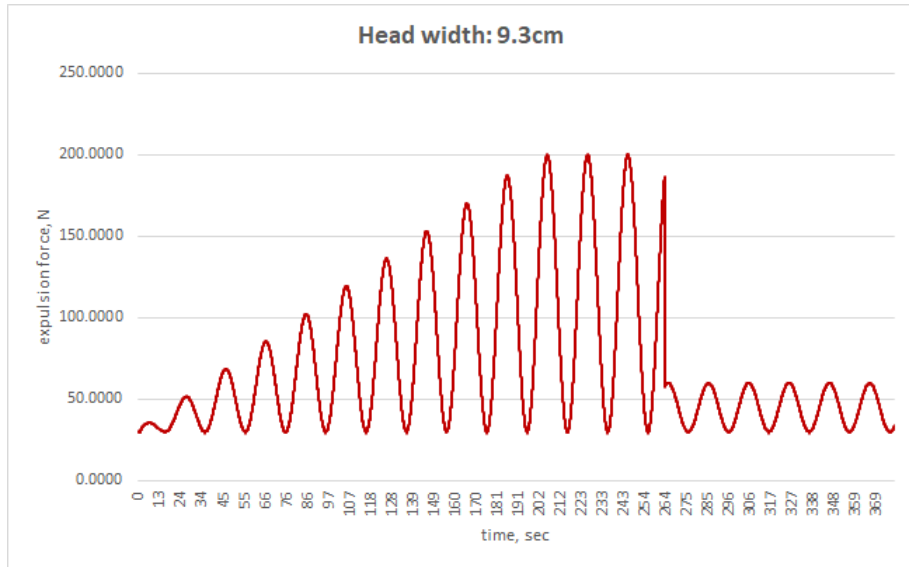


Figure A.8: Graph of the increasing periodic expulsion force (red curve). The expulsion force is decreased after the delivery of the fetal head.

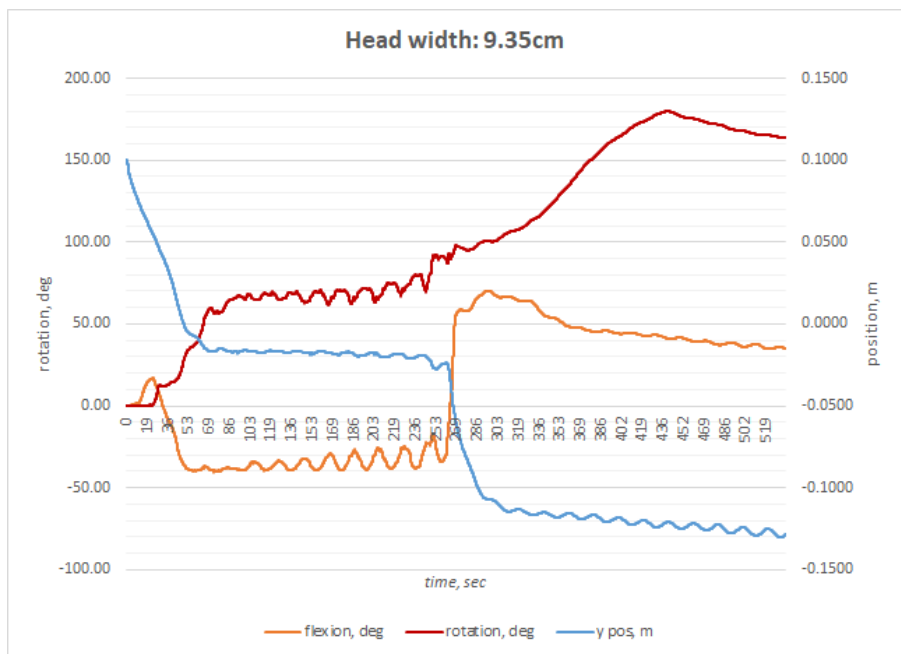


Figure A.9: Simulating childbirth (LOT) with a head width of 9.35cm.

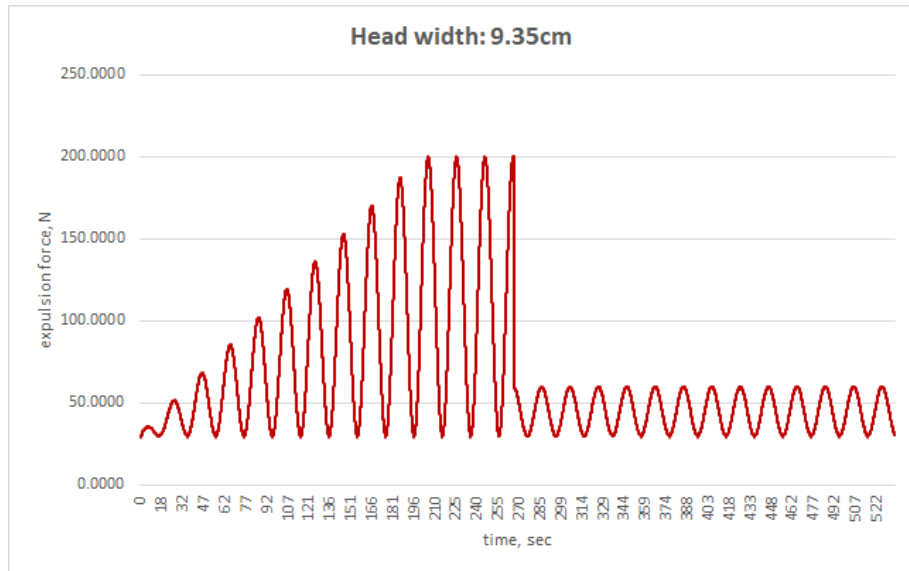


Figure A.10: Graph of the increasing periodic expulsion force (red curve). The expulsion force is decreased after the delivery of the fetal head.

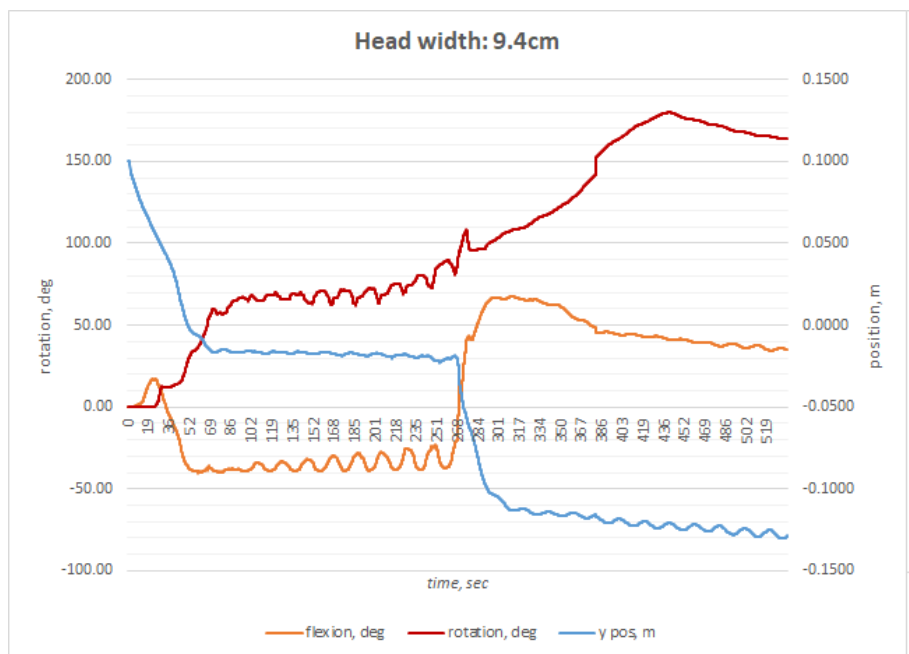


Figure A.11: Simulating childbirth (LOT) with a head width of 9.4cm.

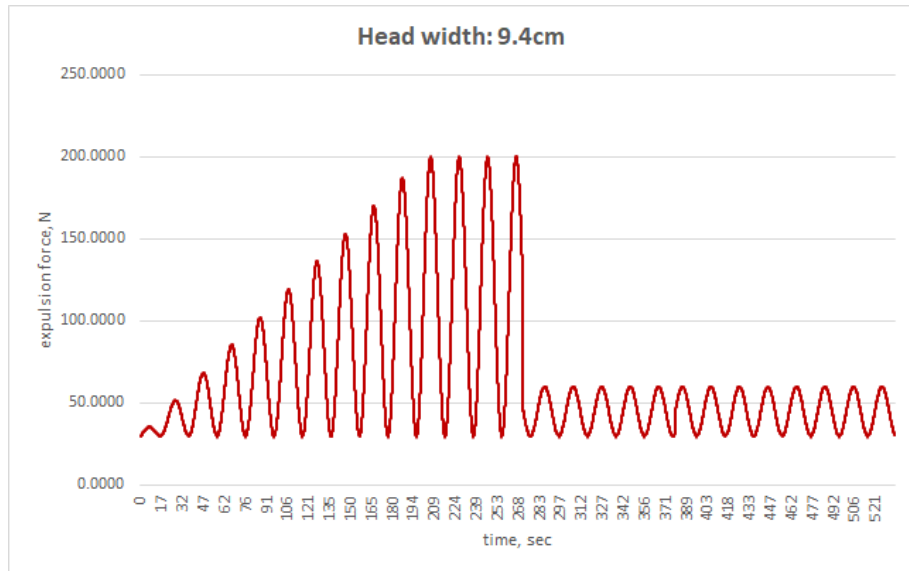


Figure A.12: Graph of the increasing periodic expulsion force (red curve). The expulsion force is decreased after the delivery of the fetal head.



Figure A.13: Simulating childbirth (LOT) with a head width of 9.45cm.

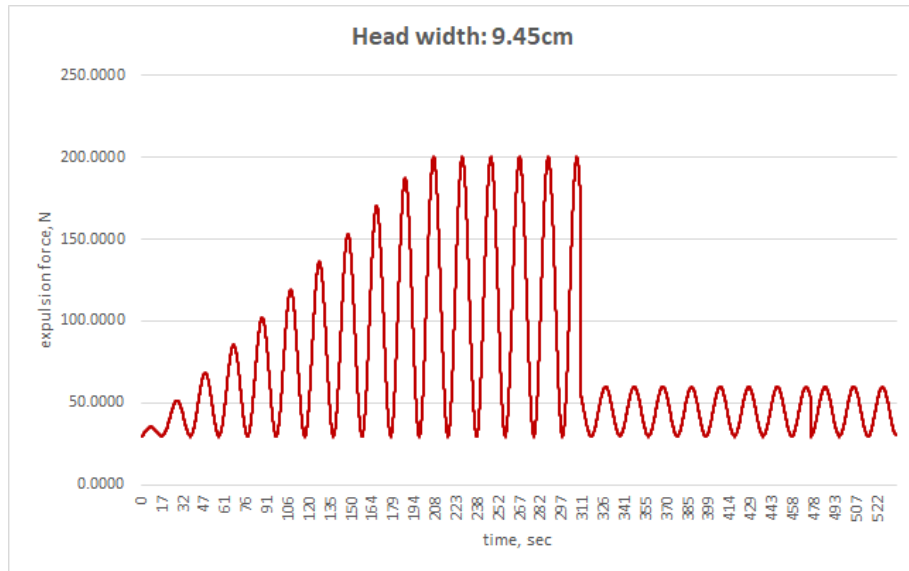


Figure A.14: Graph of the increasing periodic expulsion force (red curve). The expulsion force is decreased after the delivery of the fetal head.

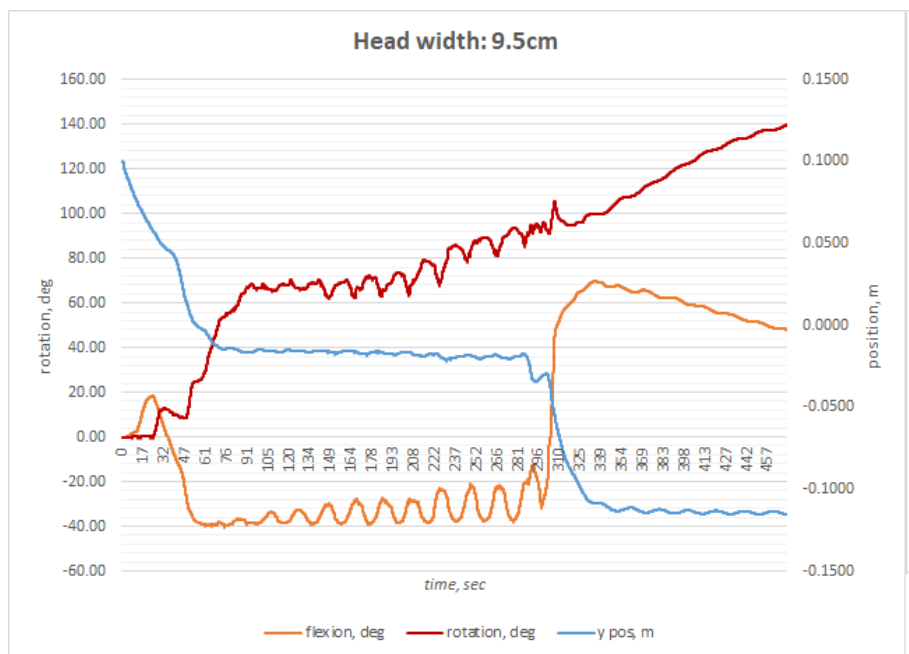


Figure A.15: Simulating childbirth (LOT) with a head width of 9.5cm.

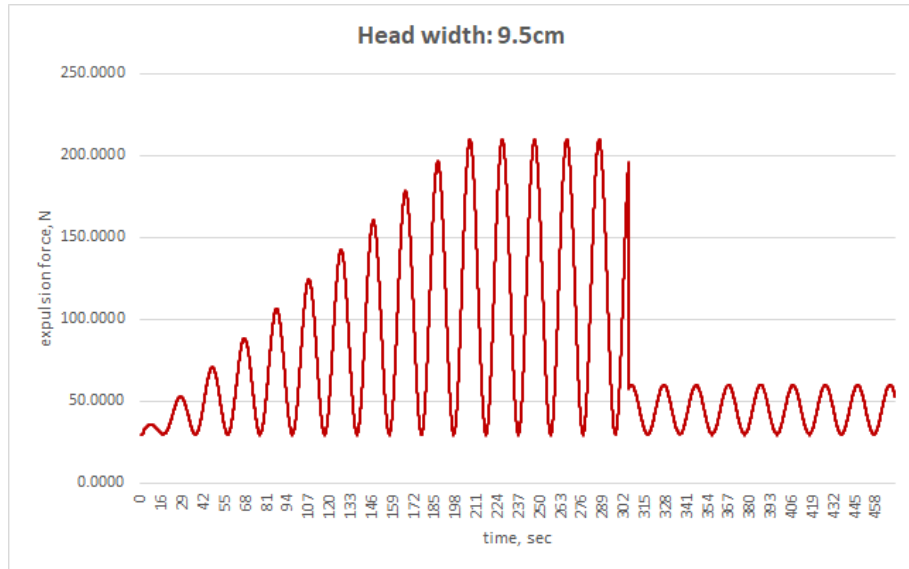


Figure A.16: Graph of the increasing periodic expulsion force (red curve). The expulsion force is decreased after the delivery of the fetal head.

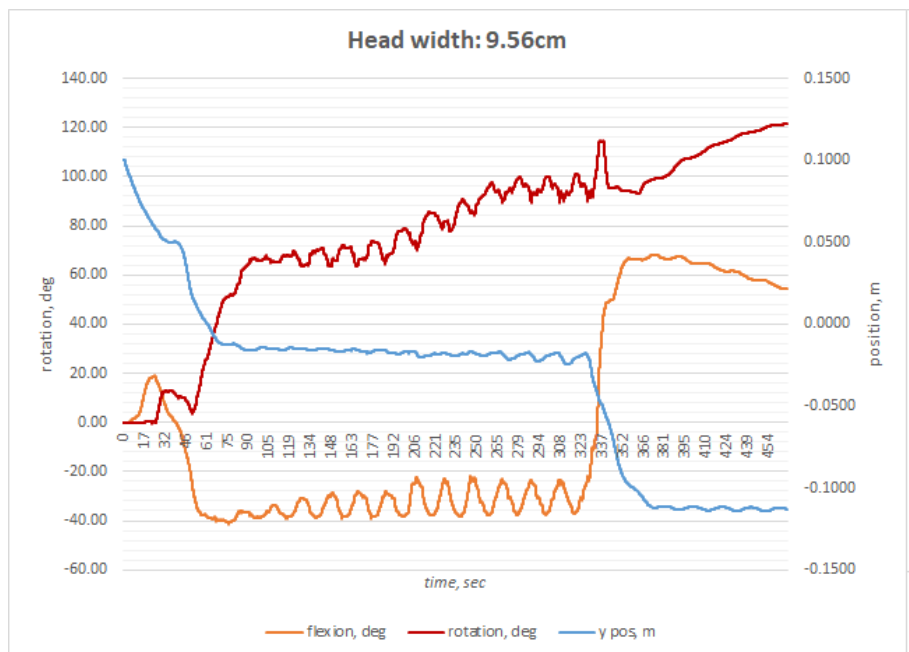


Figure A.17: Simulating childbirth (LOT) with a head width of 9.56cm.

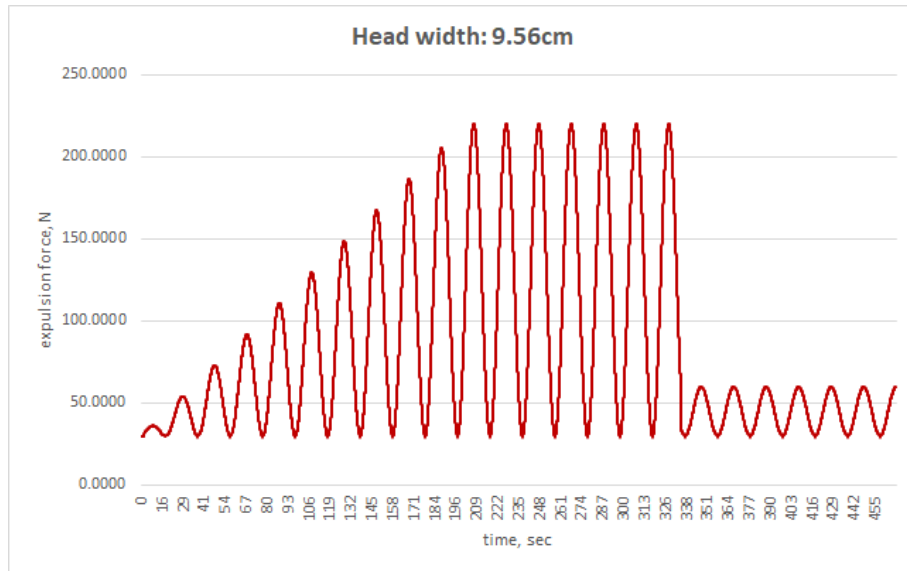


Figure A.18: Graph of the increasing periodic expulsion force (red curve). The expulsion force is decreased after the delivery of the fetal head.

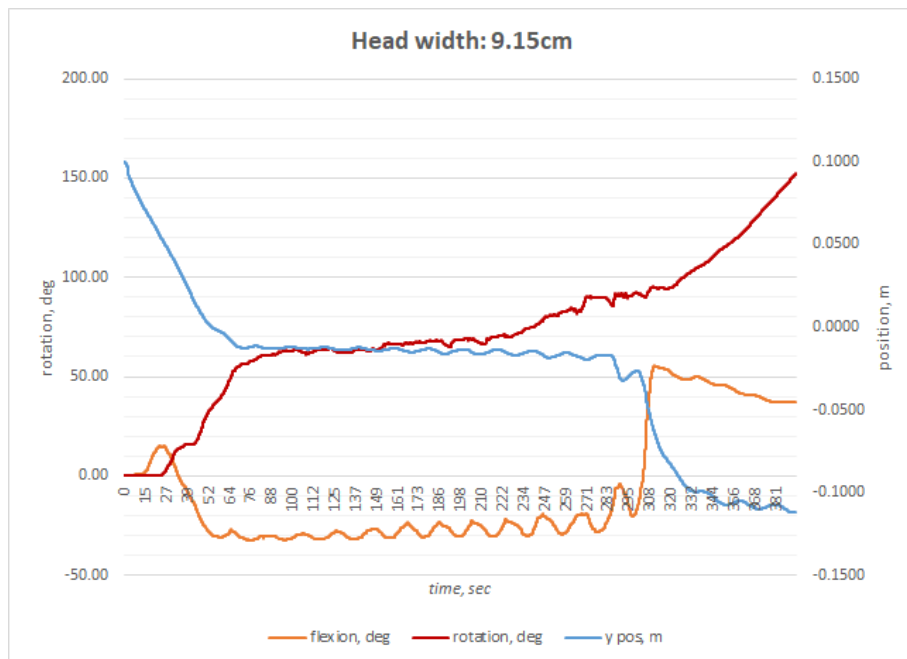


Figure A.19: Simulating childbirth (LOT) with a head width of 9.15cm and neck length of 2.4cm.

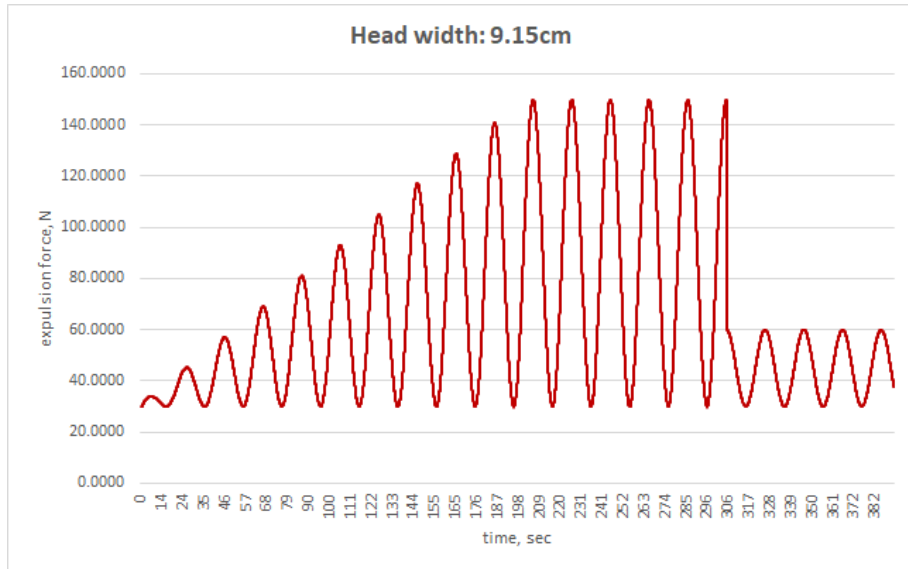


Figure A.20: Neck length: 2.4cm. Graph of the increasing periodic expulsion force (red curve). The expulsion force is decreased after the delivery of the fetal head.

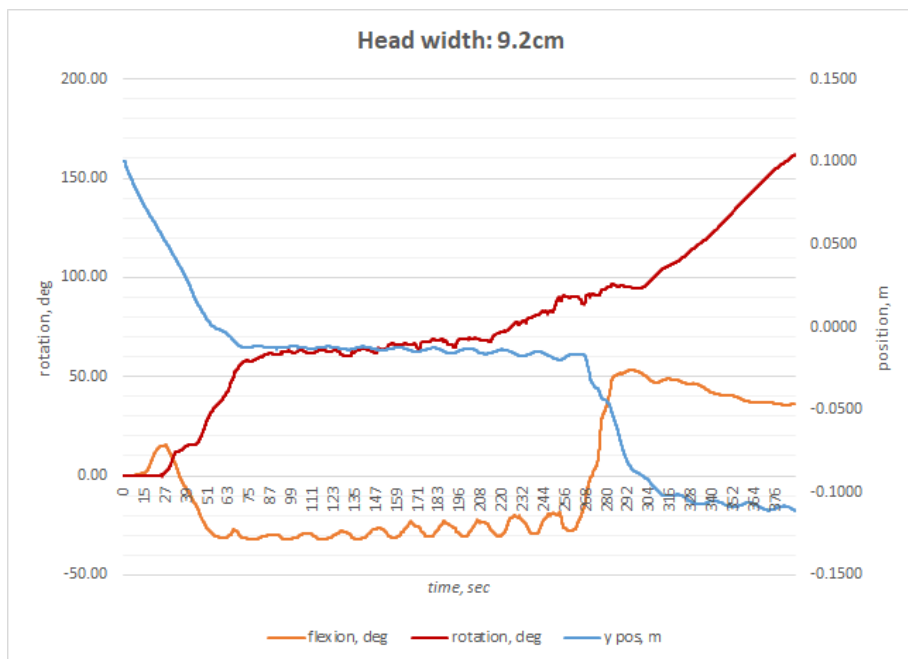


Figure A.21: Simulating childbirth (LOT) with a head width of 9.2cm and neck length of 2.4cm.

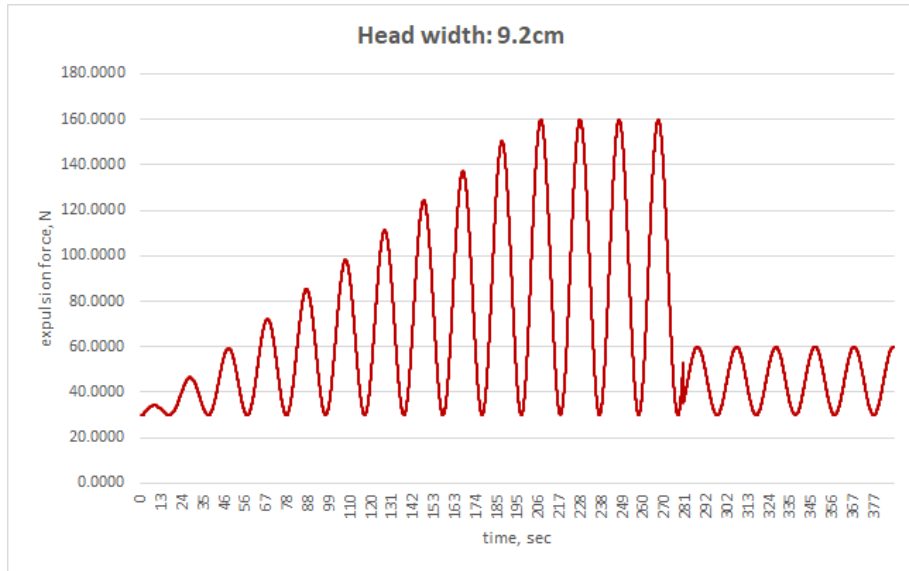


Figure A.22: Neck length: 2.4cm. Graph of the increasing periodic expulsion force (red curve). The expulsion force is decreased after the delivery of the fetal head.

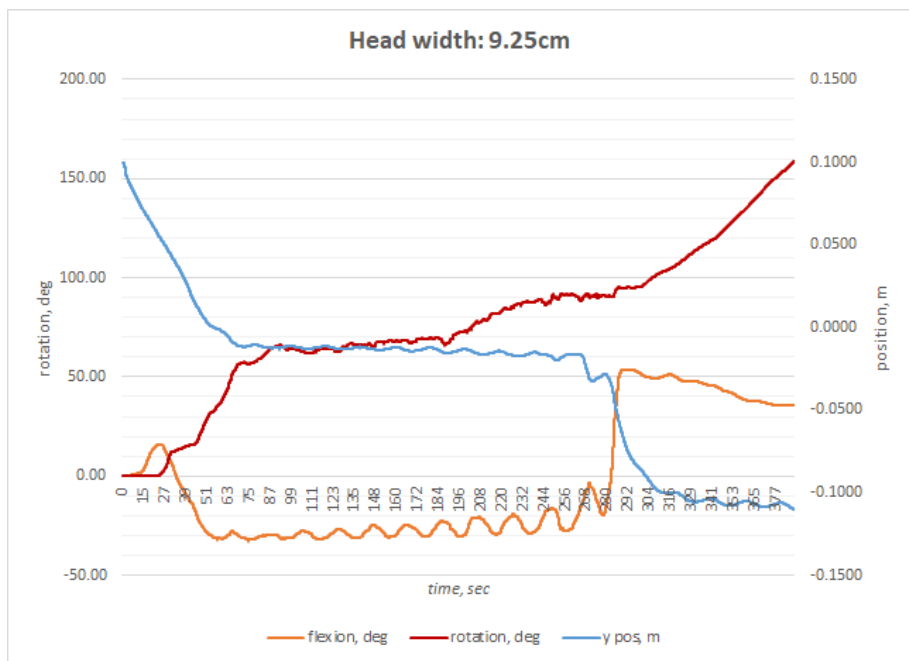


Figure A.23: Simulating childbirth (LOT) with a head width of 9.25cm and neck length of 2.4cm.

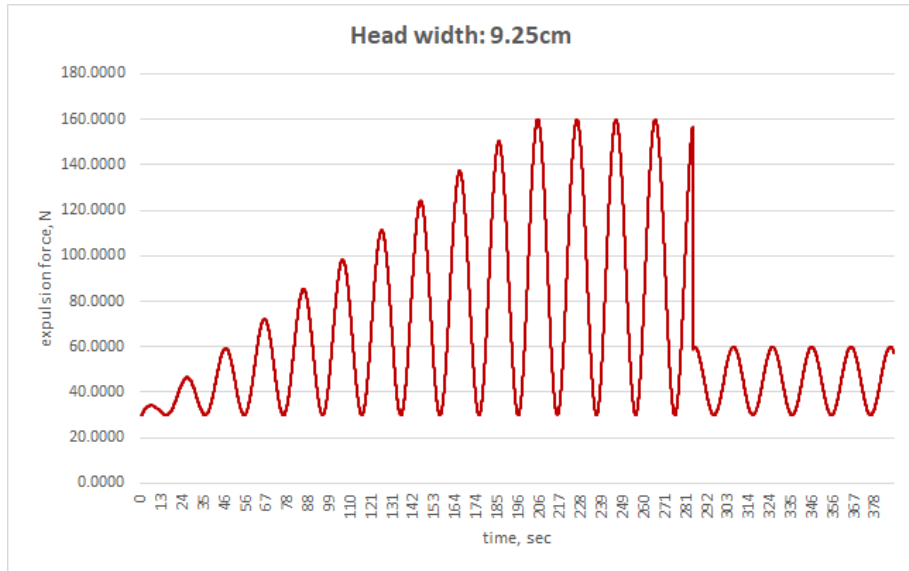


Figure A.24: Neck length: 2.4cm. Graph of the increasing periodic expulsion force (red curve). The expulsion force is decreased after the delivery of the fetal head.

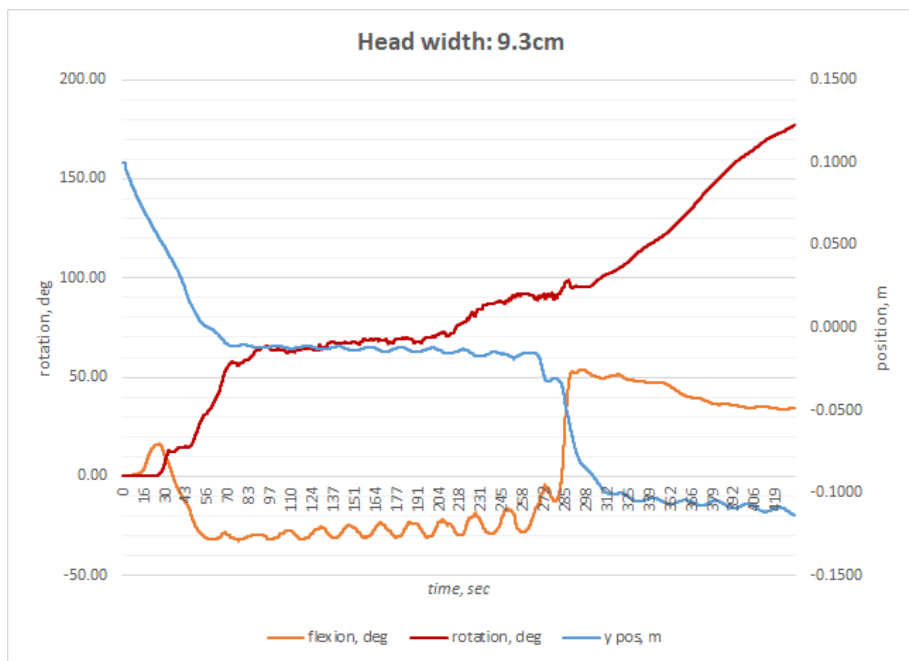


Figure A.25: Simulating childbirth (LOT) with a head width of 9.3cm and neck length of 2.4cm.



Figure A.26: Neck length: 2.4cm. Graph of the increasing periodic expulsion force (red curve). The expulsion force is decreased after the delivery of the fetal head.

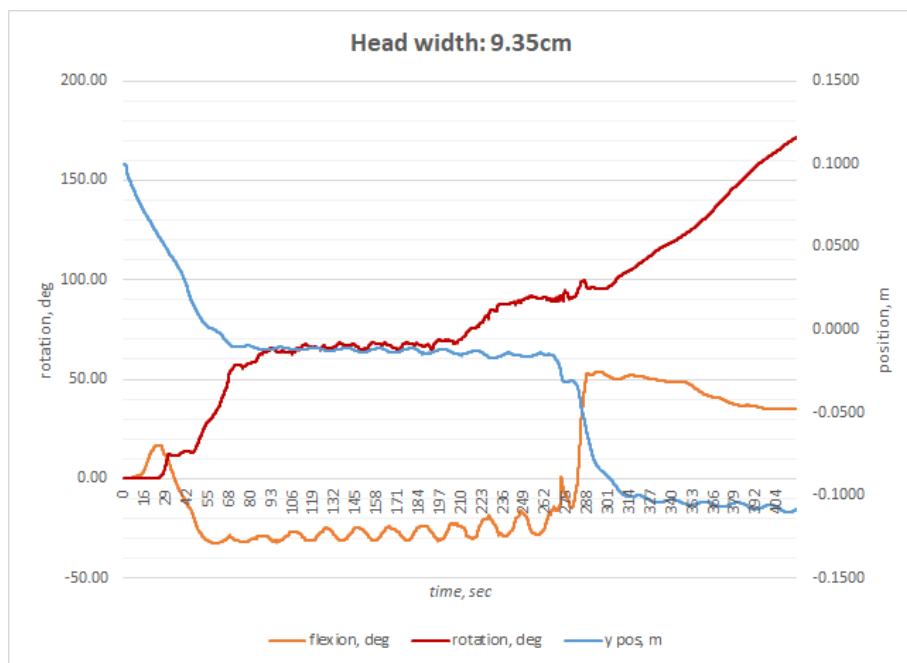


Figure A.27: Simulating childbirth (LOT) with a head width of 9.35cm and neck length of 2.4cm.

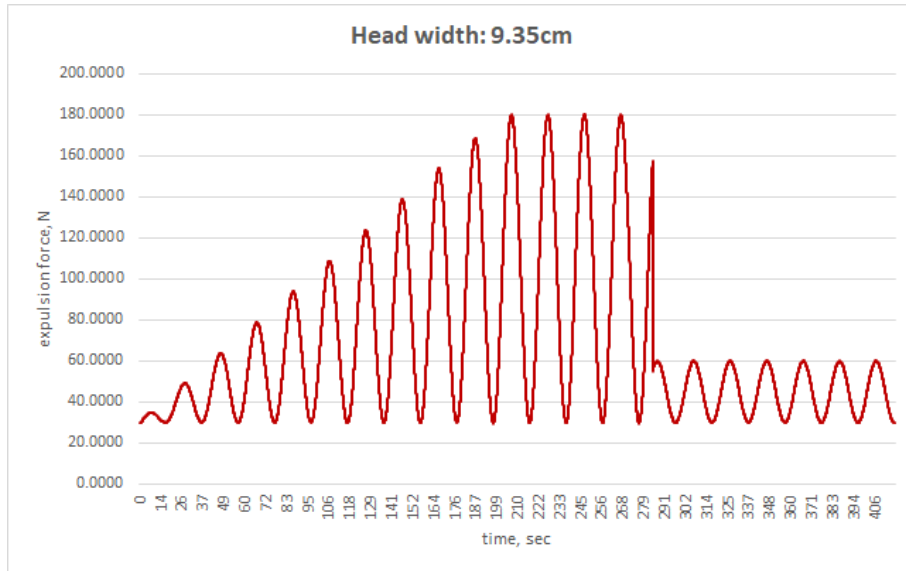


Figure A.28: Neck length: 2.4cm. Graph of the increasing periodic expulsion force (red curve). The expulsion force is decreased after the delivery of the fetal head.

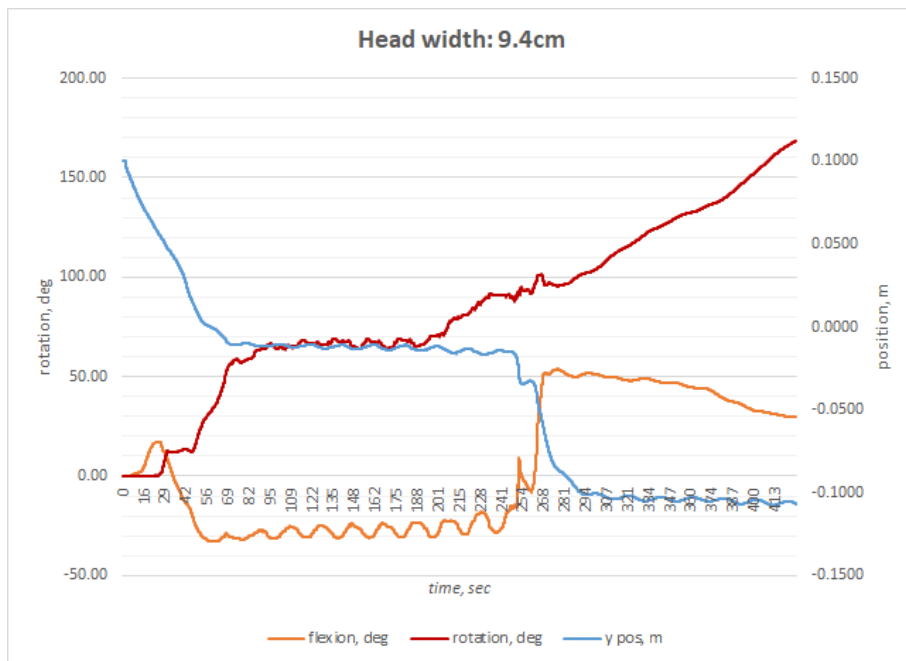


Figure A.29: Simulating childbirth (LOT) with a head width of 9.4cm and neck length of 2.4cm.

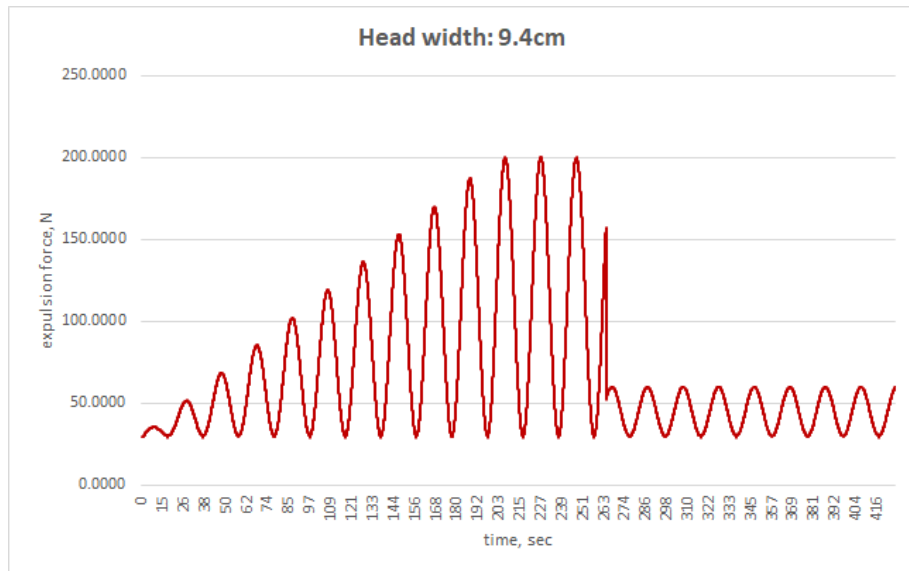


Figure A.30: Neck length: 2.4cm. Graph of the increasing periodic expulsion force (red curve). The expulsion force is decreased after the delivery of the fetal head.

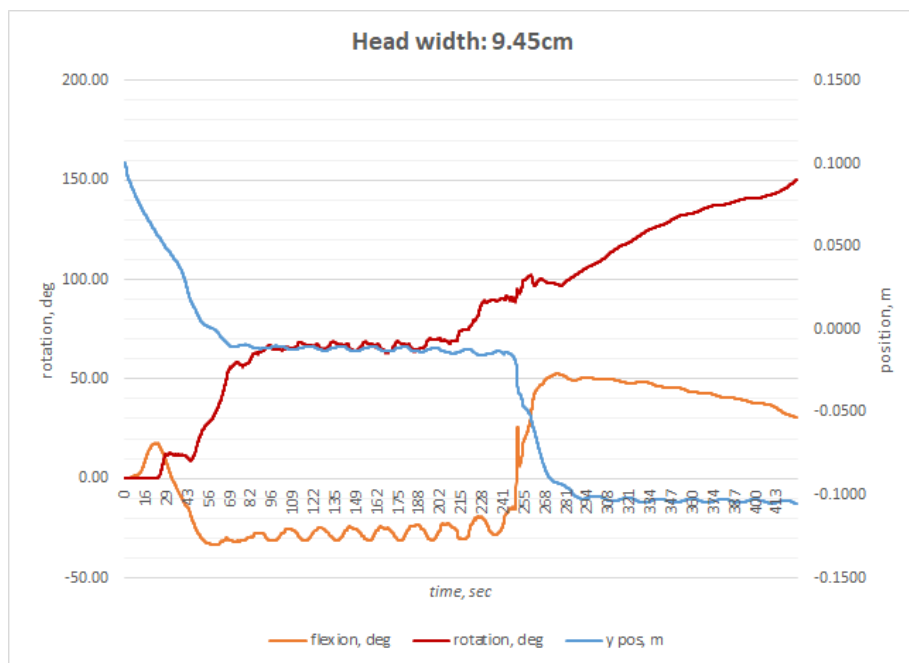


Figure A.31: Simulating childbirth (LOT) with a head width of 9.45cm and neck length of 2.4cm.

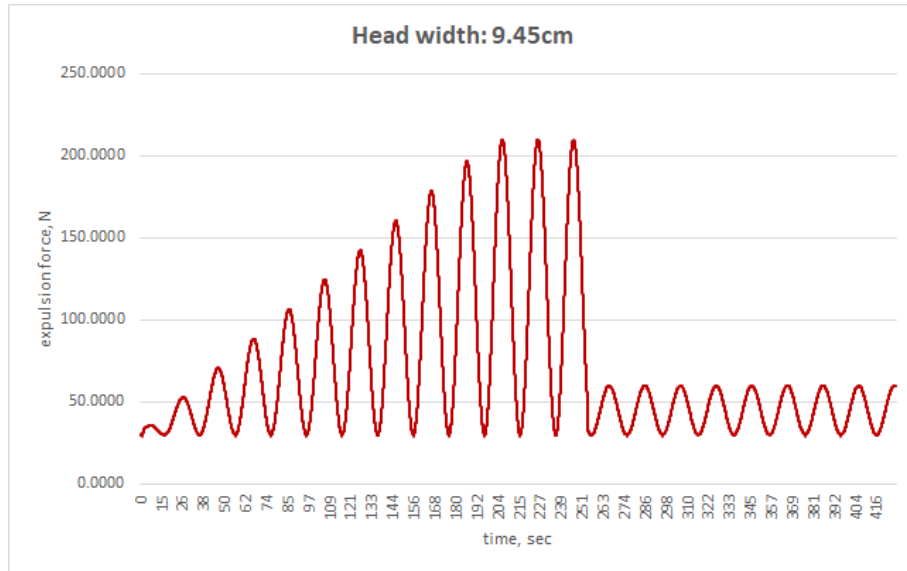


Figure A.32: Neck length: 2.4cm. Graph of the increasing periodic expulsion force (red curve). The expulsion force is decreased after the delivery of the fetal head.

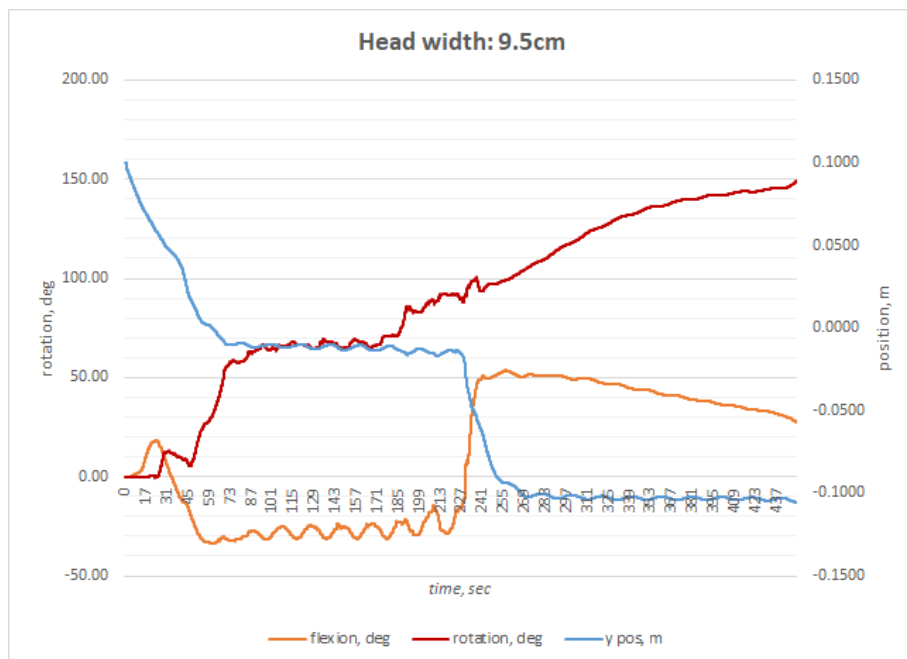


Figure A.33: Simulating childbirth (LOT) with a head width of 9.5cm and neck length of 2.4cm.

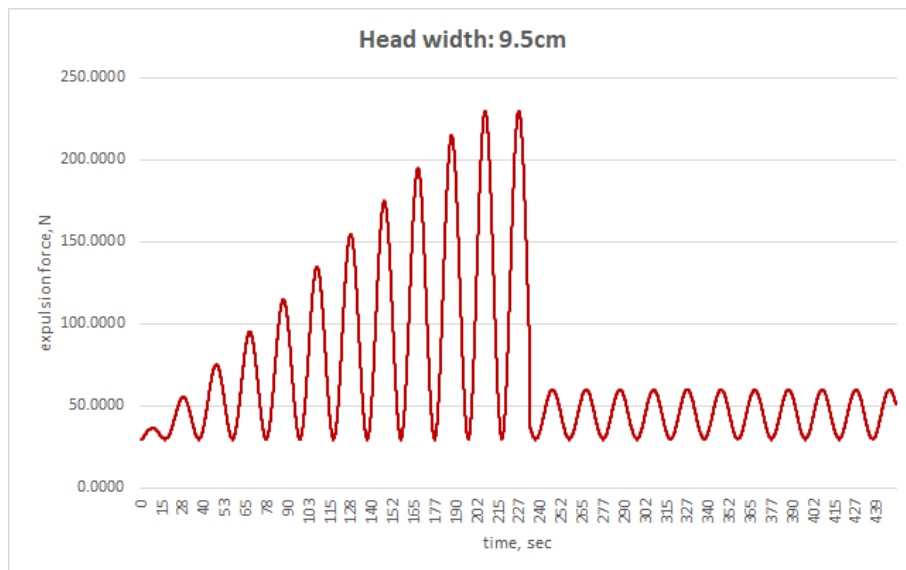


Figure A.34: Neck length: 2.4cm. Graph of the increasing periodic expulsion force (red curve). The expulsion force is decreased after the delivery of the fetal head.

Appendix B

A clinical study of ROM in healthy newborn babies

B.1 Introduction

The purpose of this study is to find out the range of motion of a newborn baby's neck, its muscle strength, other physical measurements of newborns such as mass, head circumference as well as acquire the trajectory followed by a newborn's head during various motions.

The primary aim of this observational study is to collect data for the purpose of validating a computational neck model used in a childbirth simulator. However, Range of Motions (ROMs) and the muscle strength can also be used for development, improvement and validation of computational neck models used in other applications such as virtual car crash simulations, and whiplash investigation applications.

There are presently very limited data in the literature regarding the normal range of movements of the head and neck in infants. It is important to mention that currently there are data on lateral flexion and side rotation only, acquired by measuring ROMs of the neck of 38 infants (at the ages of 2, 4, 6, and 10 months) using a joint protractor (Öhman and Beckung, 2008), however, the data do not include measurements for newborns. Also there are a few computer neck models of infants developed by Bondy et al. (2014), Jones et al. (2015), but both focus

on flexion and extension only.

This study is set to be conducted in Norwich and Norfolk University Hospital. The study requires 40 newborns of the age up to one week old, with half males and half females.

B.2 Motivation

Our research team is currently working on a state-of-the-art computer based virtual childbirth simulator (BirthView). The ultimate purpose of the simulator is to be used for training midwifery students and predicting difficult (abnormal) labour. BirthView is the only forward-engineered simulator capable of producing seven cardinal movements successfully during physiological (normal) labour.

However, prior to serving its purpose in simulating abnormal labour (e.g. shoulder dystocia), every component in the simulator needs to be tested and validated thoroughly. One of the most important elements, i.e. the neck of the newborn (computer model), is currently represented as a basic spring, whereas in real life, the neck exhibits more complicated behaviour than a Hookean spring. For that reason, the neck model in BirthView is being further improved.

Due to scarcity of information on newborns, the developed basic spring neck model has been validated against the limited data on the range of motion of the neck in infants, aged 2 to 10 months old (Öhman and Beckung, 2008). Unfortunately there is a possibility that the neck of an infant of 2 months old exhibits significantly different behaviour to a newborn (Luck, 2012) and therefore more data is required on ROM of the neck in newborns.

This clinical study is meant to fill the gap of missing data on ROM of the neck in newborns.

B.3 Methods

We have developed a device as an extension of the baby mat in order to facilitate easy measuring of ROMs in three planes: sagittal, axial and coronal (see Figure B.1). The device is made of plexiglass sheets and is designed to accommodate for the mat depicted in Figure B.2. The device has a transparent protractor

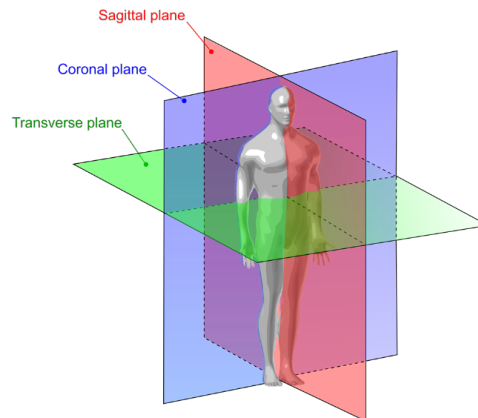


Figure B.1: Three planes of ROM.

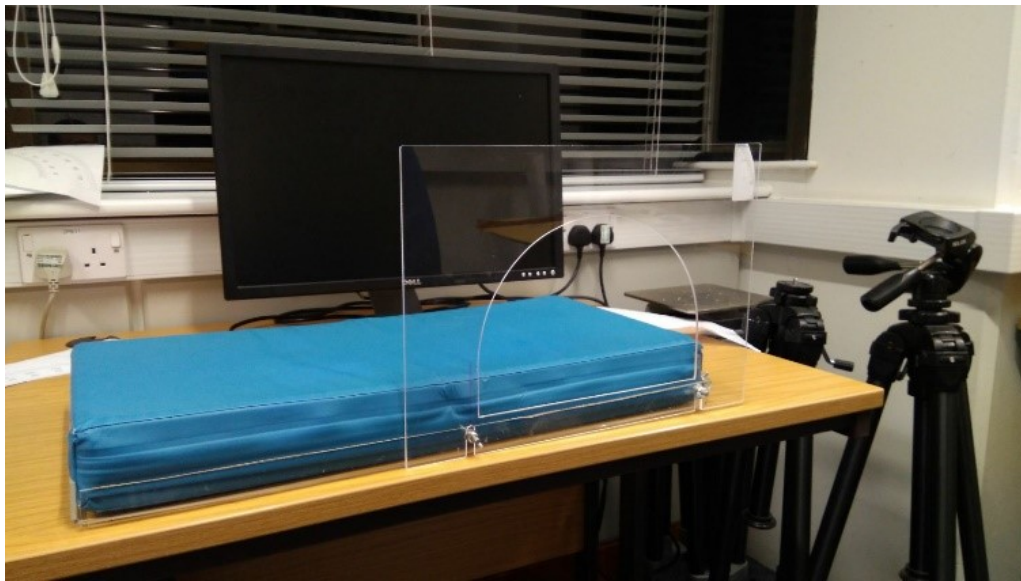


Figure B.2: Measuring device of ROMs of the neck of a newborn.

on the side which can be easily adjusted vertically to correspond to the selected rotational point.

With parental consent, a video camera will record the whole process and the following motions of the head will be performed: flexion, lateral flexion, side rotation and extension.

Figure B.4 and table B.1 summarise all the measurements that need to be



Figure B.3:
Accelerometer
BWT901CL

An accelerometer, using Bluetooth to send data to a laptop, will be used to measure isotonic muscle strength. The device can be attached to an infant hat with velcro and transmits data to a laptop using class 2 Bluetooth, which is considered to be safe ((Hietanen and Alanko, 2005)). The device is further coated with tinfoil to reduce radio-frequency (RF) emissions.

performed during the study.

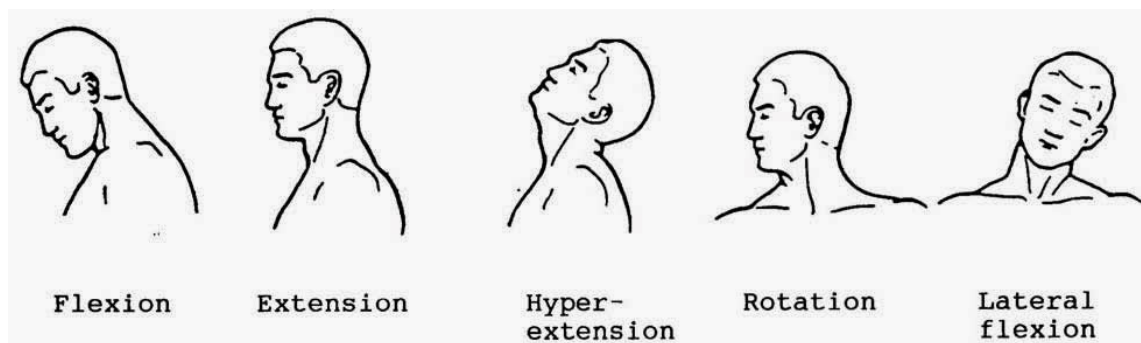


Figure B.4: Range of motion. Accessed February 2018.
<<http://arc4life.blogspot.co.uk/2014/02/a-look-at-neck-range-of-motion.html>>

Table B.2 summarises all the measurements that are normally recorded after birth, and are required for the study.

Head weight will be measured using either of the following two methods:

- using a sensitive scale similar to the one in Figure B.6. The baby's head will be placed on the scale, while the rest of the body will be supported by the examiner.
- using a dynamometer (see Figure B.7). The baby will be wearing a safety helmet (see Figure B.5) and the dynamometer will be attached to it. While

Table B.1: Measurements required for finding range of motion of a newborn baby's head (template).

Baby	Flexion	Hyper-extension	Lateral bending	Side rotation

Table B.2: Measurements that are normally recorded after birth. **Bold** items may have to be measured during the study (template).

Baby	Gestational age and Age (days)	Gender	Body Weight	Head Circumference	Head Weight	Biparietal Diameter

baby is lying in supine position, the dynamometer will be slowly pulled up to slightly lift the baby's head off the mat.

The biparietal diameters will be measured using calipers.

B.4 Study

Location: Norwich and Norfolk University Hospital.

Newborns: This study requires 40 healthy babies.

Postnatal age of babies: up to a week.

Number and gender: 20 male and 20 female.

Preferred stage of activity (from 1 to 4):

- asleep - 1
- half asleep - 2
- just awake - 4
- normal (fully awake) – 3

If a newborn is tense or uncooperative the measurements will be discontinued.

Duration: a cycle of measurements for a baby is expected to take no longer than 20 minutes

Parents should be present at all times.

B.5 Procedures

The following four procedures will be recorded with a video camera to subsequently find the aforementioned kinematic trajectories of the newborn's head at flexion/extension, side rotation and lateral bending and to obtain ROM values.

B.6 Measuring ROMs

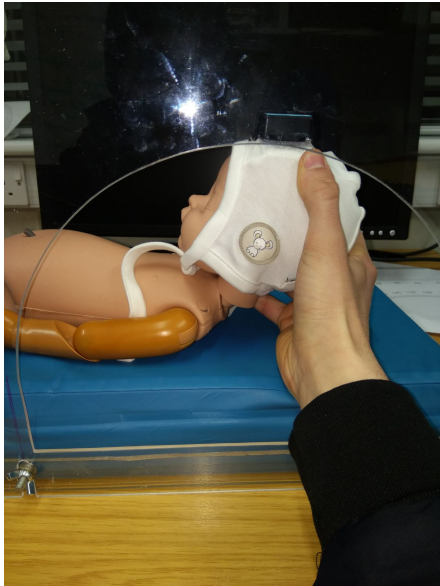


Lateral bending. A large protractor is placed flat on a bed and a newborn is in supine position with its shoulders stabilized and the head is in the cavity/inner arc of the protractor. Alternatively, a large protractor can be drawn on an examination table similar to the study by Öhman and Beckung (2008).

The head is carefully bent until moderate resistance is met and the maximum angle is measured using the protractor and noted down.



Side rotation. A newborn is in supine position on a bed with its shoulders stabilized and the head over the edge of a bed, supported by the examiner. A large protractor is fixed on the side, either on the left or right side of the newborn so that the head is in the cavity/inner arc of the protractor. The head is then carefully rotated sideways until moderate resistance is met and the maximum angle is measured and noted down. The procedure is repeated for both sides.



Flexion. A newborn is lying in supine position on a bed with its shoulders stabilized. A large protractor is fixed on the side, either on the left or right side of the newborn. The head is carefully bent forward (flexed) until a chin touches a chest and the maximum angle is measured using the protractor and noted down.



Hyper-Extension will be measured by following the common pediatric examination procedure to evaluate the tone of a newborn's neck. The procedure will be recorded and subsequently processed to find out the ROM with causing as little stress as possible to the baby.

B.7 Analysis

- The obtained video data and accelerations will be used to acquire and validate the following data: ROMs, kinematic curvatures, neck strength.
- The video will be analysed using OpenCV and OpenPose which are libraries of computer vision functions for image/video processing.
- The acceleration data will be analysed using a custom software.
- ROM data will be validated using both the protractor and computer vision techniques. Also both accelerations and ROMs can be validated with the accelerometer and, hence, all three methods can be compared to one another

to establish the level of accuracy of computer vision methods in finding ROMs and accelerations from the recorded video.

B.8 Application

The data will be used to develop another neck model and its validation. Also the experimenter himself is the perfect candidate to validate the computer neck model using BirthViewH.

The data can be used in modelling a computational newborn neck model in a variety of virtual reality simulations: childbirth simulation, car crash simulations, including assessing safety of a child restraint and investigating whiplash injuries.



Figure B.5: Safety helmet for infants.



Figure B.6: Scale.



Figure B.7: Dynamometer.

Appendix C

Instructions on BirthViewH for midwives

C.1 Aim

The aim of this experiment is to assess the strength and flexibility of the newborn's neck to allow us to create a realistic computer based model. The computer based neck model will be used as part of our childbirth simulator. Indeed, the fetal neck is a crucial component of the cardinal movements during childbirth and to ensure the simulator exhibits the cardinal movements, we require realistic behaviour of the fetal neck.

C.2 Procedure

We have created a simulation software showing a fetal head, neck and trunk on the screen. Interaction with the head is facilitated using two haptic devices (See Figure 3.11). The haptics devices allow you to rotate the displayed fetal head in 3D. You will also feel resistive moments and forces (force feedback) from the haptics device whilst doing this. The degree of flexibility or stiffness that you will sense depends on mechanical properties of the neck muscles. The aim of the experiment is to validate and adjust the mechanical properties of the computational fetal neck model so that its rotations and flexibility feel realistic.

C.3 Instructions

These instructions are intended for midwives and professionals in obstetrics to conduct the experiments on validation of the fetal cervical neck and spine.

The professionals are required to apply certain force to the fetal skull on the screen (See picture) using two Haptic devices and validate the resistance of the skull, during bending and rotation, against their real-life experience.

Please follow the instruction below and do not hesitate to approach the experimenter for further guidance.

C.4 Setting up stiffness and damping value

Try to rotate the fetal head on the screen using the provided Haptics devices (See picture) and inform the experimenter if the head is resisting movement realistically

C.5 Flexion/extension/lateral bending testing

- Try to bend the fetal head and inform the experimenter if the head is resisting movement realistically
- Allow time to adjust the stiffness of the neck if necessary
- Bend until the head completely resists further bending and inform the experimenter about the realism of the maximum bending angle
- Try to flex further and inform the experimenter whether resistance of the head feels realistic.

C.6 Side rotations testing

- Try to rotate the fetal head and inform the experimenter if the head is resisting rotation realistically

- Allow time to adjust the stiffness of the neck if necessary
- Rotate until the head completely resists further rotation and inform the experimenter about the realism of the maximum rotational angle
- Try to rotate further and inform the experimenter whether resistance of the head feels realistic

Appendix D

Glossary

Anatomical terms MedicineNet (2019); The Free Dictionary (2019)

- Pelvic floor: The soft tissues enclosing the pelvic outlet.
- Occiput: The back of the head.
- Pubic symphysis/Symphysis pubis: The area in the front of the pelvis where the pubic bones meet.
- Fetus: An unborn offspring, from the embryo stage (the end of the eighth week after conception, when the major structures have formed) until birth.
- Introitus: The exterior opening to the vagina, the muscular canal that extends from the cervix to the outside of the female body.
- Symphysis pubis: The area in the front of the pelvis where the pubic bones meet.
- Anterior: The front, as opposed to the posterior.
- Posterior: The back or behind, as opposed to the anterior.
- Anteroposterior position: From front to back. When a chest x-ray is taken with the back against the film plate and the x-ray machine in front of the patient it is called an anteroposterior (AP) view. As opposed to from back to front (which is called posteroanterior).

- Posteroanterior position: From back to front.
- Cervix: The cervix is the lower, narrow part of the uterus (womb). The uterus, a hollow, pear-shaped organ, is located in a woman's lower abdomen, between the bladder and the rectum. The cervix forms a canal that opens into the vagina, which leads to the outside of the body.
- Uterus: A hollow, pear-shaped organ that is located in a woman's lower abdomen, between the bladder and the rectum.
- Placenta: A temporary organ that joins the mother and fetus, transferring oxygen and nutrients from the mother to the fetus and permitting the release of carbon dioxide and waste products from the fetus.
- Sagittal plane: Plane parallel to the median plane; sagittal planes are vertical planes in the anatomic position.
- Coronal plane: A vertical plane at right angles to a sagittal plane, dividing the body into anterior and posterior portions, or any plane parallel to the central coronal plane.
- Axial plane: Transverse plane at right angles to the long axis of the body, as in CT scanning.
- Occipito-posterior position: A cephalic presentation of the fetus with its occiput turned toward the sacrum or rotated to the right (right occipito-posterior, ROP) or to the left (left occipitoposterior, LOP) sacroiliac joint of the mother.
- Occipito-anterior position: A cephalic presentation of the fetus with its occiput under the symphysis or rotated toward the right (right occipito-anterior, ROA) or to the left (left occipito-anterior, LOA) acetabulum of the mother.
- Shoulder dystocia: Arrest of normal labor after delivery of the head by impaction of the anterior shoulder against the symphysis pubis.

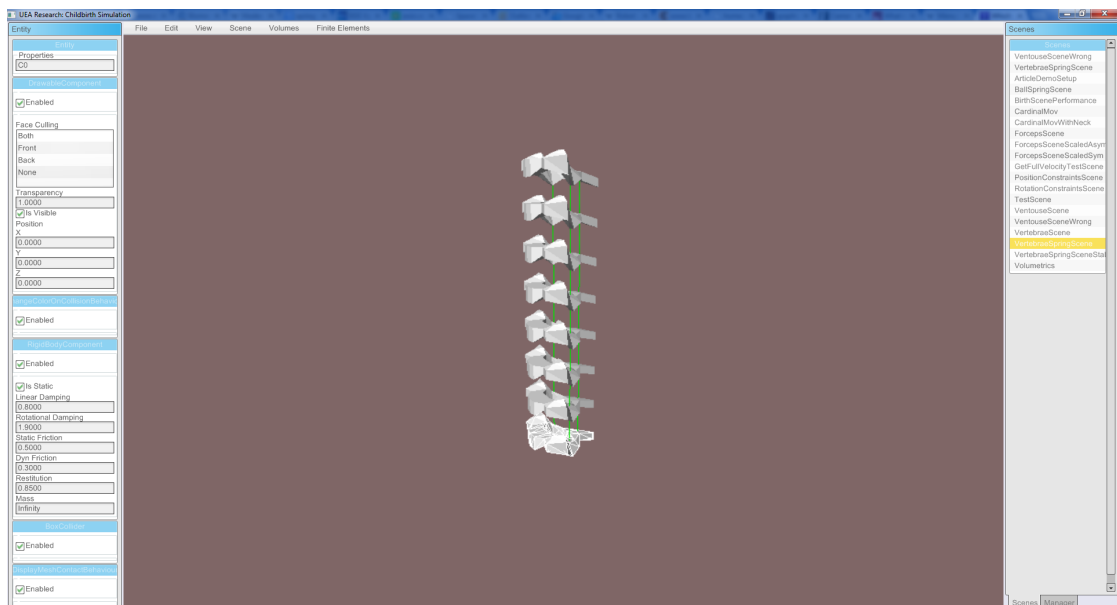
- Biparietal diameter: the diameter of the fetal head between the two parietal eminences.
- Flexion: in obstetrics, the normal bending forward of the head of the fetus in the uterus or birth canal so that the chin rests on the chest, thereby presenting the smallest diameter of the vertex.
- Extension: opposite to flexion.
- Lateral: pertaining to a side.
- Suprapubic: above the pubic bone.

Appendix E

Childbirth simulators

E.1 BirthEngine

The BirthEngine software is a generic medical simulation engine used to simulate forward-engineered childbirth process (see Figure E.1). The simulator is written in C# and it is completely cross-platform. In addition, it utilizes modern software engineering design patterns and practices (Lapeer et al., 2014).



1. The main window.

E.2 BirthView

BirthView is the current version of the childbirth simulation software written in low-level C++ language. It is cross-platform and scalable.

E.2.1 Cross-platform

BirthView is using the Simple DirectMediaLayer (SDL), which is a cross-platform development library designed to provide low level access to input devices (keyboard, mouse), audio and graphics hardware via OpenGL and Direct3D (Simple DirectMedia Layer, 2016).

E.2.2 Scalability

BirthView is plugin/static libraries based and can be easily extended by creating a separate project. Each project in the BirthView solution explorer (see Figure E.1) contain many projects, which represent a static library extending the generic core project.

E.2.3 Entity Component System

Entity component system (ECS) is an architectural pattern and is mostly used in game development. The pattern follows the *Composition over Inheritance* principle, where every object in a simulation's scene is an Entity, which typically stores only a container of components. The behaviour of an entity is specified by attaching different Components to the entity and can be done dynamically at runtime. As shown in Figure E.4 in BirthView the entities do not have identification numbers and the components are responsible for rendering (RenderableComponent), collision detection (CollidableComponent) etc. ECS is described in detail in the paper by Martin (2007).

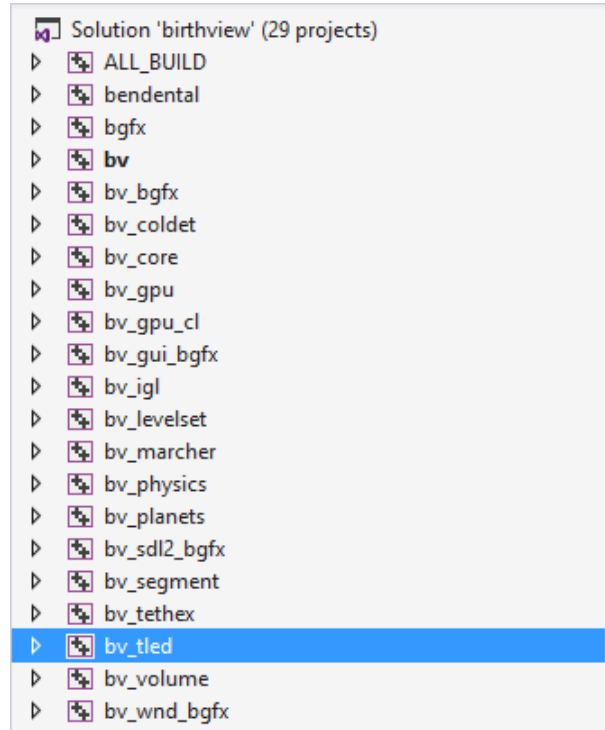


Figure E.1: BirthView solution's list of plugin projects.

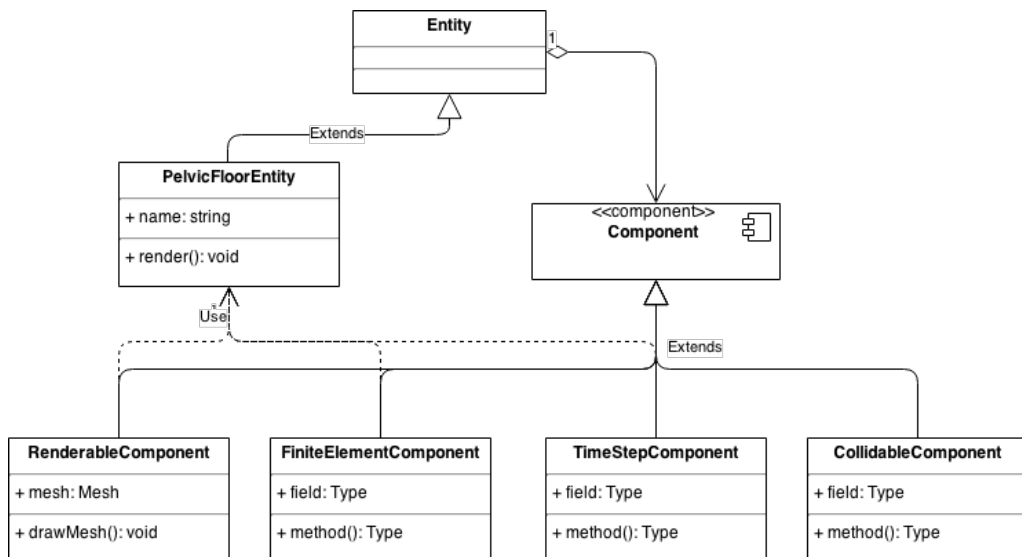


Figure E.2: Entity component system used in BirthEngine.

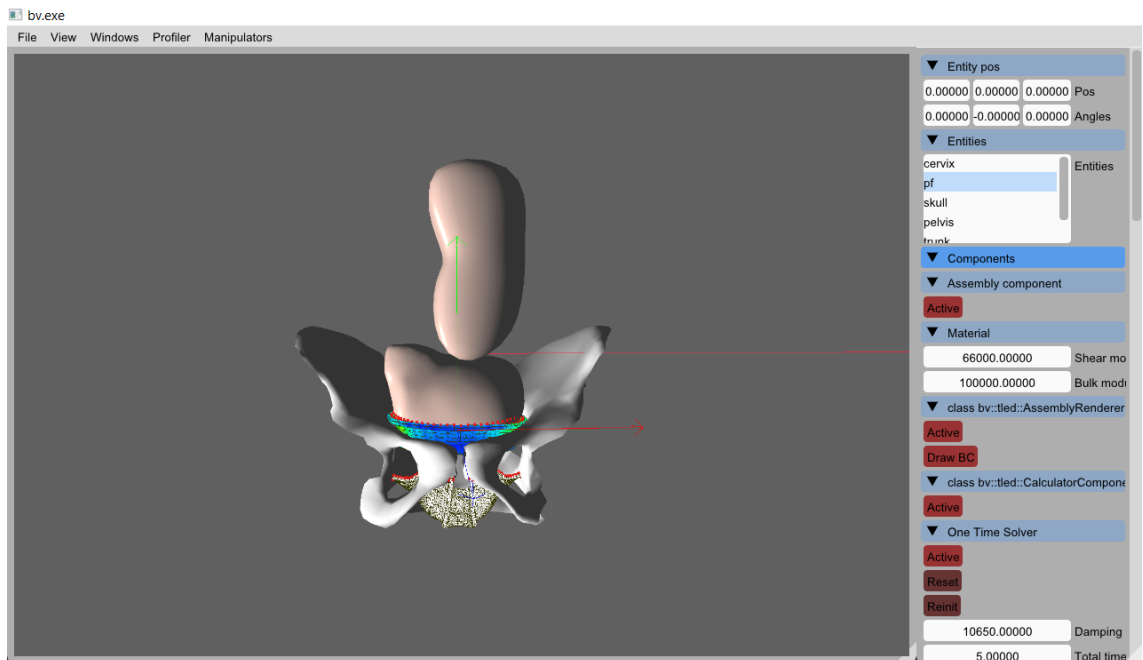


Figure E.3: Cervix Scene in BirthView.

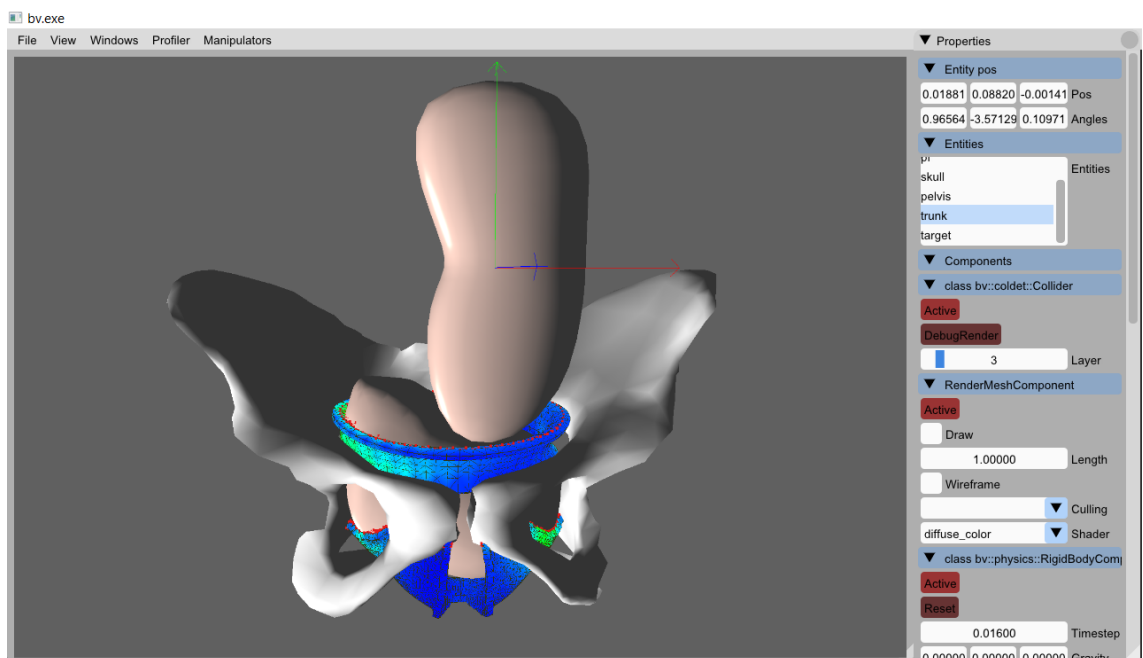


Figure E.4: Cervix Scene in BirthView.

Appendix F

Human Spine

The spine is a collection of vertebrae connected by vertebral joints, discs, ligaments, tendons and muscles.

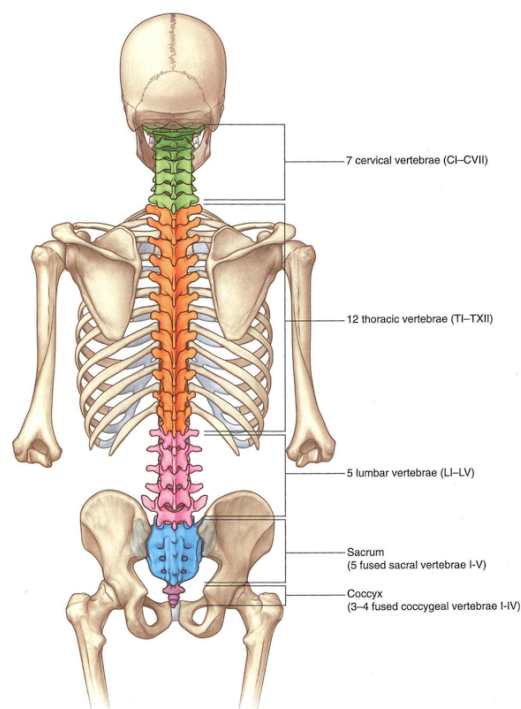


Figure F.1: Spine regions. Image from Drake et al. (2015).

F.1 Vertebral Column

There are approximately 33 vertebrae in the human spine (see Figure F.1), which can be further subdivided into five groups (Drake et al., 2015):

1. The seven cervical vertebrae, which are characterized by their small size;

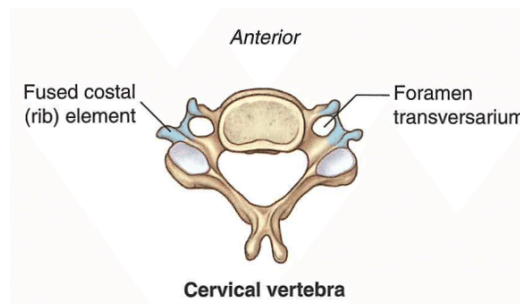


Figure F.2: Cervical Vertebra. Image from Drake et al. (2015).

2. The twelve thoracic vertebrae, which are characterized by their articulated ribs. All vertebrae embody rib elements into their transverse processes, whereas only the thoracic vertebrae articulate with the actual ribs in the thorax region;

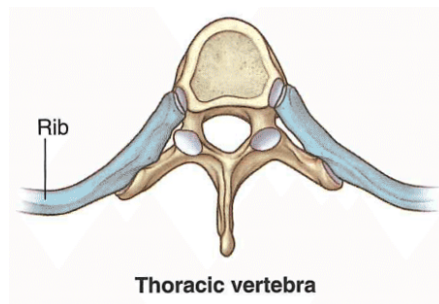


Figure F.3: Thoracic Vertebra. Image from Drake et al. (2015).

3. The five lumbar vertebrae, which are characterized by their large size, provide the skeletal support to the posterior wall of the abdominal cavity;
4. The five sacral vertebrae, which are fused into one single bone, called the *sacrum*, which is a component of the pelvis;

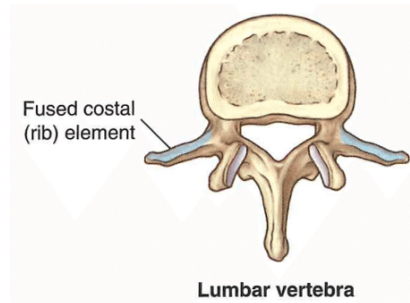


Figure F.4: Lumbar Vertebra. Image from Drake et al. (2015).

5. The coccygeal vertebrae, which vary in number between three and five, also fused into a single bone, called the *coccyx*.

F.2 Vertebra

A typical vertebra is formed by a vertebral body and a posterior vertebral arch. A vertebra also encloses various processes: a spinous process, a transverse process and an articular process/see Figure F.5.

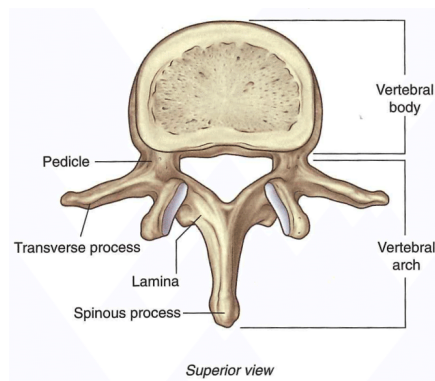


Figure F.5: Typical Vertebra. Image from Drake et al. (2015).

F.3 Joints

There are two major types of joints between vertebrae: intervertebral discs and synovial joints. A typical vertebra has six joints with the adjacent vertebrae: four

synovial joints and two intervertebral discs.

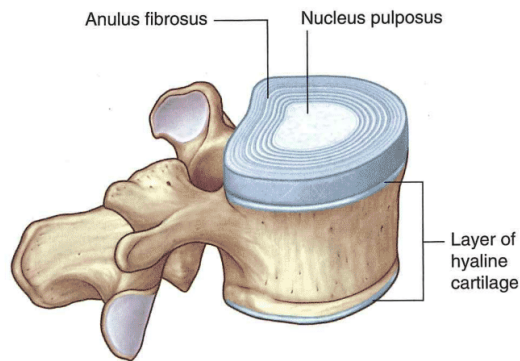


Figure F.6: Intervertebral Disc. Image from Drake et al. (2015).

F.3.1 Intervertebral Discs

Intervertebral discs are formed by an outer anulus fibrosus and inner nucleus pulposus. The arrangement of fiber of the anulus fibrosus limits rotation between vertebrae, whereas the nucleus pulposus, which is in the centre of the disc, absorbs compression forces/see Figure F.12.

F.3.2 Synovial Joints

The joints between the articular processes are called the zygapophysial joints (see Figures F.7 and F.8). Depending on the region of the human spine, these joints have different orientations and, therefore, together with the shape of the vertebral bodies, either facilitate or limit certain movements: flexion, extension, lateral flexion and rotation.

F.3.3 Ligaments

The joints are reinforced by various ligaments involved in holding together the vertebrae and the movements of the vertebral column:

- Anterior and posterior longitudinal ligaments (see Figure F.9)
- Ligamenta flava (see Figure F.10)

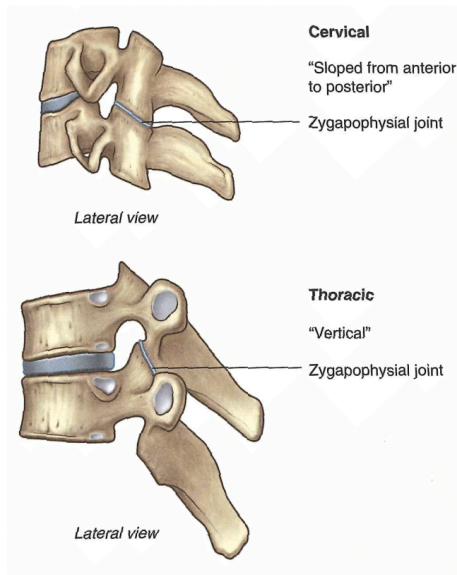


Figure F.7: Zygapophysial Joints (Cervical and Thoracic). Image from Drake et al. (2015).

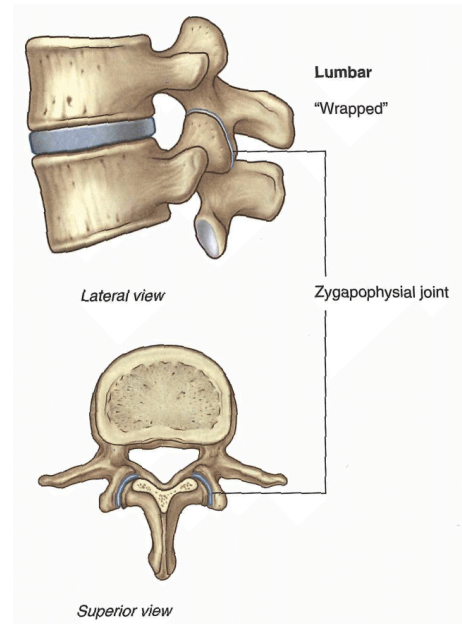


Figure F.8: Zygapophysial Joints (Lumbar). Image from Drake et al. (2015).



Figure F.9: Anterior and Posterior Longitudinal Ligaments. Image from Drake et al. (2015).

- Supraspinous ligament (see Figure F.11)

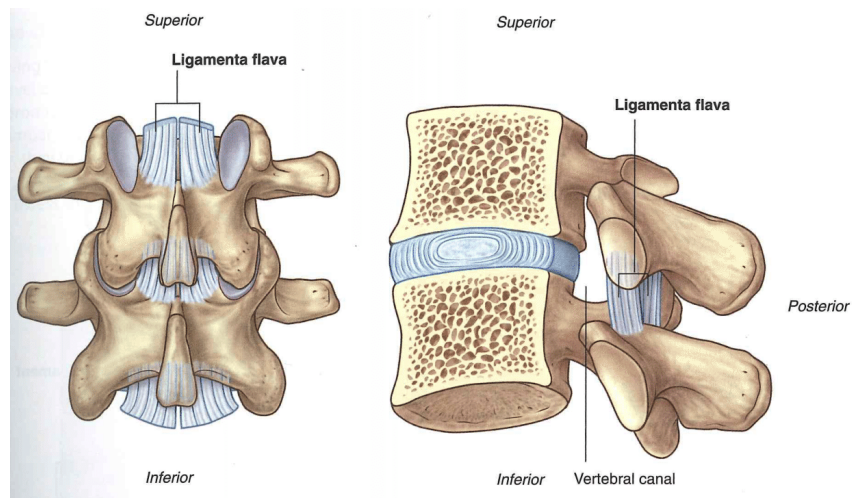


Figure F.10: Ligamenta Flava. Image from Drake et al. (2015).

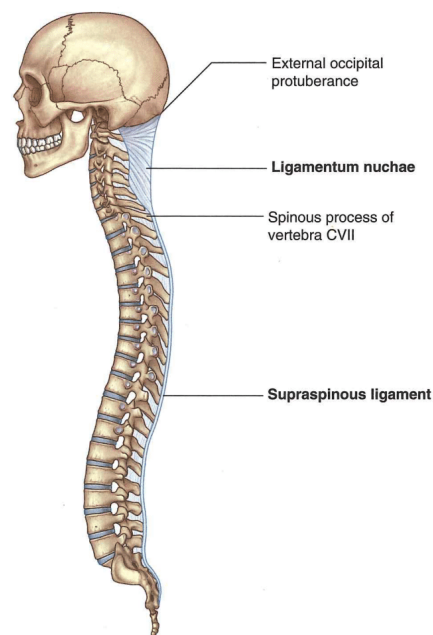


Figure F.11: Ligamentum Nuchae and Supraspinous Ligament. Image from Drake et al. (2015).

- Ligamentum nuchae (see Figure [F.11](#))
- Interspinous ligaments (see Figure [F.12](#))

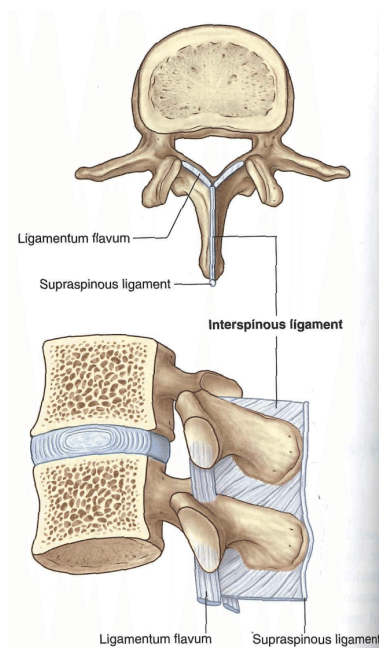


Figure F.12: Interspinous Ligaments. Image from Drake et al. (2015).